TEMPERATURE DEPENDENT RUBIDIUM-HELIUM LINE SHAPES

AND FINE STRUCTURE MIXING RATES

DISSERTATION

Wooddy S. Miller, Captain, USAF

AFIT-ENP-DS-15-S-027

DEPARTMENT OF THE AIR FORCE
AIR UNIVERSITY

AIR FORCE INSTITUTE OF TECHNOLOGY

Wright-Patterson Air Force Base, Ohio

TEMPERATURE DEPENDENT RUBIDIUM-HELIUM LINE SHAPES

AND FINE STRUCTURE MIXING RATES

DISSERTATION

Presented to the Faculty

Graduate School of Engineering and Management

Air Force Institute of Technology

Air University

Air Education and Training Command

in Partial Fulfillment of the Requirements for the

Degree of Doctorate of Philosophy in Engineering Physics

Wooddy S. Miller, M.S.

Captain, USAF

September 2015

AFIT-ENP-DS-15-S-027

TEMPERATURE DEPENDENT RUBIDIUM-HELIUM LINE SHAPES

AND FINE STRUCTURE MIXING RATES

Wooddy S. Miller, M.S.
Captain, USAF

Committee Membership:

Glen P. Perram, PhD
Chairman

David E. Weeks, PhD
Member

Benjamin F. Akers, PhD
Member

ADEDJI B. BADIRU, PhD
Dean, Graduate School of Engineering
and Management

Abstract

Line shapes for the Rb D_1 (5 $^2\mathrm{S}_{1/2} \rightleftarrows$ 5 $^2\mathrm{P}_{1/2}$) and D_2 (5 $^2\mathrm{S}_{1/2} \rightleftarrows$ 5 $^2\mathrm{P}_{3/2}$) transitions with ^{4}He and ^{3}He collisions at pressures of 500 - 15,000 Torr and temperatures of 333 - 533 K have been experimentally observed and compared to predictions from the Anderson-Talman theory. The observed collisionally induced shift rates for ^{4}He are dramatically higher for the D_1 line, 4.60 ± 0.12 MHz/Torr than the D_2 line, 0.20 ± 0.14 MHz/Torr. The asymmetry is somewhat larger for the D_1 line and has the same sign as the shifting rate. The ^{3}He broadening rate for the D_2 line is 4% larger than the ^{4}He rate, and 14% higher for the D_1 line, reflecting the higher relative speed. The calculated broadening rates are systematically larger than the observed rates by 1.1 - 3.2 MHz/Torr and agree within 14%. The primary focus of the first experiment is to characterize the high pressure line shapes, focusing on the non-Lorentzian features far from line center. In the far wing, the cross-section decreases by more than 4 orders of magnitude, with a broad secondary maximum in the D_2 line near 735 nm. The potentials do not require empirical modification to provide excellent quantitative agreement with the observations. The dipole moment variation and absorption Boltzmann factor is critical to obtaining strong agreement in the wings.

Temperature dependent shift and broadening rates have been experimentally measured over a temperature range of 373 K to 723 K and compared to prior predictions from the Anderson-Talman theory and quantum treatments involving Allard and Baranger coupling. The shift coefficients exhibit an increase of 20% from 4.36 MHz/Torr to 5.35 MHz/Torr for the D_1 line and an 80% increase from .42 MHz/Torr to .99 MHz/Torr for the D_2 line over the temperature range. Broadening coefficients exhibit a 6% increase from 17.8 MHz/Torr to 18.9 MHz/Torr and 10% from 18.5 MHz/Torr to 20.5 MHz/Torr for the D_1 and D_2 lines respectively. The experimental values agree well with prior reported values within the temperature overlap regions of T < 394 K. The closest theoretical prediction to the

observed values is the Anderson-Talman approach using spin orbit multi reference (SOCI) ab initio potentials.

A laser induced fluorescence (LIF) experiment using a hybrid continuous wave (CW) - pulsed laser excitation pumping scheme was used to measure the temperature dependent spin-orbit (SO) mixing rates. An experimental apparatus was designed and built allowing for temperatures up to 723 K to be explored which is 350 K higher than any other experiment other than Gallagher in 1968. A proposal for a systematic exploration of the σ_{SO} rates was developed with initial observed values of 2.17×10^{-16} cm^2. The temperature dependence of the rates were explored resulting in a increase of 6 times the initial value compared with an increase of 3 time the initial value observed by Gallagher. These initial observations require further exploration.

Acknowledgments

I would like to thank the many many people who were instrumental in helping me throughout this degree program. First in a long list of support goes to my Loving Wife for all of her support. Her love and support has helped through both the rough times where things didn't work and the good times where I was actually getting data.

I would like to thank my committee whose guidance and direction allowed me to stay on task while providing usefull and needed information to the scientific community. Dr. Glen Perram has been an awesome advisor who has kept me on task while providing more insight from a single person than I thought possible. Dr. David Weeks and Dr. Ben Akers have also provided support, asked me questions to make me think deeper about the problem, and made themselves available for any questions I may have had in return. I would also like to thank Dr. Gross who took time out of his busy schedule to help me with various programing problems.

The lab technicians Mike Ranft and Greg Smith who were always willing to help set up equipment in the lab. My fellow students who were always willing to lend a hand especially Ben Eshel and Rick Davila.

Finally, the man who has been tireless in his persuit of helping those students that need him. Dr. Christopher Rice has selflessly given of his time and energy to help through every step of the way. From guiding and coaching on various laboratory setup techniques to pointing out flaws in my analysis techniques. Without Dr. Rice this degree would not have gone as smoothly nor been as productive as is has been. For everything that has been done for me and to all those who have helped and supported me, Thank You.

Wooddy S. Miller

Table of Contents

List of Figures

List of Tables

List of Symbols

Symbol		Page

TEMPERATURE DEPENDENT RUBIDIUM-HELIUM LINE SHAPES
AND FINE STRUCTURE MIXING RATES

I. Introduction

Diode Pumped Alkali Lasers (DPALs) are a new type of laser that uses alkali metal vapor as a gain medium and a buffer gas to control the line shape and kinetics. While these systems were first demonstrated in 2003 [48] they have just recently been scaled to the kilowatt power levels in 2012 [18]. To achieve these powers, the design of the gain cell relied on a set of incomplete line shape and kinetic data. The current focus areas of DPAL research are the continued power scaling of the systems and basic science research into the rates involved within the system.

The purpose of this research is to determine the physical parameters of various alkali-noble gas interactions with a high degree of accuracy. The physical parameters of interest here include pressure broadening (γ), pressure shift (δ), asymmetry (β_0), the quenching rates (k_{20}, k_{10}), and spin-orbit (SO) mixing rates (k_{12}, k_{21}). Various measurements of these line shape parameters and the rates associated with these systems have been taken over the years at low temperatures and usually low pressures. Temperatures of the measurements range from 320 K [39] to 394 K [68] with pressures of 300 Torr [68]. Various theories including the semi-classical approach of Anderson Talman [4, 43] and the full quantum mechanical treatment of Baranger [7] can be used to predict line shape parameters provided that the interaction potentials, are well known. Ab initio calculations generated potential energy curves [16] that have been used by theory to predict these rates and line shape parameters. While these predictions work at lower pressures they start to differ from experimental results in the line shape wings at higher pressure [61]. Theory can also be used

1

to predict the temperature dependence of the spin-orbit mixing rates (k_{12}, k_{21}), broadening, and shift [15]. The temperature dependence of the shift and broadening rates is a very sensitive probing tool and is highly dependent on having the correct potential energy curve. Using the current theoretical work and potentials there is good agreement with the observed broadening rates, but the values and even the sign of the pressure shift vary greatly [15].

This research will focus on observing asymmetric line shapes at pressures from 500 to 15,000 Torr and examining the temperature dependence of the rates and line shape parameters up to T = 725 K. This temperature dependence has been shown with a few data points in various experiments [29, 67] and is predicted by theory. The high pressures will be used to explore the features in the wings of the line shapes and determine the asymmetry of the line shape. The line shape and kinetic databases will be expanded using this experimental data. Using these expanded databases the current potential energy curves will be adjusted until they match with the experimental broadening, shift, and asymmetry data. The new energy curves will then be used to try to predict the correct temperature dependence of the various line shape parameters and rates.

In order to obtain these new rates the following tasks were undertaken. The first task measured the temperature dependence (T = 300-725 K) of the broadening and shift rates for the D_1 and D_2 of the Rb-^{4}He interaction. These parameters were compared with the predictions from Anderson-Talman theory, Baranger theory, and compared to other experimental data. The second task was to measure the spin-orbit mixing rates of the Rb $5^2P_{3/2} \rightleftarrows {}^2P_{1/2}$ transition for both the ^{4}He and ^{3}He cases as a function temperature (T=300-725 K). These mixing rates were observed using a new method that combines the pulsed and continuous wave (CW) type experiments into a single quasi-CW pump method. The CW pumping method has a better signal-to-noise ratio (SNR), but does not have the directly measured time basis. The pulsed experiment directly measures the times basis though typically has a lower signal-to-noise ratio. The quasi-CW pumping method will

have the increased signal to noise associated with the CW while still allowing for a limited measurement of the direct time basis. These resultant rates, will be compared to various theoretical models and prior results.

The experimental results along with the various theoretical calculations from these experiments will have a two fold effect. The first is the increased population of a sparse kinetics database for future use in predicting line shape parameters, calculating potential energy surfaces, and modeling collisional interactions. The second effect these measurements will have is the advancement of the DPAL program in general through a greater understanding of how temperature changes affect the system, and will allow for models that predict and model temperature changes within the system, not just the global parameters. This will allow for better power scaling and beam quality, two areas where the DPAL has a great advantage over other laser systems such as solid state lasers.

II. Background and Literature Review

2.1 Diode Pumped Alkali Laser (DPAL)

The Diode Pumped Alkali Laser (DPAL) is a three level laser system that uses alkali metal vapor as a gain medium as shown in Figure 2.1. The DPAL works by first exciting the alkali atom from the ground $^2S_{1/2}$ state up to the first $^2P_{3/2}$ state along the D_2 transition. The excited alkali must relax down to the excited $^2P_{1/2}$ state before it can then emit down to the ground state along the D_1 transition. In order to move populations from the excited $^2P_{3/2}$ state down to the lower excited $^2P_{1/2}$ a collisional partner is necessary because there is not an allowable optical transitions between the two excited states. This collisional partner is a gas mixture that is pumped into the cell. The gases used range from hydrocarbons mixtures such as ethane [56] to ethane with helium [84, 86] to pure hydrocarbon free mixtures such as ^{4}He [79] and ^{3}He [80]. The first demonstration of the DPAL system in 2003 used a mixture of Rb, and ethane and He for its buffer gas [48].
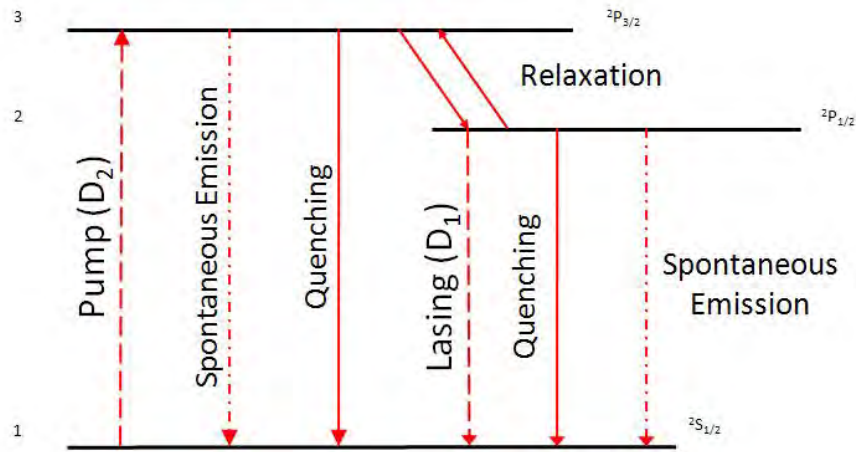
Figure 2.1: 3 Level DPAL System showing all of the optical transition paths [56]

4

The ability of the DPAL system to scale to higher power is what makes it a highly studied system. A sample scaling of output intensity with pump intensity is shown in Figure 2.2. The three regions of interest on this curve are the linear slope portion, the rollover, and the bleached cell limit. The initial linear slope defines the efficiency of the laser and ideally would be as close to the quantum limit (98.1% for Rb). The slope efficiency of the laser system can be described as the change in output laser power (P_L) as a function of input pump power (P_p) [85]:

$$\frac{dP_L}{dP_p} = \frac{T}{L+T}\frac{\nu_L}{\nu_P}\eta_P\frac{dS}{dF} \tag{2.1}$$

In the slope efficiency equation the first factor is the output coupler (T) and internal losses (L) of the system. The second factor is the quantum efficiency (η_L) of the system which is the laser frequency (ν_L) over the pump frequency (ν_P). The third factor is the fraction of the pump that is absorbed by the medium, the pump efficiency (η_P), and is related to the modal overlap of the system. The final factor, $\frac{dS}{dF}$, is how efficiently each pump photon is turned into a laser photon which includes quenching and re-absorption of emitted photons. Slope efficiencies as high as 81% have been achieved [85].

At the high pump intensity end of the curve is the asymptotic limit of the system or the bleached cell limit. The incoming pump source has excited all of the available alkali atoms in the system and there is a bottle neck that has occurred between the $^2P_{3/2}$ and $^2P_{1/2}$ states. The number of alkali excited in the $^2P_{3/2}$ state are rate limited in their relaxation down to the $^2P_{1/2}$ state. With no more available alkali to excite and the limitation on the movement between the two excited states the power of the system can not go up resulting in a waste of input power at this limit. This bleaching limit is dependent upon the alkali density within the cell and the amount of buffer gas in the system. Due to these constraints this upper limit is most easily raised through either the increase in alkali density which will also modify the threshold or by increasing the amount of buffer gas in the system to allow for faster transition between the excited P levels [33, 35].
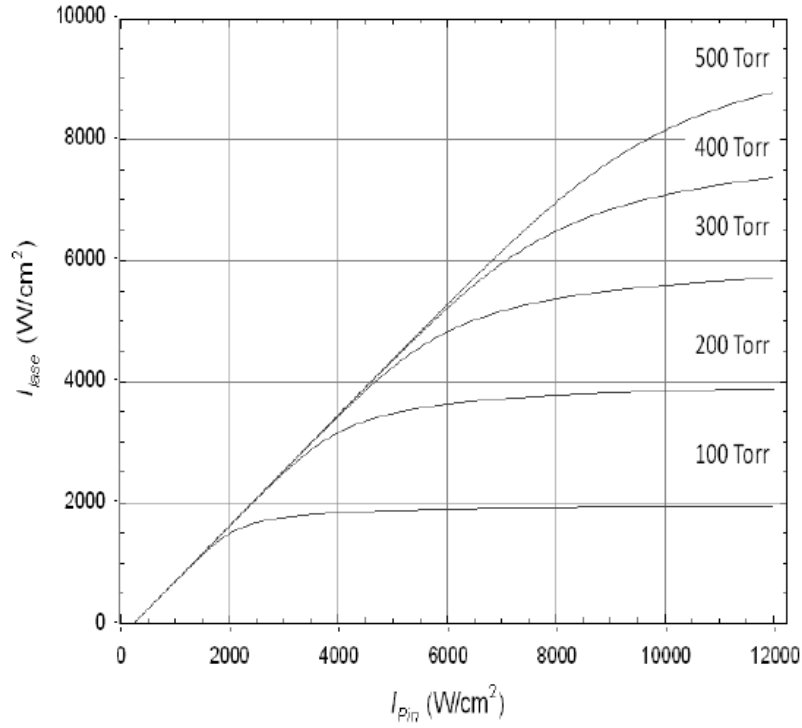
Figure 2.2: Computed Intensity in vs Intensity out curve for various pressure of buffer gas showing the linear increase at the start followed by the rolling over section and the bleached cell limit for various buffer gas pressures. [33, 35]

In the transition region between these two limits, the curvature depends critically on the spectral line shape absorption relative to the diode bar bandwidth. A simple view of this curvature vs the ideal case can be seen in Figure 2.3. This curved region describes how well matched the line shapes of the system and the pump sources are. In an ideal case the power would scale linearly until it hits the bleached limit. This does not happen because of mismatch between these two line shapes [35]. When the pump line shape is either too narrow or too broad compared to the alkali D_2 and D_1 transitions pump power is wasted either in pumping the core where it bleaches the core of the line shape while missing the wings. The opposite case of being too broad means a lot of the energy is wasted pumping

6
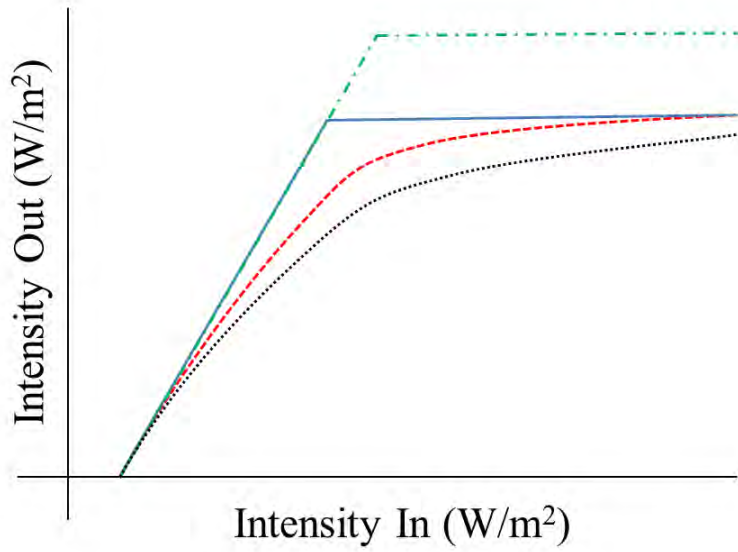
Figure 2.3: Ideal depiction of I_{out} vs I_{in} curve with three regions: an ideal linear increase in I_{out} up to the bleached limit (—), an ideal linear increase in I_{out} to a higher bleached limit with the addition of more buffer gas (- · -), a realistic curve with mismatched pump line shape (- - -), a realistic curve with a more severe pump mismatch (· · ·)

wavelengths that are outside of the transition. Both cases of pump transition mismatch lead to loss within the system reducing the systems overall efficiency.

The natural line width of the alkali transitions is very small, approximately 36 MHz and 38 MHz for the D_1 and D_2 transitions [73, 74] which is much narrower than most pump sources. Doppler broadening of the system, approximately 500 MHz at room temperature, is much larger than the natural line width and closer to current pump sources. Adjustment of the pump source line width is possible, and is currently being worked on by various groups. A 30 W diode source that has been narrow banded down to only 10 GHz has been demonstrated by Gourevitch et al. [30], but considering the natural line width of the alkali transitions this is still not narrow enough without more modification. To correct this the

7

transitions of the alkali must be adjusted to allow for matching with these pump sources. The buffer gases introduced into the system to allow for the spin-orbit mixing also allow for the adjustment of the line shapes to better match the pump sources available. In order for a system to be able to fully use the 10 GHz pump source approximately 500 Torr of helium would be needed to broaden the transition with 5,000 Torr (over 6 atmospheres) for a less narrowed 100 GHz pump source.

The gases added into the system not only broaden the transition and allow for spin-orbit relaxation, the gas also effects the absorption cross-section and related the saturation intensity (I_{sat}) of the system. The saturation intensity is the pumping intensity at which the small signal gain of the laser is reduced by half. I_{sat} is calculated as:

$$I_{sat} = \frac{h\nu_{20}}{\sigma}\Gamma_{20} \tag{2.2}$$

with the cross-section being related to the broadened line shape, $g(\lambda)$ via:

$$\sigma_{20} = \frac{g_u}{g_l}\frac{\lambda^2}{8\pi}A_{ul}g(\lambda) \tag{2.3}$$

where

h = Plank's constant

ν_{20} = D_2 transition frequency

Γ_{20} = $^2P_{3/2}$ natural line width

g_u = $^2P_{3/2}$ degeneracy

g_l = $^2P_{1/2}$ degeneracy

λ = transition wavelength

A_{ul} = $^2P_{3/2}$ lifetime

Early DPAL systems typically used a hydrocarbon gas such as ethane as a spin-orbit relaxation gas [81, 84, 86]. The reason for this early use of hydrocarbons is their ability to create very high mixing rates. The mixing rate is the defined as the collisional cross-section, σ, times the thermally averaged velocity $\bar{v}$. This high mixing rate effectively moves

the population from the upper excited state to the lower leading to the population inversion needed to operate the laser. These heavy hydrocarbons also tended to quench the system though, which is where a collision between the alkali and the buffer gas leads to a non-radiative transition down to the ground level. When this happens the energy used to excited the alkali is wasted by being turned into heat leading to a less efficient laser due to the wasted energy. The hydrocarbon mixtures also demonstrated a tendency to deposit carbon soot on the windows of the cell. The carbon soot comes from hydrocarbons reacting with alkali metals at high temperatures and pumping intensities creating an alkali hydride [79]. Due to these problems associated with the hydrocarbons Lawrence Livermore National Laboratory (LLNL) in 2007 created the first hydrocarbon-free rubidium laser [79]. Since then many of the recent works have focused on using hydrocarbon free systems that use helium or the other noble gases for spin-orbit relaxation. Details are discussed in the line shape section 2.2 and the kinetics sections 2.3.

A few of the useful qualities of the alkali metals that make them ideal for a robust field system include ease of handling, low quantities of alkali metals needed for operation, and a small quantum defect. Both the ease of handling and the needed quantity of alkali are logistical issues, but are still important considerations for fielded systems. The small quantum defect is a physical property of the alkalies that is exploited for the laser creation.

Alkali metal, once it has been inserted into the laser system, is closed off from the user. The metal does not get used up in the process of running an alkali laser meaning more does not need to be put in or taken out regularly. The DPAL also does not take large quantities of alkali to run due to the nature of the metal vapor gain medium which typically operates with a number density on the order of 10^{13} cm^{-3}. In a laboratory laser demonstration milligrams of alkali metal can be sufficient to run the system for months. These two items combine to cut down on logistical problems.

9

The small quantum defect, or the energy spacing between the pump level and the lasing level is very small for the alkali metals. A small energy gap between the two levels means that there is less energy wasted as heat when the excited alkali collides and loses energy to go the top of the lasing level. All of alkalies show this small gap, with the heavier alkalies having slightly larger differences. The various energy levels for rubidium and cesium can be seen in Figure 2.4. These small energy gaps mean that the quantum efficiency of the system can reach up to 99% for K, 98% for Rb, and 95% for Cs.

2.2 Lineshapes

Much work has been done through the years on the line-shapes of excited transitions of the alkali metals including those done by Romalis [67] and Rotondaro [68]. The three areas of interest in these line shapes typically include the pressure broadening, γ, pressure shift δ, and the asymmetry, β_0 of the line. The pressure broadening of the line, γ, is typically described as the full-width half-maximum (FWHM) and changes as a function of temperature. The pressure shift, δ, describes the changing of the center frequency of the peak of the line shape. When there is no pressure, the peak of the line shape is at the fundamental frequency of the transition. The asymmetry, β_0, of the line shape describes how quickly one side falls off compared to the other. These three parameters are based off of fitting the core of line shape with a asymmetrically slanted Lorentz line shape given by:

$$I(v) = I_L(v) + I_A(v) \tag{2.4}$$

$$I_L(v) = 2\left(\frac{c}{w}\right)e^{-n\alpha_o}cos(n\beta_0)\frac{n\alpha_1}{(n\alpha_1)^2 + (\frac{2\pi c}{w}v - n\beta_1)^2} \tag{2.5}$$

$$I_A(v) = 2\left(\frac{c}{w}\right)e^{-n\alpha_o}sin(n\beta_0)\frac{n\alpha_1(\frac{2\pi c}{w}v - n\beta_1)}{(n\alpha_1)^2 + (\frac{2\pi c}{w}v - n\beta_1)^2} \tag{2.6}$$

In the above equations (c) is the speed of light, (n) is the number density, and (w) is the angular frequency of the transition. The variables α_1, β_0, and β_1 correspond to broadening,
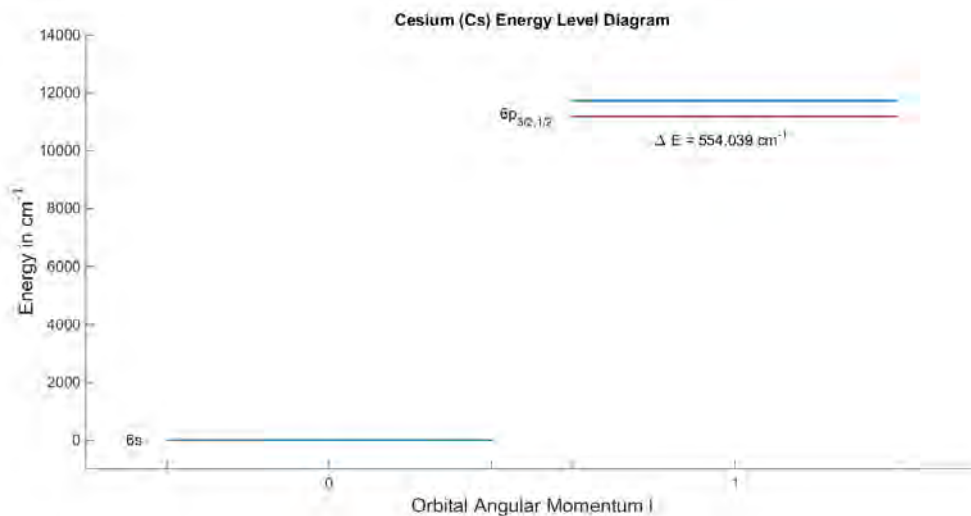
(a) Cesium Energy Levels
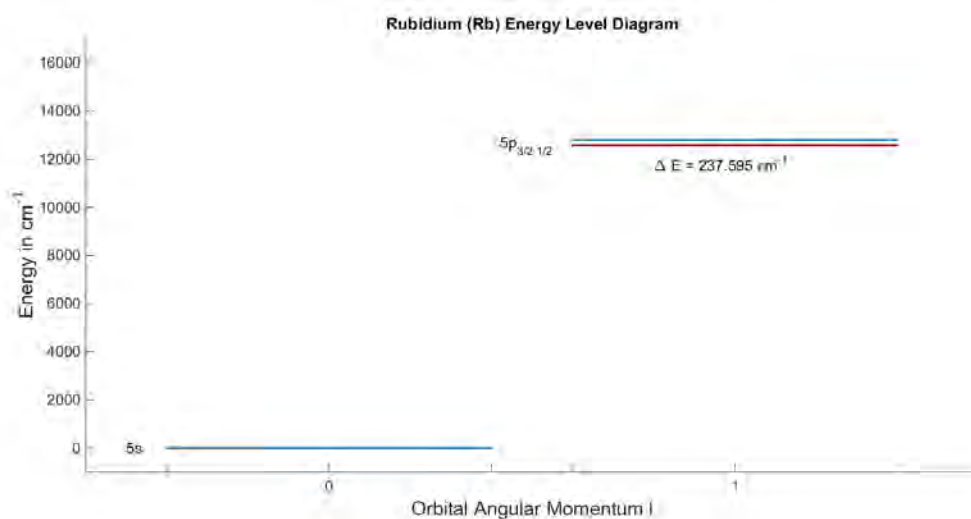
(b) Rubidium Energy Levels

Figure 2.4: Energy level diagrams for cesium and rubidium

shift, and asymmetry respectively with further derivations shown in Section 2.4.2. A representation of all of these can be seen in figure 2.6 with the fundamental values of rubidium being shown in Tables tables 2.1 to 2.6. Also of interest here is not just how pressure affects the line shape parameters, but also how these values vary with temperature.

11

There are various methods of determining these line shape parameters which will be described in more detail.

The number density of alkali in the system is based on the vapor pressure at the surface of the alkali pool. The relationship between temperature and pressure is given by the equations below for ^{87}Rb for temperatures below melting (solid phase) and temperature above melting point (liquid phase) respectively [73, 74]:

$$\log_{10}(P_v) = -94.04826 - \frac{1961.258}{T} - 0.03771687 \cdot T + 42.57526 \cdot \log_{10}(T) \qquad (2.7)$$

$$\log_{10}(P_v) = 15.88253 - \frac{4529.635}{T} - 0.00058663 \cdot T - 2.99138 \cdot \log_{10}(T) \qquad (2.8)$$

The vapor pressure is given in Torr with the temperature (T) given in K. Using the ideal gas law the vapor pressure is converted into a number density. A combined ^{85}Rb/^{87}Rb number density curve based on natural occurring relative abundances is shown in Figure 2.5. As seen with the log y-axis the number density increases rapidly for increasing temperature and in fact doubles every approximately 7.8 K. At the melting temperature of 312.5 K there is already a number density of 5×10^{10} cm^{-3}.
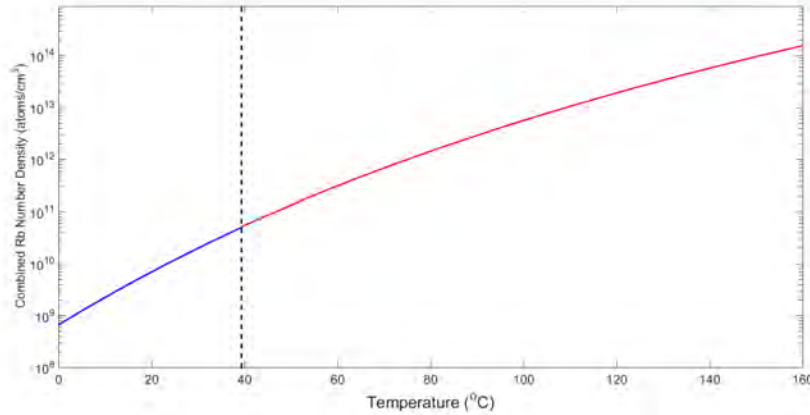
Figure 2.5: Combined Rb number density curves as a function of temperature [74]. The blue line represents the Rb density before melting point, shown as (- - -), with the red line representing the Rb density after the melting point.

Table 2.1: ^{85}Rb Physical Properties [73]

Atomic Number	Z	37	
Relative Natural Abundance	$\eta(^{85}Rb)$	72.17(2)%	[52]
Nuclear Lifetime	τ_n	(stable)	[52]
Atomic Mass	m	84.911 789 732(14) amu	[20]
Density at 25^0C	ρ_m	1.53 g/cm^3	[52]
Melting Point	T_M	39.30 °C	[52]
Boiling Point	T_B	688 °C	[52]
Nuclear Spin	I	5/2	

Table 2.2: ^{87}Rb Physical Properties [74]

Atomic Number	Z	37	
Relative Natural Abundance	$\eta(^{87}Rb)$	27.83(2)%	[52]
Nuclear Lifetime	τ_n	4.88 x 10^{10} yr	[52]
Atomic Mass	m	86.909 180 520(15) amu	[20]
Density at 25^0C	ρ_m	1.53 g/cm^3	[52]
Melting Point	T_M	39.30 °C	[52]
Boiling Point	T_B	688 °C	[52]
Nuclear Spin	I	3/2	

Table 2.3: ^{85}Rb D_2 Transition Optical Properties [73]

Frequency	w_0	$2\pi\cdot$384.230 406 373(14) THz	[8, 82]
Transition Energy	$\hbar w_0$	1.589 049 139(38) eV	
Wavelength (Vacuum)	λ_{vac}	780.241 368 271(27) nm	
Wavelength (Air)	λ_{air}	780.033 489(23) nm	
Wave Number (Vacuum)	$k_L/2\pi$	12 816.546 784 96(45) cm^{-1}	
Lifetime	τ	26.2348(77) ns	[17, 32, 72, 77]
Natural Line Width (FWHM)	Γ	$2\pi\cdot$6.0666(18) MHz	

Table 2.4: ^{85}Rb D_1 Transition Optical Properties [73]

Frequency	w_0	$2\pi\cdot$377.107 385 690(46) THz	[6, 8]
Transition Energy	$\hbar w_0$	1.559 590 695(38) eV	
Wavelength (Vacuum)	λ_{vac}	794.979 014 933(96) nm	
Wavelength (Air)	λ_{air}	794.767 282(24) nm	
Wave Number (Vacuum)	$k_L/2\pi$	12 578.948 390 0(15) cm^{-1}	
Lifetime	τ	27.679(27) ns	[32, 72, 77]
Natural Line Width (FWHM)	Γ	$2\pi\cdot$5.7500(56) MHz	

Table 2.5: ^{87}Rb D_2 Transition Optical Properties [74]

Frequency	w_0	$2\pi \cdot 384.230\,484\,468\,5(62)$ THz	[82]
Transition Energy	$\hbar w_0$	$1.589\,049\,462(38)$ eV	
Wavelength (Vacuum)	λ_{vac}	$780.241\,209\,686(13)$ nm	
Wavelength (Air)	λ_{air}	$780.033\,330(23)$ nm	
Wave Number (Vacuum)	$k_L/2\pi$	$12\,816.549\,389\,93(21)$ cm^{-1}	
Lifetime	τ	$26.2348(77)$ ns	[17, 32, 72, 77]
Natural Line Width (FWHM)	Γ	$2\pi \cdot 6.0666(18)$ MHz	

Table 2.6: ^{87}Rb D_1 Transition Optical Properties [74]

Frequency	w_0	$2\pi \cdot 377.107\,463\,380(11)$ THz	[8]
Transition Energy	$\hbar w_0$	$1.559\,591\,016(38)$ eV	
Wavelength (Vacuum)	λ_{vac}	$794.978\,851\,156(23)$ nm	
Wavelength (Air)	λ_{air}	$794.767\,119(24)$ nm	
Wave Number (Vacuum)	$k_L/2\pi$	$12\,578.950\,981\,47(37)$ cm^{-1}	
Lifetime	τ	$27.679(27)$ ns	[32, 72, 77]
Natural Line Width (FWHM)	Γ	$2\pi \cdot 5.7500(56)$ MHz	
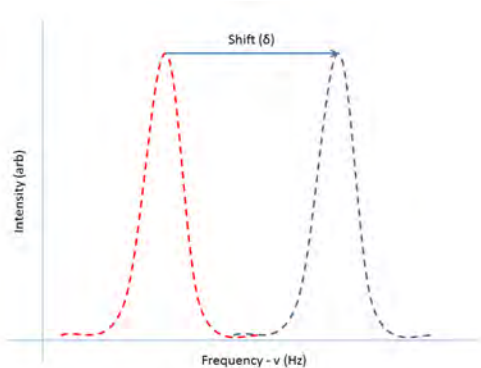
(a) Shift δ
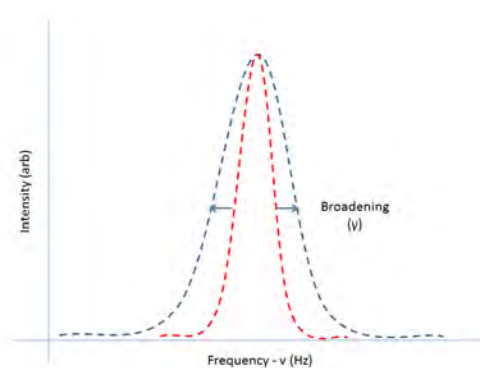
(b) Broadening γ
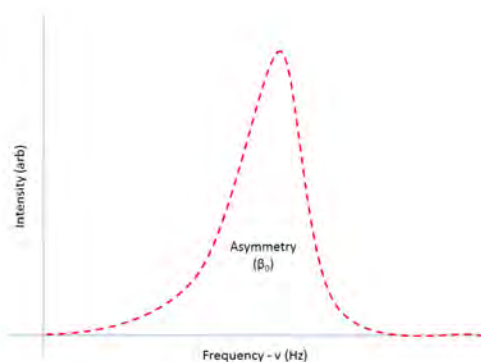
(c) Asymmetry β_0

Figure 2.6: Lineshape Demonstrations: a) shows the exaggerated shifting of the center wavelength of the line shape profile from a lower to a higher frequency b) shows the increase of the full-width at half maximum (FWHM) of the line shape c) demonstrates the asymmetrical nature of the line shape with the higher frequency side dropping off more rapidly than the lower frequency side

2.2.1 Laser Absorption.

The laser absorption technique used in the research is similar to the employed by Rotondaro [68] and Romalis [67]. The experimental setup used is shown in figure 2.7. Rotondaro used a tunable titanium-sapphire (Ti:sapphs) ring laser split into 3 using a trifurcated fiber bundle. Using one of those bundles to monitor the incident power of the laser the other two were used to probe the alkali vapor and reference cell. The reference cell was filled with alkali at a very low pressure ($\sim 10^{-6}$ torr) set at 360 K with the last fiber being directed through the test cell. The purpose of the reference cell is to provide a calibration for the wavelength axis. The alkali metals, having been studies extensively for decades, have very well known transitions. The absorbance profile of the alkali metal is then determined by the ratio of the transmitted intensity signal to the incident signal using the Beer-Lambert-Bouguer law, also known as Beer's law,

$$I(v) = I_0(v)e^{-\sigma nL} \tag{2.9}$$

where $I(v)$ is the transmitted signal, $I_0(v)$ is the incident signal, n is the number density
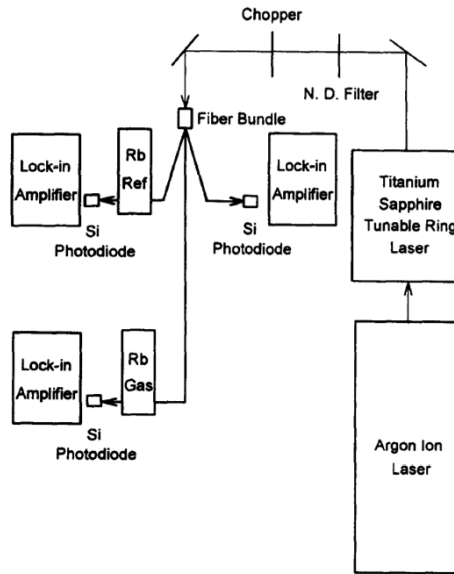
Figure 2.7: Rotondaro laser absorption experimental setup [68]

17

of absorbers, L is the absorption path length, and σ is the optical absorption cross section of those absorbers. By scanning the tunable laser's frequency an absorbance profile can be built up across the D_1 and D_2 transitions. This method was then repeated with different partial pressures of buffer gas in the cell ranging from 0 to 300 Torr while being kept at 394 K. Using data from multiple runs using varying pressures of buffer gas the line shape parameters can be determined as functions of pressure. Their results, along with others, can be seen in Table 3.1.

2.2.2   *Scanning Monochromator.*

The second method for determining line shapes is using a scanning monochrometer and a broadband light source. In this method a bright broadband light source is sent through a cell with the alkali metal and buffer gas. The alkali will absorb the light near the D_1 and D_2 transitions while allowing the light not near those transitions to pass through. A lens placed after the exit of the cell is then used to f-match the light to the monochromator. The f matching lens focuses the light on the entrance slit and is placed at such a distance that the light entering the monochromator fills the entire grating of the monochromator. The grating within the monochromator will then defract the light through the exit slit where a PMT will amplify the signal to be collected by a picoameter.

Using Beer's Law, Equation 2.9, the baseline intensity is divided out. In this case since there is no reference channel to determine the baseline a predetermined baseline is used. To create this baseline, scans of the system are taken when the cell is cold, but the source intensity is held at its data collection levels, leading to almost no alkali absorption due to the low alkali number density in the system. These scans then show the spectral response of the entire system without the alkali present. Multiple scans can be taken and then averaged to account for variations in light output and noise which are then averaged together and fit with a polynomial. Before the signals are ratioed the baseline is scaled to

fit the wings of the absorption profile. From there the log of the ratio of the two signals is taken resulting in the absorbance. An example experimental setup shown in figure 2.8.
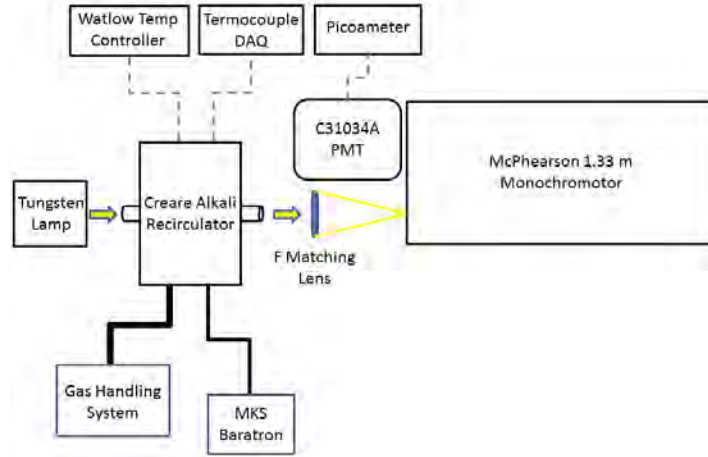
Figure 2.8: Experimental setup for the scanning monochromator method. There is a white light source that travels through the alkali cell and is f-matched before going into the monochromator. Various addition items record the pressure, temperature, and output signal with a Krypton pen lamp providing absolute wavelength correction.

2.2.3 Polarization Scattering.

The final method is a polarized scattering method [10, 11, 50]. This method typically uses an intense pump beam of polarized light to selectively pump part of the transition. By pumping the isotropic material with the polarized light the transition follows the ΔM selection rule for polarized light of ± 1 depending on either right or left-handed circularization. When this happens the degenerate sublevels become depleted leaving a non-isotropic material. In this now anisotropic material the incoming probe beam sees a birefringent material that can be measured using a set of crosses linear polarizers.

In this type of experiment a broadband light source is sent through a notch filter to pick the D_1 line and then through a circular polarizer. The light is then sent through the

alkali cell filled with buffer gas. Inside the cell the alkali vapor becomes weakly polarized through the absorption of the circularly polarized light. The intensity of the light that passes through at this point is the baseline. As an radio frequency (rf) field is applied to the cell and scanned the alkali-metal will become depolarized leading to a decrease in intensity of the light that passes through. This creates the absorption profile of the transition [10].

2.2.4   *Line Shape Temperature Dependence.*

Temperature dependent line shape data in the literature is very limited in scope. Most experiments that look at pressure broadening and shifting only use one temperature. As shown later in Table 3.1 experimental temperatures range from 310-394 K with a complete listing of various measured values. Among the various measurements there is good agreement on the pressure broadening rate of around 18 MHz/Torr for the D_1 line and a slightly higher 20 MHz/Torr for the D_2 line. The reported shift values though do not share such agreement. Measured values of the shift for the D_1 line is in general agree in the 4.5-5.0 MHz/Torr range. The D_2 shift though varies greatly with measured values from -.47 MHz/Torr [60] to 2.2 MHz/Torr [12]. This range in values even has a sign change denoting the direction of the center wavelength is going in opposite directions.

The two best pieces of temperature dependence for the line shape data come from experimental data from Romalis [67], theoretical computations done for his dissertation by R. Loper [53], and the Anderson-Talman approach used by Hager [34] and Blank [14, 15]. The Romalis data shows a linear increase in both the FWHM of the measured line shapes with temperature, as well as an increase in the shift of the central wavelength. The data was taken at three temperatures for ^{4}He, 333, 353, and 373 K with ^{3}He being taken at 353 K [67]. In order to build the curve the assumption was made that only the average velocity of the collision was important allowing for the calculation of a higher temperature proportionally equal to the decrease in mass of the helium. By making this assumption they were able to extend their temperature range from the actually measured difference of 40K

20

to an effective range of 130 K. This data did not actually measure the pressure broadening and shifting rates as a function of temperature, rather they demonstrated that at a single pressure that the temperature affects the line shape in this way, though an extrapolation from this is not difficult to infer the rates also will be temperature dependent. The data can be seen in figure 2.9.
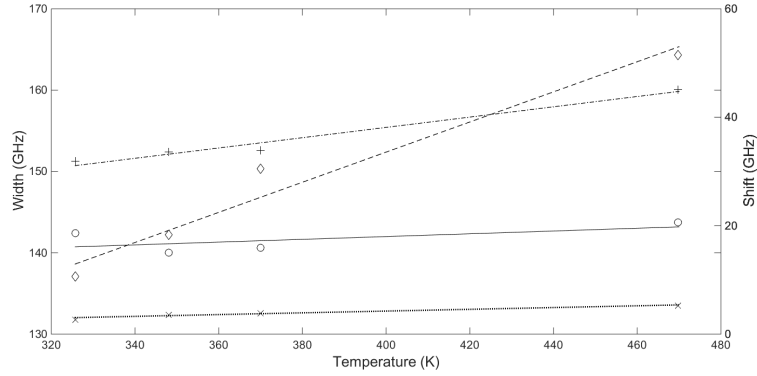
Figure 2.9: Romalis data showing FWHM and shift as a function of temperature at a constant pressure. D_1 shift (+) and broadening (0) with D_2 shift (x) and broadening (⋄). The three lower temperature data points are ^{4}He with the last being a calculated temperature using the ^{3}He data. [67]

Loper's research is focused on the theoretical calculations of the line shapes using their interaction potentials [53]. Using the potential energy curves and the Baranger model, he was able to calculate broadening and shifting rates for three temperatures for a host of alkali-noble gas partners. The values are for the D_1 and the two branches of the D_2 branch which are averaged together to give the D_2 coefficients. The relevant results are summarized in Table 2.7.

The final approach to determining the temperature dependence of the shift and broadening rates uses the semi-classical Anderson-Talman approach, discussed later in Section 2.4. Using ab initio calculated potential energy surfaces, the same ones used later

Table 2.7: Loper theoretical γ and δ calculations using ab initio potential energy curves [53]

Temp (K)	D_1 (MHz/Torr)		D_{2a} (MHz/Torr)		D_{2b} (MHz/Torr)	
	γ	δ	γ	δ	γ	δ
250	30.47	6.79	17.49	-2.35	34.59	5.17
350	23.7	6.09	14.36	-1.98	28.25	4.33
450	19.41	5.47	12.38	-1.74	24.28	3.78

by Loper, Blank was able to predict the temperature dependence of the broadening and shift rates. The predicted rates are shown in Chapter 4.3 when compared to experimental results.

2.3 DPAL Kinetics

The DPAL kinetics describes the rates of various reactions within the system. The two points of concern are the spin-orbit (SO) mixing rate, also known as relaxation, and the quenching rates. The SO mixing rate determines how fast the alkali transitions between the excited $^2P_{3/2}$ and $^2P_{1/2}$ states. The quenching rates correspond to the rate of transitions between $^2P_{3/2} \rightarrow {}^2S_{1/2}$ and $^2P_{1/2} \rightarrow {}^2S_{1/2}$ through non-radiative means which removes population that could otherwise contribute to the laser system. In a DPAL, the goal is to have the highest possible SO rate while minimizing the quenching rate.

2.3.1 Population Mechanisms and Rate Equations.

The following equations describe how the population of the system can move between the ground state $^2S_{1/2}$, N_0, the first $^2P_{1/2}$, and second $^2P_{3/2}$, $N_{1,2}$ excited states respectively [21].

$$\left[\text{Rb}\left(5\,^2S_{1/2}\right)\right] + h\nu_{20} \quad \xrightarrow{R} \quad \left[\text{Rb}\left(5\,^2P_{3/2}\right)\right], \quad \text{optical pumping} \qquad (2.10a)$$
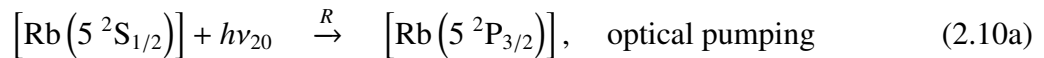
$$\left[\text{Rb}\left(5\,{}^2\text{P}_{3/2}\right)\right] \quad \xrightarrow{\xi_2 A_{20}} \quad \left[\text{Rb}\left(5\,{}^2\text{S}_{1/2}\right)\right] + h\nu_{20}, \quad \text{spontaneous emission} \qquad (2.10b)$$

$$\left[\text{Rb}\left(5\,{}^2\text{P}_{1/2}\right)\right] \quad \xrightarrow{\xi_1 A_{10}} \quad \left[\text{Rb}\left(5\,{}^2\text{S}_{1/2}\right)\right] + h\nu_{10}, \quad \text{spontaneous emissoin} \qquad (2.10c)$$

$$\left[\text{Rb}\left(5\,{}^2\text{P}_{3/2}\right)\right] + M \quad \xrightarrow{k_{20}} \quad \left[\text{Rb}\left(5\,{}^2\text{S}_{1/2}\right)\right] + M, \quad \text{quenching} \qquad (2.10d)$$

$$\left[\text{Rb}\left(5\,{}^2\text{P}_{1/2}\right)\right] + M \quad \xrightarrow{k_{10}} \quad \left[\text{Rb}\left(5\,{}^2\text{S}_{1/2}\right)\right] + M, \quad \text{quenching} \qquad (2.10e)$$

$$\left[\text{Rb}\left(5\,{}^2\text{P}_{3/2}\right)\right] + M \quad \underset{k_{12}}{\overset{k_{21}}{\rightleftarrows}} \quad \left[\text{Rb}\left(5\,{}^2\text{P}_{1/2}\right)\right] + M, \quad \text{spin-orbit mixing} \qquad (2.10f)$$

These 6 equations describe all of the various methods that population can move from one level to the next with the following variables:

[Rb] = alkali metal concentration in given level

h = Plank's Constant

R = pump rate

$\nu_{20,10}$ = frequency of transition between ${}^2\text{P}_{3/2} \to {}^2\text{S}_{1/2}$ and ${}^2\text{P}_{1/2} \to {}^2\text{S}_{1/2}$

$A_{20,10}$ = spontaneous emission rates from ${}^2\text{P}_{3/2} \to {}^2\text{S}_{1/2}$ and ${}^2\text{P}_{1/2} \to {}^2\text{S}_{1/2}$

$k_{20,10}$ = quenching rates from ${}^2\text{P}_{3/2} \to {}^2\text{S}_{1/2}$ and ${}^2\text{P}_{1/2} \to {}^2\text{S}_{1/2}$

$k_{21,12}$ = spin-orbit mixing rates between ${}^2\text{P}_{3/2}$ and ${}^2\text{P}_{1/2}$ states

$\xi_{1,2}$ = radiation trapping, discussed in Section 2.3.3

The spin-orbit mixing rates going from ${}^2\text{P}_{3/2} \to {}^2\text{P}_{1/2}$ (k_{21}) and ${}^2\text{P}_{3/2} \leftarrow {}^2\text{P}_{1/2}$ (k_{12}) are related to each other using detailed balance. Detailed balance states that the forward and backward rates are related to each other by: the number of degenerate states in each level, the energy difference between the two levels, and the temperature of the system.

$$k_{12} = \frac{g_2}{g_1} e^{-\frac{\Delta E_{21}}{k_B T}} k_{21} = \rho k_{21} = 1.25 \cdot k_{21} \qquad (2.11)$$

Once the thermally averaged rates k are determined the cross-section σ can then be calculated assuming

$$k = \bar{v}\sigma \qquad (2.12)$$

with the average speed $\bar{v}$ of the collisions being defined as

$$\bar{v} = \sqrt{\frac{8k_BT}{\pi\mu}} \tag{2.13}$$

The average speed is based upon Boltzmann's constant (k_b), the temperature (T), and the reduced mass of the collision partners (μ). The average velocity for Rb-He at 373 K is 1.437×10^5 cm/s.

2.3.2 Pulsed Experiment.

For a pulsed experiment where the pump is only on for a very short amount of time the coupled rate equations for the system can be written as [70]:

$$\begin{pmatrix} \dot{N}_2 \\ \dot{N}_1 \end{pmatrix} = \begin{bmatrix} -(\xi_2 A_{20} + \gamma_{20} + \gamma_2 1) & R + \rho\gamma_{21} \\ \gamma_{21} & -(\xi_1 A_{10} + \gamma_{10} + \rho\gamma_{21}) \end{bmatrix} \begin{bmatrix} N_2 \\ N_1 \end{bmatrix} \tag{2.14}$$

The pump rate, R, in equation 2.14 can be turned into an initial condition if the pulse duration is short compared to the timescales of other decay mechanisms. When the condition of a short pulse is met equation and the pump rate is turned to an initial condition the time dependent solution for I(t) comes from solving for the eigenvalues of Equation 2.14 and is given as:

$$I(t) = C(e^{-\lambda_- t} - e^{-\lambda_+ t}) \tag{2.15}$$

Solving for the eigenvalues of equation 2.14 we get solutions:

$$\begin{aligned} \lambda_\pm = &-\frac{1}{2} \left[\xi_1 A_{10} + \xi_2 A_{20} + \gamma_{10} + \gamma_{20} + \gamma_{21} (1 + \rho) \right] \\ &\pm \frac{1}{2} \left(\left[(\xi_1 A_{10} + \gamma_{10}) - (\xi_2 A_{20} + \gamma_{10}) \right]^2 + (1 + \rho)^2 \gamma_{21}^2 \right. \\ &\left. + 2\gamma_{21} \left[(\xi_1 A_{10} + \gamma_{10}) (\rho - 1) + (\xi_2 A_{20} + \gamma_{10}) (1 - \rho) \right] \right)^{1/2} \end{aligned} \tag{2.16}$$

The trapping coefficients, $\xi_{1,2}$, relate to how many times the photon is absorbed and re-emitted before reaching the edge of the cell. The γ_{21}, γ_{20}, γ_{10} variables are defined as

$k_{21}[M]$, $k_{20}[M]$, and $k_{10}[M]$ respectively where [M] is the number density of buffer gas. Our initial conditions coefficient, C, is dependent upon the pressure of the buffer gas within the system as is described by the equation:

$$C = \frac{\gamma_{21}}{\left(\left[(\xi_1 A_{10} + \gamma_{10}) - (\xi_2 A_{20} + \gamma_{10}) \right]^2 + (1 + \rho)^2 \gamma_{21}^2 \right.}{\left. + 2\gamma_{21} \left[(\xi_1 A_{10} + \gamma_{10})(\rho - 1) + (\xi_2 A_{20} + \gamma_{10})(1 - \rho) \right] \right)^{1/2}} \tag{2.17}$$

When ρ is approximately equal to 1, ie. the rate going up is equal to the rate going down, equations 2.16 and 2.17 can be reduced to:

$$\lambda_{\pm} = -\frac{1}{2} \left[\xi_1 A_{10} + \xi_2 A_{20} + \gamma_{10} + \gamma_{20} + 2\gamma_{21} \right] \pm \frac{1}{2} \sqrt{\left[(\xi_1 A_{10} - \xi_2 A_{20}) + (\gamma_{10} - \gamma_{20}) \right]^2 + 4\gamma_{21}^2} \tag{2.18}$$

$$C = \frac{\gamma_{21}}{\sqrt{\left[(\xi_1 A_{10} - \xi_2 A_{20}) + (\gamma_{10} - \gamma_{20}) \right]^2 + 4\gamma_{21}^2}} \tag{2.19}$$

The above equations can be simplified further if there is no trapping in the system. With no trapping, or very little trapping, ξ become equal to 1. Another assumption that can be made to simplify the equations and is approximately true is that the quenching rates, γ_{20} and γ_{10}, are approximately equal. Using these assumptions Equations 2.18 and 2.19 reduce down to:

$$\lambda_{\pm} = -\frac{1}{2} \left[A_{10} + A_{20} + 2\gamma_{10} + 2\gamma_{21} \right] \pm \frac{1}{2} \sqrt{\left[(A_{10} - A_{20}) + \right]^2 + 4\gamma_{21}^2} \tag{2.20}$$

$$C = \frac{\gamma_{21}}{\sqrt{\left[(A_{10} - A_{20}) \right]^2 + 4\gamma_{21}^2}} \tag{2.21}$$

Using Equation 2.15 to fit the data, a sample of which can be seen in Figure 2.10, the values for C and the eigenvalues can be determined. Then using equations 2.20 and 2.21 k_{21}, k_{20}, and k_{10} can be calculated. Taking the difference of the eigenvalues will provide k_{21} and $k_{10} - k_{20}$ while the addition of the eigenvalues will provide $k_{10} + k_{20}$. Solving these two equations simultaneously will provide the final values with Equation 2.21 being used as a independent check.
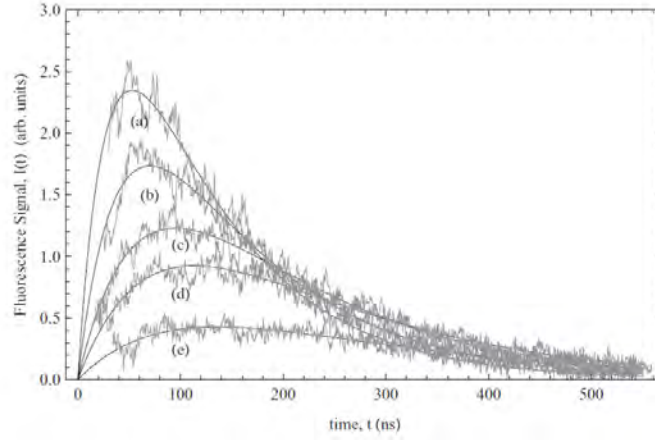
Figure 2.10: Experimental data from a pulse SO mixing experiment showing the decay curves of Cs-He $7P_{1/2}$-$6S_{1/2}$ transition. The buffer gas pressures in torr a) 2.0 b) 1.2 c) 0.6 d) 0.4 e) 0.2 [21]

2.3.3 Radiation Trapping.

Radiation trapping is the process by which a captured photon may be absorbed and emitted multiple times before reaching the edge of the gain cell. Two main factors determine the magnitude of the radiation trapping in a system. The first, volume of the cell. The larger the distance that the photon must travel to reach the edge of the cell, the greater the probability of collision leading to absorption. The second factor is the alkali density within the cell. High alkali density increases the probability that an emitted photon will be reabsorbed before reaching the edge. Radiation trapping therefore increases the timescale of the decay curve. Therefore in order to ascertain the correct rates, the trapping must be calculated and accounted for.

At times the experiment may actually encourage this radiation trapping to extend the decay lifetime of the signal. By extending the decay time it becomes easier to deconvolve the initial pulse of the laser if that pulse is on the order of the decay time. While this does allow for longer pulse lasers to be used for this type of experiment that uncertainty inserted

26

into the calculations by this random process introduces more errors. To avoid the necessity of extending the decay times a pulsed laser source with a much shorter pulse duration than the decay time can be used.

The following discussion of the proposed experiments avoid the problem of radiation trapping all together, which is the best option if available. In order to completely avoid the trapping the alkali density within the cell is kept low via the use of an alkali metal dispenser. A ∼100 pico-second laser will also be used in order to avoid the necessity of extending the decay time and therefore removing the requirement to do radiation trapping.

2.3.4   *Continuous Wave (CW) Experiment.*

For the CW experiment, the major difference from the pulsed experiment is how the rate equations change. The equations that describe population movement stay the same. In the pulsed experiment rate equations were solved by finding the eigenvalues of coupled rate equations. In the CW experiment the system has reached a steady state and the change in the population of N_1 and N_2 is equal to zero, allowing for a direct solution of the rates. The relative populations of each level when pumping the $^2P_{3/2}$ are given as [64]:

$$\left[\frac{N_1}{N_2}\right]_{PumpD_2} = \left(\frac{I_{D_1}}{I_{D_2}}\right)\left(\frac{d_2}{d_1}\right) = \frac{k_{12}[M]}{A_1 + (k_{10} + k_{21})[M]} \tag{2.22}$$

and when pumping the $^2P_{1/2}$ state:

$$\left[\frac{N_2}{N_1}\right]_{PumpD_2} = \left(\frac{I_{D_2}}{I_{D_1}}\right)\left(\frac{d_1}{d_2}\right) = \frac{k_{21}[M]}{A_2 + (k_{20} + k_{12})[M]} \tag{2.23}$$

where I_{D_1} and I_{D_2} are the intensities recorded from the side fluorescence using the band pass filters. The detectivity of each detector is given by d_1 for detector one and d_2 for detector two.

In this type of experiment the intensity of both the D_1 and D_2 transitions are monitored as shown in the experimental setup of figure 2.11. Some of the data from the experiment by Pitz can also be seen in figure 2.11. The cross-section in this experiment as well as the previously described pulsed experiments assumes that the cross-section σ is independent

27

of temperature. This may make a difference in the rates if the average speed is not the only

parameter that depends upon the temperature of the system.
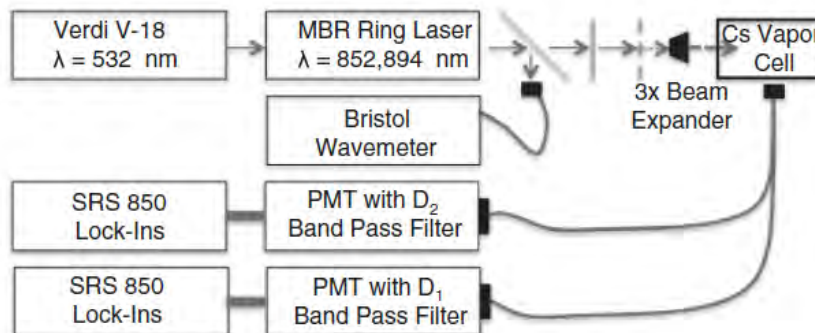
Figure 2.11: Experimental setup for CW SO-mixing from Pitz [64]
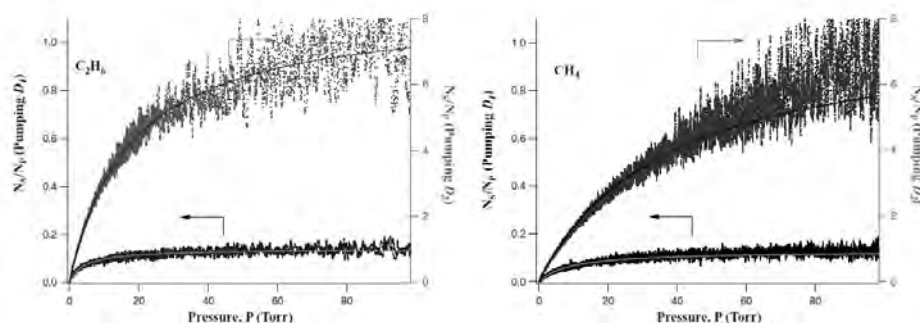
Figure 2.12: Sample experimental data from CW SO-mixing experiment [64]

2.3.5 *Temperature Dependent Mixing Rates.*

The spin-orbit mixing rates have now been discussed along with the various methods

used to determine them. The temperature dependence of these rates, as with the line shape

parameters is the main focus of this research. To that end the best information available with

respect to the rates come from Gearba [29] at the Air Force Academy for the experimental

28

side, and from the theoretical side Lewis [51]. The data from Gearba is compared with the earlier works by Gallagher [28], Krause [45], and Beahn [9] in Figure 2.13.
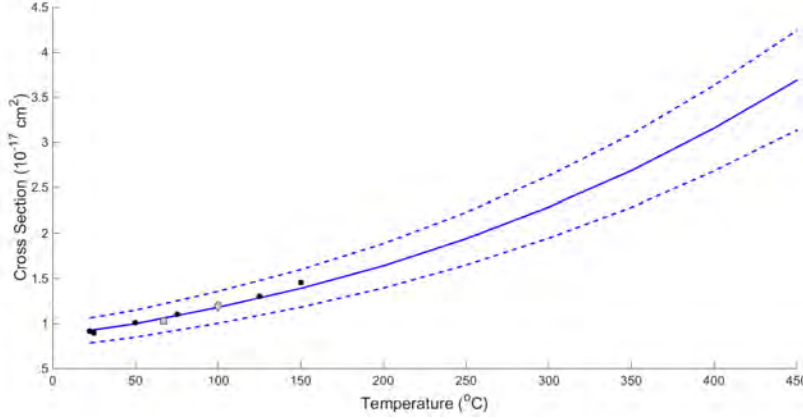
Figure 2.13: Temperature dependence of spin-orbit mixing rates from Gearba [29] as solid circles, Krause [45] as the square, Beahn [9] as the diamond, and Gallagher [28] as the solid line with 15% error bounds.

The work done by Lewis for his computational modeling done for his dissertation can be seen compared to Krause and Beahn in Table 2.8.

2.4 Anderson Tallman Line Broadening Theory

2.4.1 Potential Energy Curves.

A potential energy curve (PEC) describes the interaction forces between two non-interacting atoms or molecules. The potential between the two atoms can be considered to be zero at infinity and has some structure as the two object move closer together due to the forces involved. In 1924 J. E. Jones published in the Royal Society of London his mathematical fitting to the interaction potentials of experimental argon [40]. In his explanation of the potential energy curve between two argon atoms he developed what

29

Table 2.8: Lewis [51] computational calculations of SO rates with comparisons to experiment.

Q($^2P_{3/2} \leftarrow {}^2P_{1/2}$)	RbHe	Temp (K)
Krause [45]	$0.27 \pm .027$	340.15
Predicted SO	0.10	
Predicted SO + Coriolis	0.39	
Beahn [9]	0.36 ± 0.036	373.15
Predicted SO	0.13	
Predicted SO + Coriolis	0.45	

became known as the Lennard-Jones or 12-6 potential. He expressed the potential as:

$$V = 4\epsilon \left[\left(\frac{\sigma}{r} \right)^{12} - \left(\frac{\sigma}{r} \right)^{6} \right] \tag{2.24}$$

where ϵ is the well depth, σ is the van der Waals radius of the particle, and r is the spacing between the two particles. In equation 2.24 the term raised to the twelfth power is the repulsive force between the particles and the term raised to the sixth is the attraction.

David Weeks and L. Blank have created ab initio potential energy curves for the cesium-helium [15]. A sample of one of their PECs is shown in figure 2.14

2.4.2 Broadening and Shift.

In 1956 P. Anderson-J. Talman published their Unified Theory of pressure broadening [4]. In the Anderson-Talman theory the line shape of a transition is created by taking the Fourier transform of the auto-correlation function for a single emitter. Kielopf then gives a modified expression for the line shape given as [43]:

$$I(\nu) = 2 \left(\frac{c}{\bar{\nu}} \right) \int_0^\infty e^{-n\alpha(u)} cos \left[(2\pi c\nu/\bar{\nu}) - n\beta(u) \right] du \tag{2.25}$$
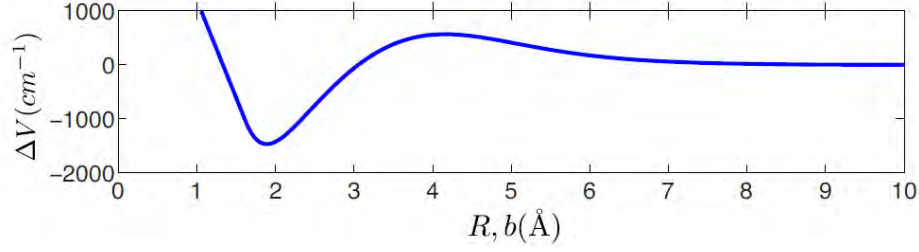
Figure 2.14: Sample potential energy curve for the cesium-helium interaction created by Weeks and Blank for use in testing line-broadening theories [15]

The variables for the line shape include:

ν = emitter frequency in wavenumbers (cm^{-1})

u = correlation distance = $w\tau$

$\bar{v} = \sqrt{\frac{8kT}{\pi\mu}}$ = average relative speed of collision pair

μ = reduced mass of collision pair

τ = correlation time

c = speed of light

The real part, α of the accumulated phase difference:

$$\alpha(u) = \int_{-\infty}^{\infty} dx_0 \int_{0}^{\infty} 2\pi b \left(1 - cos[\theta(x_0, b, u)]\right) db \qquad (2.26)$$

with the imaginary portion, β,

$$\beta(u) = \int_{-\infty}^{\infty} dx_0 \int_{0}^{\infty} 2\pi b \left(sin[\theta(x_0, b, u)]\right) db \qquad (2.27)$$

The function $\theta(x_0, b, u)$ is the accumulated phase shift on collision:

$$\theta(x_0, b, u) = 2\pi \left(\frac{c}{\bar{v}}\right) \int_{0}^{u} \Delta V \left(\sqrt{(x_0 + u')^2 + b^2}\right) du' \qquad (2.28)$$

Then assuming a large correlation distance α and β can be written as linear functions

$$\alpha(u) = \alpha_0 + \alpha_1 u \qquad (2.29)$$

$$\beta(u) = \beta_0 + \beta_1 u \tag{2.30}$$

Combining these equations results in the full intensity profile which is the full form of equation 2.4 expanded to include the non-linear term that dominates in the wings

$$I(v) = I_L(v) + I_A(v) + I_{NL}(v) \tag{2.31}$$

$I_L(v)$ is given by equation 2.5 with $I_A(v)$ defined by equation 2.6 and the final term:

$$I_{NL}(v) = 2\left(\frac{c}{w}\right) \int_0^u \left[e^{-n\alpha(u')} cos\left(\frac{2\pi c}{w}u'v - n\beta(u')\right) - e^{-n(\alpha_0 + \alpha_1 u;)} cos\left(\frac{2\pi c}{w}u'v - n(\beta_0 + \beta_1 u')\right) \right] du' \tag{2.32}$$

III. High-Pressure Lineshape

3.1 Introduction

The diode-pumped alkali laser (DPAL) was proposed in 2001 as an alternative to high-power, diode-pumped, solid-state lasers [46, 48]. The radiation from the un-phased diode laser bars or stacks are absorbed on the D_2 $^2S_{1/2} \rightleftarrows {}^2P_{3/2}$ transition and collisional energy transfer to the spin-orbit split $^2P_{1/2}$ state yields lasing on the D_1 $^2P_{1/2} \rightleftarrows {}^2S_{1/2}$ transition in potassium, rubidium, or cesium vapor.

A rubidium laser pumped by a 1.28 kW diode stack with a 0.35-nm bandwidth has achieved 145-W average power [88]. More recently, 1 kW Cs laser with closed loop transverse flow was demonstrated with 48% optical-to-optical efficiency [18]. The fine structure splitting in Cs is large, and hydrocarbon collision partners are generally required to prevent bottlenecking. The presence of hydrocarbons can lead to soot and alkali hydride formation [47]. In contrast, helium is sufficient to induce fine structure mixing in Rb with the rates required to support high power development [56]. Helium pressures of 10-20 atmospheres are required to avoid bottlenecking on the fine structure mixing and to broaden the absorption line shapes sufficiently to accept modestly narrowed diode bar radiation. Characterizing the high pressure Rb-He line shapes is critical to: (1) design the pump diode spectral band, (2) design the optical resonator, (3) assess the effects of atmospheric transmission on high power propagation, and (4) evaluate the rates of ionization via far wing absorption. In this chapter we observe and compare with theory the high-pressure line shapes for the Rb D_1 and D_2 lines induced by collisions with ^{4}He and ^{3}He.

The Rb-He gas line shapes near resonance (in the core) have been investigated experimentally in considerable detail [12, 31, 39, 42, 44, 54, 60, 65, 67, 68, 71, 76, 83]. The broadening and shifting rates for the Rb D_1 line induced by collisions with ^{4}He using modern methods agree to within better than 4% [54, 65, 67, 68, 83]. The agreement for the

D_2 line is poorer, with a 9% variance for the broadening rate and 20% for the shift rate. The shift rate for the D_2 line is small due to the combined effects of two electronic surfaces. The temperature range where these rates have been determined is modest, 314-394 K, and span several different studies. Older measurements during the period 1940-1980 exhibit a 30% variance in broadening rates and disagree on the sign of the shift [12, 31, 39, 42, 60, 71, 76]. The corresponding rates for collisions with ^{3}He were all performed at high pressures, >1 atm, and vary by about 20% [44, 50, 67].

Several computational approaches have also been applied to compute the broadening and shift rates [14, 15, 43, 53, 69]. However, the results are sensitive to the long range portion of the interaction potentials. Indeed, the two ab inito potentials [16, 55] used in our recent study of Cs line shapes [34] both require empirical modification to adequately describe the observed spectra. Furthermore, different line shape theories applied to the same interaction potentials do not agree on the sign of the shift for the Rb-He interaction [15].

In the current work we focus on the high pressure, non-Lorentzian behavior of the Rb-He D_1 and D_2 line shapes. For pressures exceeding 1,000 Torr, a significant asymmetry has been observed in the core of the line, [54, 65, 67] as predicted by several theoretical calculations [19, 22, 26, 41]. However, the magnitude of the asymmetry is not well predicted and further refinement of the interaction potential appears necessary [43]. A blue satellite is observed in the far wing of the Rb D_2 line and is most pronounced for the heavier rare gases [2, 19, 22, 26, 41]. A comparison of the theoretical predictions for the far wing spectra of Rb-He over a broad range of temperatures has recently been published [19]. In the recent work, potential surfaces were generated using SA-CASSCF-MRCI calculations. In this paper we report observations of the absorption spectrum in far wings of the Rb D_2 and D_1 lines perturbed by ^{4}He and ^{3}He at pressures as high as 15,000 Torr. We then employ the Anderson-Talman theory, [3, 4] including the effects of dipole

moment variation, [1] to predict the line shapes. The sensitivity of dipole moment variation on the wing line shapes is also evaluated. Our longer-term goal is to unify the Rb-He DPAL kinetics with potential surfaces that are sufficient to predict the temperature dependence of the fine structure mixing rates and collisional line shape parameters.

3.2 Experiment

Absorption spectra for rubidium vapor in the spectral range 600-875 nm were observed using a grating monochromator, as shown in Figure 3.1. The broadband visible emission from an Ealing 100 Watt tungsten lamp, with Oriel 68831 300 W lamp power supply, was collimated with an f=2.5 cm lens to pass through a Rb sample maintained in a gas recirculation cell. The transmitted light was focused with another f=2.5 cm, 5 cm diameter lens onto the entrance slit of a McPherson model 209 f=1.33 m (f/#=9.4) monochromator. With a 500 nm blaze, 1200 gr/mm grating and slits widths of 20.8 μm for the entrance and 34.7 μm for the exit, the instrumental line shape exhibited a full width at half maximum spectral resolution of 0.05 nm (24.7 GHz). An Ultraviolet Products krypton pen lamp was positioned at 17 mm in front of the monochromator entrance slit to provide dynamic wavelength calibration. Wavelength calibration was stable to within 0.035 nm from over 6 months of data acquisition.

An uncooled Burle C31034A photomultiplier tube biased at 1,275 V exhibited a dark signal bias of 4-6 nA with noise fluctuation of 0.04 nA, as monitored on a Keithley model 386 picoammeter with 0.175 integration time. Monochromator scan rates of 0.32 nm/min required approximately 11 hours to obtain a full spectrum across the range 670-880 nm. The spectrum is sampled 11 times for each digital step in wavelength of 0.01 nm. The unattenuated lamp signal was typically 110-120 nA with noise of 0.25-0.35 nA. The minimum detectable absorbance:

$$A = -ln\left[I_t(\lambda)/I_0(\lambda)\right] \tag{3.1}$$
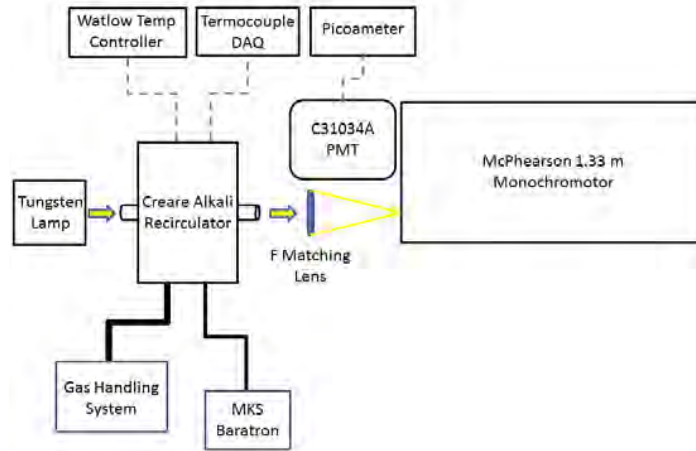
Figure 3.1: Experimental setup for the High-Pressure Lineshape Study

where

$I_t(\lambda)$ = transmitted intensity with Rb vapor in the path

$I_o(\lambda)$ = transmitted intensity without Rb vapor in the path

was limited by the detector noise at A= 0.005. The maximum detectable absorbance was limited by baseline drift and noise at A= 2.1. Absorbance was stable to within 2% over a 13-hour period for a cold cell. Cell window transmission degraded by about 60% over a 6-month period.

A spectral baseline, $I_o(\lambda)$, was obtained by recording the transmitted intensity with the circulator operated at 296 K (Rb density, $n < 10^{10} atom/cm^3$) and evacuated conditions to minimize the spectral absorption. A 9th order polynomial fit for the average of several observed baselines before and after allows interpolation across the weak and narrow D_1 and D_2 line positions. This baseline had no theoretical basis and was chosen because it provided the best fit to the cold scan data. The stability of the observed baselines was affected primarily by changes in the circulator window transmission. The transmitted signal at 735

36

nm with the circulator operating at 513 K varied from 38.5-41.0 nA, or by 6.5% during a 13 hour observation.

A schematic of the gas circulator and gas handling system is provided in Figure 3.2. The gas bearing turbo machinery circulator provides mass flow rates of up to 1 g/s. In the current experiments, stagnant, non-flowing circulator conditions were employed. The Monel 400 walls and stainless steel 316 valves were not degraded throughout the testing period. The optical path length with Rb vapor is 8.125 cm and accessed through 4 fused silica windows. Temperatures of 333-533 K were monitored by type K thermocouples and controlled in four zones with a Watlow controller, to yield rubidium densities of n = 2.5 x 10^{11} - 6.3 x 10^{15} atoms/cm^3. The windows were kept at 5-10 K hotter than the test cell to minimize plating. Rubidium density is stable to within 2% over a 13 hour period. However, there is a periodic variation of temperature, due to the control system response time of 3.5 min, of $\Delta T = 3$ K. This produces a variation in absorbance of up to $\Delta A = .02$ at the highest temperatures, and is corrected as discussed below.

Approximately 1 g of Alfa Aesar 99.75% purity, natural isotopic abundance rubidium was loaded into the circulator in a nitrogen purged dry box. This single charge of rubidium was not depleted or reacted during the 9 months of operation. Linde 99.9999% ^{4}He and Spectra Gases, 99.9% ^{3}He was introduced through a SAES heated getter and 0.003 μm filter to remove atmospheric gases, CO, and H_2 to <1 ppb. A Varian EX9698996 turbo pump was used to evacuate the circulator. Pressure was measured with a 15,000 Torr MKS model 609A manometer and 670 signal conditioner. Line shapes for gas pressures of 500 - 15,000 Torr were observed. Pressure measurements are performed and reported at the elevated cell temperatures. The pressure transducer is protected behind a stainless steel valve during the longer spectral scans.
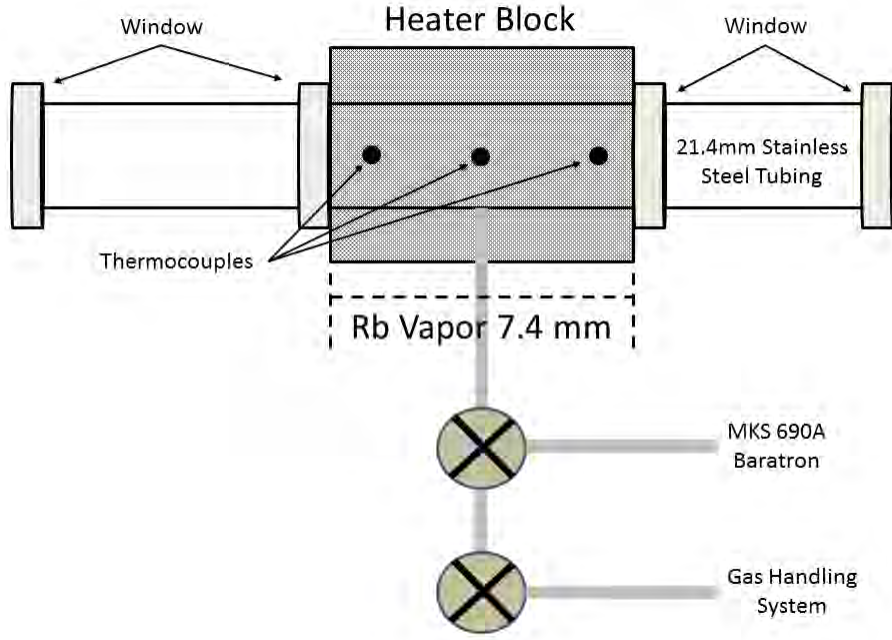
Figure 3.2: Diagram of the high-pressure Creare Cell used in experiment

3.3 Observed Spectra

The transmitted intensity as a function of monochromator wavelength for several rubidium densities and [4]He pressure of 10,000 Torr is provided in Figure 3.3. The various spectral features are assigned to the strongly absorbed Rb D_1 and D_2 lines, the weaker Cs D_2 line at 852.1 nm due to sample impurity, the Kr lamp calibration lines, and for the higher Rb densities, the vibrational bands of the Rb$_2$ $X^1\Sigma_{g^+} - B^1\Pi_u$ electronic transition. The broad blue satellite of the Rb D_2 line can also been seen in the higher Rb density scans near λ = 735 nm. The absorbance in the blue satellite is 0.03% of the line center absorbance at 10,000 Torr. The core of the Rb D_2 and D_1 lines become highly opaque for T > 400 K. The relative height of the Cs D_2 line suggests ~0.047% Cs in the sample. The potassium lines near 770 nm and 766 nm are very weak in the current spectra. At T = 333 K, the ratio of

Rb dimer to atom concentrations is 7×10^{-5} and grows dramatically to 4×10^{-3} at T = 533 K [59]. Fortunately the Rb_2 absorbance is spectrally isolated from the atomic lines.
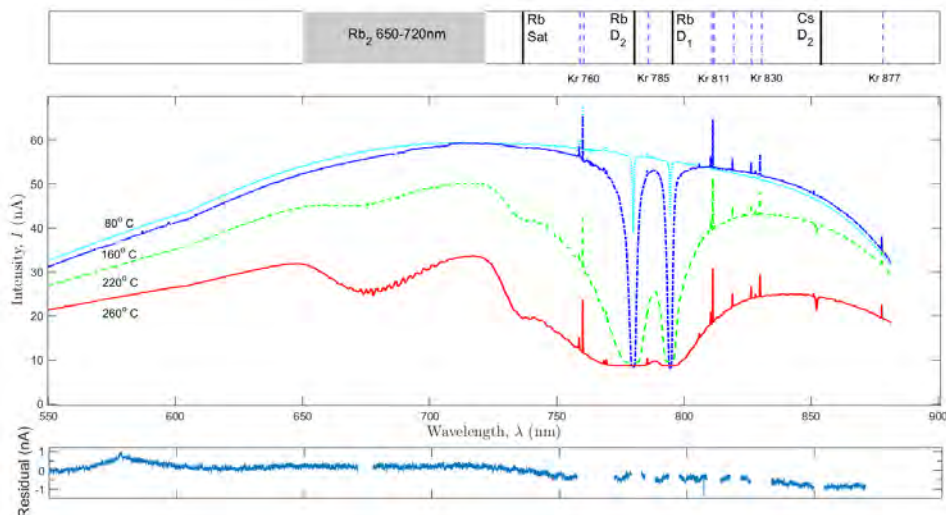
Figure 3.3: Monochromator spectrum at T=353 - 533 K and ^{4}He pressure of 10,000 Torr. Spectral features are assigned in the upper banner and the fit residuals for a 9th order polynomial in regions without spectral structure is provided in the lower panel.

The transmitted intensity of Figure 3.3 is converted to absorbance, A, in Figure 3.4, using Beer's Law and the baseline spectrum from the cold scans as described above. The bottom panel in Figure 3.3 illustrates the residuals associated with the baseline polynomial fit to the data. In the regions with no atomic or molecular features, the residuals are unstructured with an average variance of $\Delta I = 1 \times 10^{-9}$ A or approximately 2-5%. By examining the absorbance in the spectral region near the Rb D_2 and D_1 lines only, several new features are revealed. A slow saw-tooth cycling of temperature of 3 K (peak to valley) with a regular period of 3.5 minutes leads to a periodic variance in absorbance of up to $\Delta A = 0.02$. This variance is fully removed by processing the data with the thermocouple readings, as shown below. The absorbance due to the atmospheric O_2 $X^3\Sigma - b^1\Sigma(0,0)$ band near 762 nm is rotationally resolved. The absorbance of A=0.02 is consistent with a path

length of 2 meters, largely within the monochromator. Additional detail from the Kr lamp is also evident in Figure 3.4.
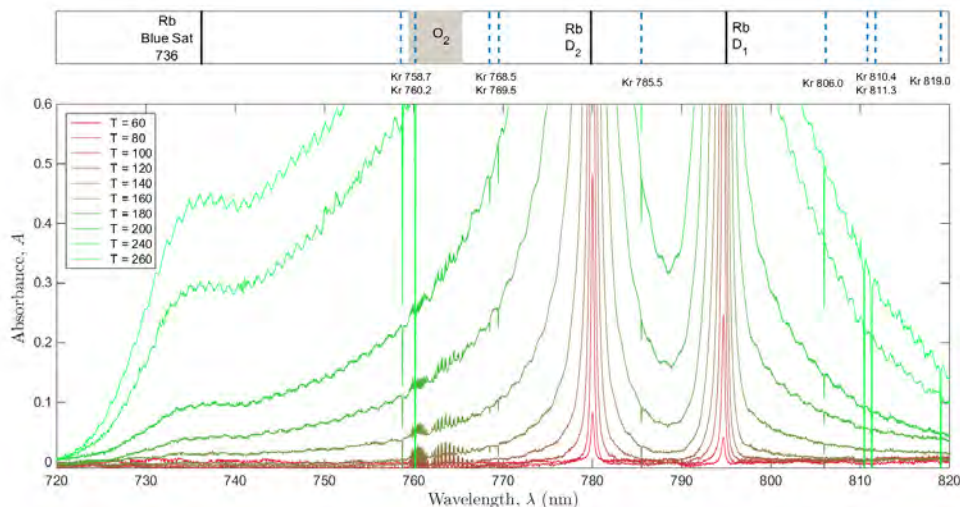
Figure 3.4: Absorbance spectra corresponding to the data in Figure 3.3. The magnetic dipole selection rules, Hunds case (b), produces four $O_2(b^1\Sigma \rightarrow X^3\Sigma)$ absorption branches: ^PP and ^PQ, beginning near 762 nm and extending beyond 770 nm, and the ^RQ and ^RR lines from 762-759 nm.

At lower Rb densities, the core of the line shape is not opaque and the rates for collisional broadening, shifting and asymmetry may be evaluated. Figures 3.5 and 3.6 illustrates the observed line shapes for both the Rb D_2 and D_1 lines for ^{4}He and ^{3}He pressures of 500-15,000 Torr at 343 K. The D_1 lines exhibit a significant shift of the center frequency to the blue. In contrast, the D_2 lines exhibit a small blue shift. In all cases, the widths of the spectral features are 240-290 GHz at the highest pressure, depending on transition and buffer gas. The areas under these curves are nearly constant, varying by 18% for D_1 and 8% for D_2 due to modest changes in alkali density.

The Anderson-Talman theory for the line shape, limited to the low-pressure core of the line, can be expressed as two terms:
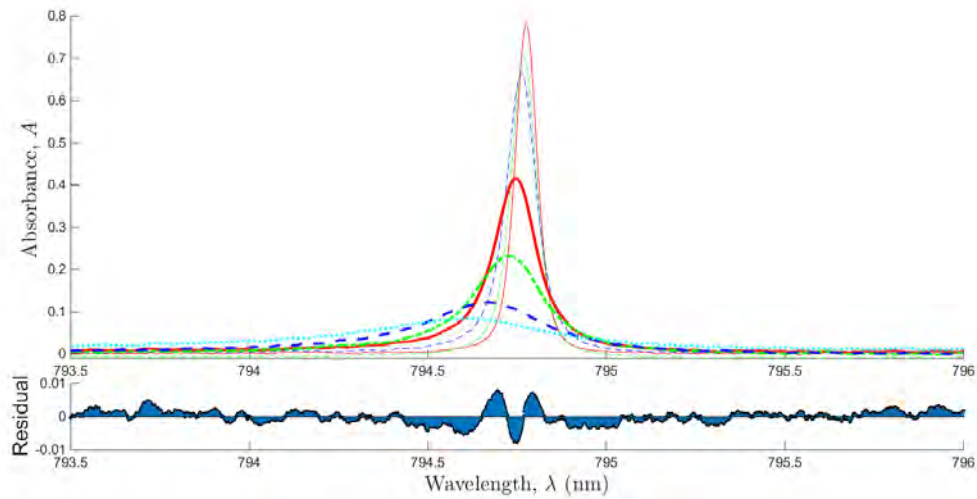
(a) D_1 ^{4}He
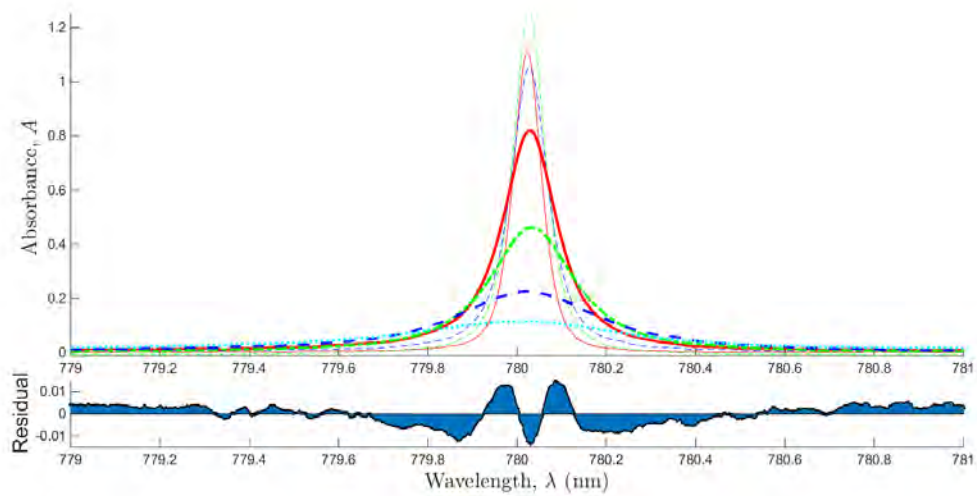
(b) D_2 ^{4}He

Figure 3.5: Core line shapes for (a) Rb D_1-^{4}He and (b) Rb D_2-^{4}He, at pressures from narrowest to widest of (—) 512 Torr, (–·–) 997 Torr, (- - -) 1,544 Torr, (...) 2,005 Torr, (——) 3,006 Torr, (—·—) 5,490 Torr, (‐ ‐ ‐) 9,988 Torr, (...) 15,039 Torr.

41
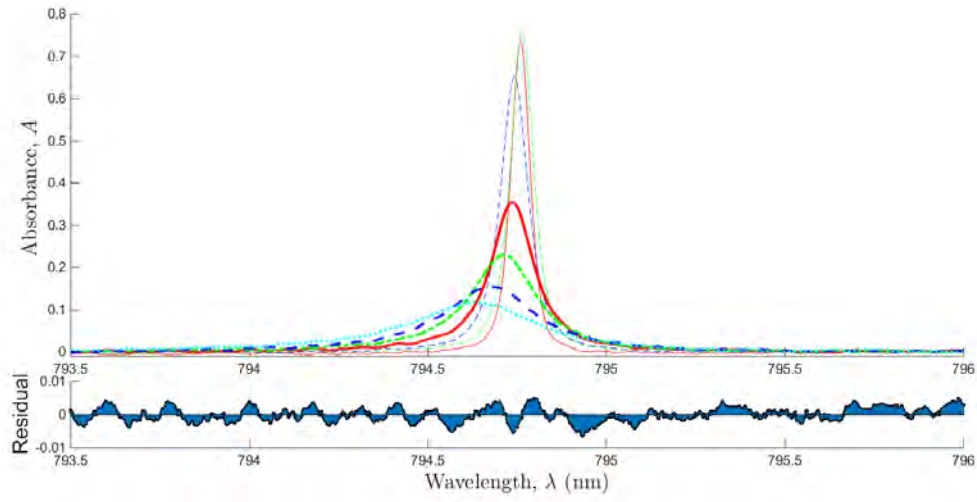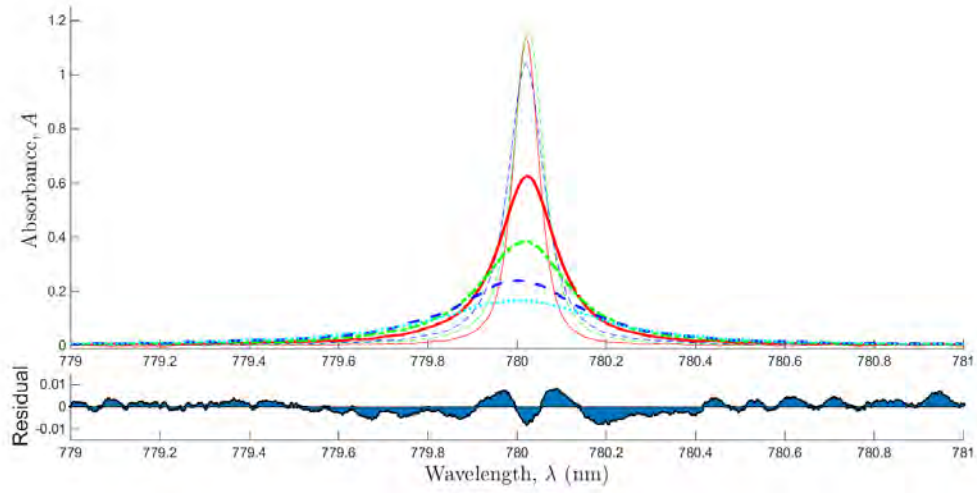
(a) D_1 ^{3}He

(b) D_2 ^{3}He

Figure 3.6: Core line shapes for (a) Rb D_1-^{3}He and (b) Rb D_2-^{3}He, at pressures from narrowest to widest of (—) 502 Torr, (–·–) 998 Torr, (- - -) 1,498 Torr, (...) 1,994 Torr, (——) 3,015 Torr, (—·—) 5,001 Torr, (- - -) 7,500 Torr, (...) 10,062 Torr.

42

$$I(v) = 2\left(\frac{c}{\bar{v}}\right)e^{-n\alpha_0}\frac{\left[cos(n\beta_0)(n\alpha_1) + sin(n\beta_0)\left(\frac{2\pi c}{\bar{v}}v - n\beta_1\right)\right]}{(n\alpha_1)^2 + \left(\frac{2\pi c}{\bar{v}} - n\beta_1\right)^2} \tag{3.2}$$

where the first term is nearly Lorentzian at low perturber density, n, and represents the pressure broadened and shifted line core. The second term has a dispersive shape, with asymmetric shading. The rate for pressure broadening of the core Lorentzian, γ, is normally defined from the low pressure line shapes by the full-width half-maximum (FWHM) line width and expressed with units of MHz/Torr:

$$\Delta v_{FWHM} = \gamma P + \Delta v_n \tag{3.3}$$

where Δv_n is natural broadening and

$$\gamma = \left(\frac{2\bar{v}}{\pi c}\right)\left(\frac{c}{kT}\right)\alpha_1 \tag{3.4}$$

Similarly, the rate for the pressure-induced shift of the line center is:

$$\delta = \left(\frac{2\bar{v}}{2\pi c}\right)\left(\frac{c}{kT}\right)\beta_1 \tag{3.5}$$

Finally, the asymmetry of the line shape, or how much of a tail the line shape has to one side compared to the other, is described by the parameter, β_o.

A fit of equation (2) to the full set of data for T = 343 K similar to that provided in Figures 3.5 and 3.6 yields the rate parameters reported in Table 3.1. The fits are limited to the core of the line, defined as the signal near resonance from 25% of the peak to the peak. The wing of the lines and secondary maximum are not described by equation 3.2 and are discussed further below. The quality of the fits is indicated by the residuals displayed in Figures 3.5 and 3.6. Typically, 8 spectra were recorded at pressures of 50-15,000 Torr. Linear fits yield the rates in Table 3.1 with uncertainties reported as the 95% confidence interval.

Table 3.1: Pressure Broadening and Shift Rates

	D_1	D_2	Temperature	Reference
^{4}He Broadening γ (MHz/Torr)	16.1 ± 0.2	17.0 ± 0.3	343	Experiment
	17.6 ± 0.1	16.5 ± 0.1	353	[65]
		20.3 ± .3	314	[83]
	18.9 ± 0.2	20.0 ± 0.2	394	[68]
	18.3 ± 0.2	18.4 ± 0.2	353	[67]
	17.9 ± 0.2		373	[54]
	19.0 ± 2.0	15.0 ± 2.0	320	[39]
	18.3 ± 0.9			[42]
		22.5 ± 1.1	310	[12]
	18.5 ± 3.4	18.5 ± 3.4	320	[60]
	19.3	18.1	313	Theory
	21.6	19.8	394	[15]
	15.7	21.3	394	[53]
	14.3	14.3	320	[43]
	17.1	12.5	450	[69]
^{4}He Shift δ (MHz/Torr)	4.60 ± .12	.20 ± .14	343	Experiment
	4.57 ± .02	0.28 ± .05	353	[65]
		0.39 ± .06	314	[83]
	4.71 ± .04	0.37 ± .06	394	[68]
	4.40 ± 0.1	.47 ± .06	353	[67]
	5.0 ± 1.0	0.9 ± 0.2	320	[39]
	6.2 ± 0.5			[42]
		2.2 ± 0.5	310	[12]

Continued on next page

	D_1	D_2	Temperature	Reference
		-0.74 ± 0.34	320	[60]
	4.66	0.20	393	Theory
	5.8	1.10	394	[15]
	-5.8	-1.13	394	[53]
	1.09	1.09	320	[43]
	4.13	1.76	450	[69]
^{4}He Asymmetry β_0 (rad nm^3)	0.51 ± .04	0.24 ± .02	343	Experiment
	-0.98 ± 0.03	-0.12 ± 0.03	353	[67]
	-0.61 ± 0.03	-0.14 ± 0.04	353	[65]
	1.1	0.3	313	Theory
^{3}He Broadening γ (MHz/Torr)	16.8 ± 0.5	19.4 ± 0.4	343	Experiment
	19.0 ± 0.3	21.2 ± 0.2	353	[67]
	18.12 ± 0.07	20.30 ± 0.08	363	[44]
	26.32		393	[50]
	19.6	20.1	393	Theory
^{3}He Shift δ (MHz/Torr)	5.65 ± 0.35	0.65 ± 0.2	343	Experiment
	5.4 ± .05	.62 ± .04	363	[44]
	6.32		393	[50]
	5.74 ± 0.15	0.69 ± 0.05	353	[67]
	5.45	-0.01	393	Theory
^{3}He Asymmetry β_0 (rad nm^3)	0.43 ± 0.01	0.30 ± 0.03	343	Experiment
	-0.55 ± 0.03	-0.24 ± 0.03	353	[67]
	0.50	0.125	333	Theory

The prior experimental ^{4}He broadening rates for the D_2 line vary from 14.3-22.5 MHz/Torr and were measured in a modest temperature range of 310-394 K. The modern results (since 1990) are more closely grouped with an average of 18.8 ± 1.7 MHz/Torr. Scaling the rates to a common temperature requires a prediction of the temperature dependent cross-section, [34, 63, 66, 83] but only marginally reduces the variation in the results. The current observation is somewhat lower at 17.0 ± 0.3 MHz/Torr, just outside of the range of the modern measurements. The modern D_1 rates exhibit a smaller range with an average of 18.2 ± 0.6 MHz/Torr, and the present result is again somewhat low. The grating spectrometer employed in the current work is designed to examine the far wings of the lineshapes and has poorer spectral resolution than the laser absorption experiments. The preferred results are from references [67, 68, 83].

It is worth noting that the theoretical predictions for the D_1 broadening rate, even when using the same interaction potentials and temperature, vary from 15.7-20.2 MHz/Torr. The semi-classical Anderson-Tallman line shape theory predictions [15] and the full quantum mechanical Baranger calculations done by Loper [53] yield predictions that vary by more than the range of experimental observations. The Anderson-Talman theory for the full line shape is discussed in Section 3.4.3.

Comparing the ^{4}He and ^{3}He results reveals an interesting trend. For the D_2 line the current ^{3}He rate is 4% larger than the ^{4}He rate, which agrees almost exactly with the only prior study of both collision partners [67]. Similarly for the D_1 line, the ratio is 14% higher in the current results, compared with 15% in reference [67]. The primary isotope effect is the higher relative speed of the collision pair, which would predict a 15% increase for ^{3}He due to the reduced mass of the ^{3}He.

The collision induced shift rates are dramatically higher for the D_1 line than the D_2 line. The D_2 line is influenced by two surfaces, with competing binding (see Section 3.4.2), yielding small shifts. The current result for the D_1 line, 4.60 ± 0.12 MHz/Torr and 5.65 ±

0.35 MHz/Torr for ^{4}He and ^{3}He respectively, agree quite favorably with the prior modern results with averages of 4.6 ± 0.2 MHz/Torr and 5.8 ± 0.5 MHz/Torr. The agreement for the D_2 line is similar with the present results of 0.2 ± 0.14 MHz/Torr and 0.65 ± 0.2 MHz/Torr in agreement with the average prior results of 0.38 ± 0.08 MHz/Torr and 0.65 ± 0.04 MHz/Torr. However, the theoretical predictions sometimes disagree even on the sign of the shift.

In Figure 3.7, the spectra are folded about the line center to illustrate the asymmetric nature of the modified Lorentzian line shape. The asymmetry parameter, β_o, is positive, reflecting a higher intensity on the blue side of the line, consistent with equation (2). The asymmetry is somewhat larger for the D_1 line and has the same sign as the shifting rate. The asymmetry rates generally follow the trends observed for the collision induced shifts, as previously reported for Csrare gas collisions [14]. The asymmetry parameters from prior studies reported in Table 3.1 use a different sign convention, where $\beta_o < 0$ implies a repulsive interaction potential [67]. The current and prior observed line shapes for He all exhibit a higher intensity on the blue side of the line.

The primary focus of the current work is to characterize the high pressure line shapes, focusing on the non-Lorentzian features far from line center. In particular, the broader absorption spectrum of Figure 3.4 illustrates the blue satellite of the D_2 line near 735 nm. The location, height and shape of this satellite peak is a strong probe of the interaction potential. To better characterize the full line shape, the absorbance is converted to the cross-section in Figure 3.8. The absorption cross-section, σ, is defined as:

$$\sigma(\lambda) = A/(nL) = \frac{g_u}{g_l}\frac{\lambda^2}{8\pi}A_{ul}g(\lambda) \tag{3.6}$$

where

n = Rb density

L = vapor path length = 8.125 cm

$g_{u,l}$ = degeneracy of the upper and lower levels: $g(^2P_{3/2}) = 4$, $g(^2S_{1/2}) = g(^2P_{1/2}) = 2$
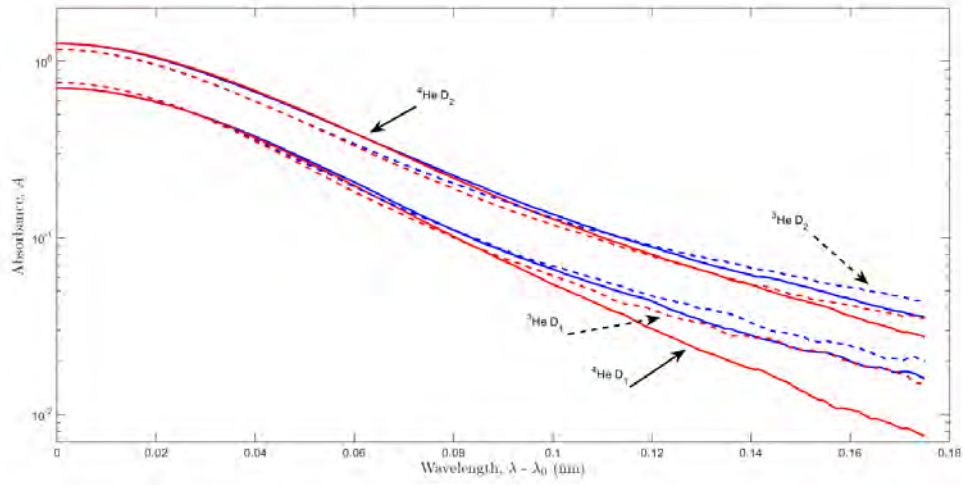
Figure 3.7: Asymmetric line shapes observed at 343 K and 998 Torr for (—) ^4He and (- - -) ^3He. The red wings (—) are less intense than the blue wings (—) of the line shape, yielding a positive value for β_0

A_{ul} = spontaneous emission rate between the upper and lower level:

$$A(^2P_{3/2}) = 3.81x10^7 s^{-1} \text{ and } A(^2P_{1/2}) = 3.61x10^7 s^{-1}$$

$g(\lambda)$ = the wavelength dependent transition line shape

For a Lorentzian line shape with a width of 170 GHz (the D_2 line at 10,000 Torr), the peak cross-section would be $\sigma = 6.9x10^{-14}$ cm^2, about twice the value observed in the spectrum of Figure 3.8 with a peak D_2 cross-section of $3.6x10^{-14}$ cm^2. The Rb density appears to be overestimated by the wall temperature, with $\Delta T = 6K$ sufficient to explain the difference.

The variation in Rb density due to cycling of the temperature control loop produces a periodic variance in the absorbance of Figure 3.4. This variation is removed in Figure 3.8. The temperature varies periodically with a peak-to valley difference of 3 K and a period of 3.5 min. At T= 473 K, the Rb vapor pressure curve exhibits a 12% change in density for the 3 K temperature variation. By ratioing the observed absorbance to the Rb density when calculating the absorption cross-section, this variance is fully removed.

48
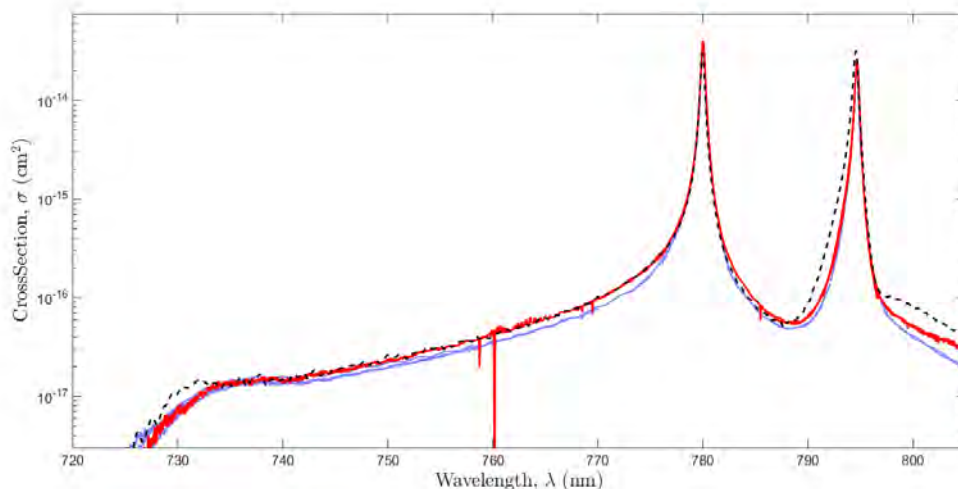
Figure 3.8: Absorption cross-sections at 10,000 Torr observed for: (—) ^{4}He and (—) ^{3}He and (- - -) predicted from the Anderson-Talman theory with dipole moment variation and absorption Boltzmann factor. The spectra are obtained by merging the observed absorbance at T = 333 K near line center to T = 533 K in the far wings. The oxygen absorption and several calibration lamp lines are retained in the ^{3}He spectrum.

The absorption cross section reported in Figure 3.8 is comprised of absorbance spectra for six Rb densities, $n = 2.35 \times 10^9 - 5.36 \times 10^{13} atoms/cm^3$ (T = 333-533 K). By merging the absorbance at low density for the line center and at high density for the blue satellite, a single curve is developed with larger dynamic range. A variation in cross-section of more than 4 orders of magnitude is observed. Note that the shapes of the ^4He and ^3He wing spectra are quite similar. The location of the D_2 blue satellite is 735.7 nm independent of pressure with an amplitude of 0.03% of the peak at T= 100^oC and 10,000 Torr. The location of the blue satellite is predicted by the maximum in the X-B difference potential as discussed below at 728.6 nm. The B barrier in the $B^2\Sigma_{1/2}^+ - X^2\Sigma_{1/2}^+$ difference potential from reference [19] predicts the He blue satellite at 721.5 nm, whereas

49

the surfaces reported in reference [16] predict a maximum at 723.8 nm. The current ab initio surfaces systematically over predicted the barrier height in the $B^2\Sigma^+_{1/2}$ surface.

3.4   Discussion and predicted line shapes

The observed high-pressure line shapes are compared with predictions of the semi-classical Anderson Talman theory in the following discussion. The presentation includes a brief development of the theory, a description of the potential surfaces, and a comparison of the predictions with the current observations.

3.4.1   *Anderson Talman Line shape theory with dipole moment variation.*

In the Anderson Talman theory of pressure broadening, [60] the line shape, $I(v)$, is determined from the Fourier transform of the auto-correlation function, Φ:

$$I(v) \propto Re \int_0^\infty \Phi(s)e^{i2\pi vs}ds \tag{3.7}$$

$$\Phi(s) = e^{-ng(s)} \tag{3.8}$$

where n is the density of the perturber and the accumulated phase difference, g(s), is defined by the difference potential, $\Delta V(r)$, and collision trajectory with impact parameter, b, and relative speed, v. We have recently applied this theory to the Cs D_1 and D_2 lines for collisions with rare gases and the approach is developed in further detail in reference [34]. Recently, Allard et. al. [1] has derived a modified version of the Anderson-Talman equations that incorporates the variation of dipole transition moments, d, with inter-nuclear separation, r. They also include a Boltzmann term that gives the probability distribution for inter-nuclear separation,

$$\bar{d}(r) = d(r)e^{V_X(r)/2kT} \tag{3.9}$$

where V_X is the ground state surface used to describe an absorption profile. With these modifications, the accumulated phase for a single adiabatic surface is:

$$g(s) = \frac{1}{\bar{d}^2(r(0))} \int\limits_0^\infty 2\pi b db \int\limits_\infty^\infty dx \left[\bar{d}^2(r(0)) - Exp\left(\frac{-i}{\hbar} \int\limits_0^s dt \Delta V(r(t)) \right) \bar{d}(r(0))\bar{d}(r(s)) \right]$$

(3.10)

assuming straight line trajectories:

$$r(t) = \sqrt{b^2 + (x + \bar{v}t)^2}$$

(3.11)

Allard et. al. note that including the Boltzmann factor is not consistent with straight line trajectories, but improves agreement with experiment [1]. Equation (10) uses an average velocity, $\bar{v}$, rather than including the Maxwellian speed distribution. With this form of the difference potential, the integral over time, t, in the exponential can be accomplished analytically. The remaining two integrals over x and b are accomplished numerically.

The real and imaginary parts of the accumulated phase

$$g(s) = \alpha + i\beta$$

(3.12)

at large correlation distances, s, become linear:

$$\alpha(s) = \alpha_0 + \alpha_1 s$$

(3.13)

$$\beta(s) = \beta(0) + \beta_1 s$$

(3.14)

yielding the core line shape of Equation (3.2). The wing of the line shape requires the full integral analysis of Equations (3.7-11).

3.4.2   Potential surfaces.

The diatomic potential surfaces that arise for collisions between the rubidium in its ground $^2S_{1/2}$ state or first excited $^2P_{1/2,3/2}$ states, and helium are required to predict the D_1 and D_2 line shapes. The ground $X^2\Sigma^+_{1/2}$ and excited $A^2\Pi_{1/2}$, $A^2\Pi_{3/2}$ and $B^2\Pi^+_{1/2}$ potential energy surfaces have been calculated using one-electron pseudopotential technique and are provided in Figure 3.9.
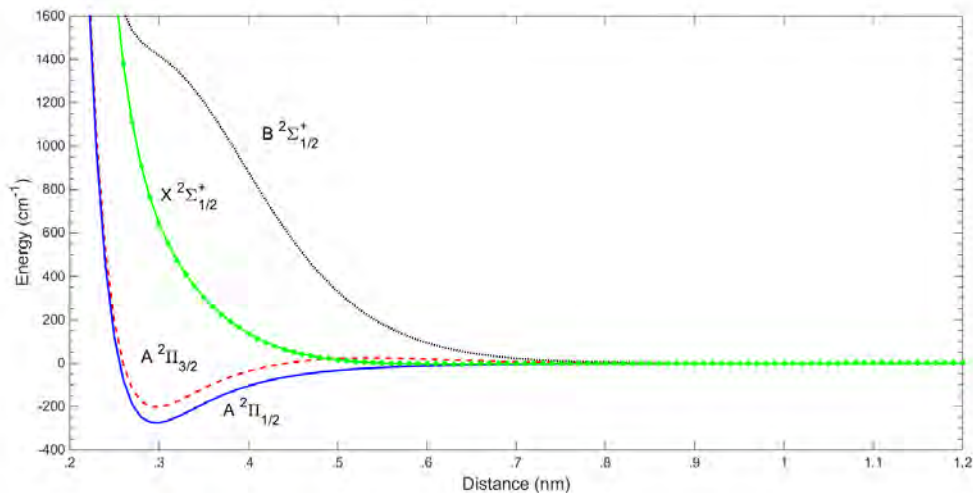
Figure 3.9: Rb-He potential energy surfaces

The calculation method is based on the use of pseudopotentials, which reduces the Rb-He excimer to a one-electron molecular problem. In this model, Rb^+ and He are treated as two closed-shell cores interacting with the alkali valence electron via semi-local pseudopotentials. The total potential energy includes the core-core interaction, the interaction between the Rb valence electron and the ionic system Rb^+-He, and the spin orbit coupling.

The core-core interaction, which corresponds to the Rb^+-He ground state potential energy curve, is taken from the accurate coupled cluster calculations of Hickling et al. [36] Single and double excitations were included, along with a perturbative treatment of the triple excitation terms, CCSD(T). This potential is fit using the analytical form of Tang and Toennies [75]. The equilibrium distance of the neutral dimer is larger than that of the ionic system, and few energies were calculated around this distance. Providing an analytical form for the Rb^+-He core-core interactions increases the accuracy in the region of interest for the neutral Rb-He dimer. The analytical form contains the well-known long range van der Waals terms and an exponential short-range repulsion. By least squares fitting,

the parameters of the analytical form were derived. An excellent agreement is observed between the analytical and the original numerical potential. The difference between the analytical and the numerical potentials for all internuclear distances is $< 3\ cm^{-1}$.

For the interaction between the Rb valence electron and the ionic system, Rb^+-He, we have performed a one-electron ab initio calculation using semi-local pseudopotential for the Rb^+ core and the electron-He effects. The electron-He atom interaction was represented by a pseudopotential fitted in our group. However, the Rb atom has been represented by the one-electron pseudopotential proposed by Barthelat et al. [27] and used in previous calculations [13, 24, 25]. In addition, we take into account the core-valence correlation by applying the operator formulated by Müller et al. [58]. For each atom (Rb or He), the core polarization effects are described by the effective potential proposed by Müller and Meyer. The electric dipole polarizabilities were taken as 9.245 a.u. for the Rb^+ core and 1.3838 a.u. for He [49, 78].

The pseudopotential parameters were optimized in order to reproduce the ionization potentials and the lowest valence s, p and d one-electron states as deduced from the atomic data tables. The Gaussian type orbital basis sets used for the rubidium and helium atoms were 6s/6p/4d and 3s/3p. The calculated ionization potential and the lowest atomic energy levels for Rb were compared with the experimental data [5, 57] and a good agreement was observed. The largest absolute error is 32.43 cm^{-1} obtained for 5s-6p transition energy.

The spin-orbit interaction is evaluated using the semi-empirical scheme of Cohen and Schneider [23]. The spin-orbit coupling for the electronic states, dissociating into 5p, is given by the following matrix:

$$\begin{bmatrix} E_p\left(^2\Pi\right) - 1/2\xi & \xi/\sqrt{2} & 0 \\ \xi/\sqrt{2} & E_p\left(^2\Sigma^+\right) & 0 \\ 0 & 0 & E_p\left(^2\Pi\right) + 1/2\xi \end{bmatrix} \quad (3.15)$$

The diagonalization of such a matrix provides us with the eigenvalues and the energy splitting leading to three molecular states related to the atomic limits $S_{1/2}$, $P_{1/2}$ and $P_{3/2}$. The spin orbit coupling constant ϵ_{5p} (Rb) = 158.396 cm^{-1} was used in the present calculation. The rotation matrix issued from the diagonalization is used to determine the dipole moment including the spin-orbit interaction.

The atomic asymptotic limits in Figure 3.9 have been shifted to E=0 to better compare the surfaces. The ground $X^2\Sigma^+_{1/2}$ surface correlating with Rb 5 $^2S_{1/2}$ is largely repulsive with a very shallow well of depth $\approx$ 4 cm^{-1} at about 0.63 nm. The $A^2\Pi_{1/2}$ surface correlating with Rb 5 $^2P_{1/2}$ has a well of 202.9 cm^{-1} near 0.30 nm. A local maximum of 24.3 cm^{-1} occurs at longer range, near 0.53 nm. The $A^2\Pi_{3/2}$ and $B^2\Sigma^+_{1/2}$ both correlate to Rb 5 $^2P_{3/2}$. The $A^2\Pi_{3/2}$ well is deeper than the $A^2\Pi_{1/2}$ surface , 275 cm^{-1}, but at the same location, 0.30 nm. The $B^2\Sigma^+_{1/2}$ exhibits a long range shallow well of 0.85 cm^{-1} near 1.0 nm. The barrier appears as a broad shoulder near 0.35 nm, with no minimum at shorter range. These well depths differ by those reported in reference [16] by 20-210%.

The corresponding difference potentials are shown in Figure 3.10. There is no long range minimum in the $A^2\Pi_{3/2}$-$X^2\Sigma^+_{1/2}$ difference potential and the minimum for $A^2\Pi_{1/2}$-$X^2\Sigma^+_{1/2}$ is less than 0.2 cm^{-1} suggesting no red satellite features for the D_1 and D_2 lines. The D_1 $A^2\Pi_{1/2}$-$X^2\Sigma^+_{1/2}$ difference potential has a positive extremum of 24.4 cm^{-1} at a separation of 0.57 nm. The $B^2\Sigma^+_{1/2}$-$X^2\Sigma^+_{1/2}$ component of the D_2 transition has a positive extremum of 907.7 cm^{-1} at a separation of 0.34 nm. The variation of dipole moment with nuclear separation and the Boltzmann factors described in equations (9-10) are provided for each surface in Figure 3.11. The dipole moments for the current B-X surface decrease from the asymptotic limit by < 15% at r = 3 nm, with minimal variation for the other transitions. The variation at shorter distances has minimal impact on the line shapes. However, the Boltzmann factors vary by a factor of 2-3 for the X and B states, and will significantly modify the wing line shapes.
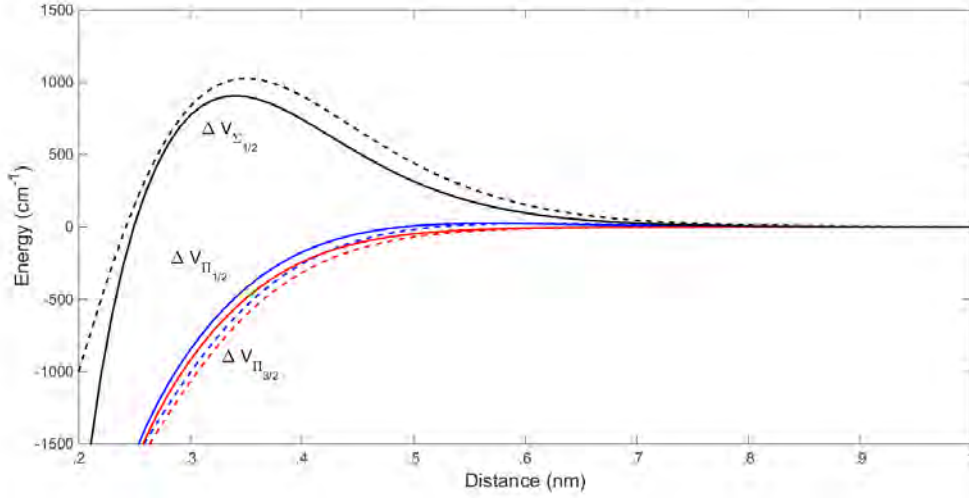
Figure 3.10: Rb-He difference potentials for the current work (—) and (- - -) for the identical potentials used by Blank [16] and Bouhadjar [19].

To compute the D_1 and D_2 spectra we treat each of the difference potentials separately. The D_1 line is separated from the D_2 line in Rb by 237 cm^{-1} and only the $X - A^2\Pi_{1/2}$ difference potential is required to compute the line shape. The D_2 line is more complicated and requires both the $X - A^2\Pi_{3/2}$ and X-B difference potentials. An approximate method to treat this problem for large spin orbit coupling is to compute $g(s)$, for each difference potential and weight them equally to compute the correlation function. This procedure is equivalent to a convolution of the two spectral lines. For ease of computation, we fit the numerical difference potentials to an expansion in $1/r^n$, with n = 6-20.

In our recent work on Cs rare gas line shapes, several empirical modifications of the potential surfaces were required to achieve reasonable agreement with the observed line shapes [34]. No empirical modifications of the potential surfaces are required in the present study.
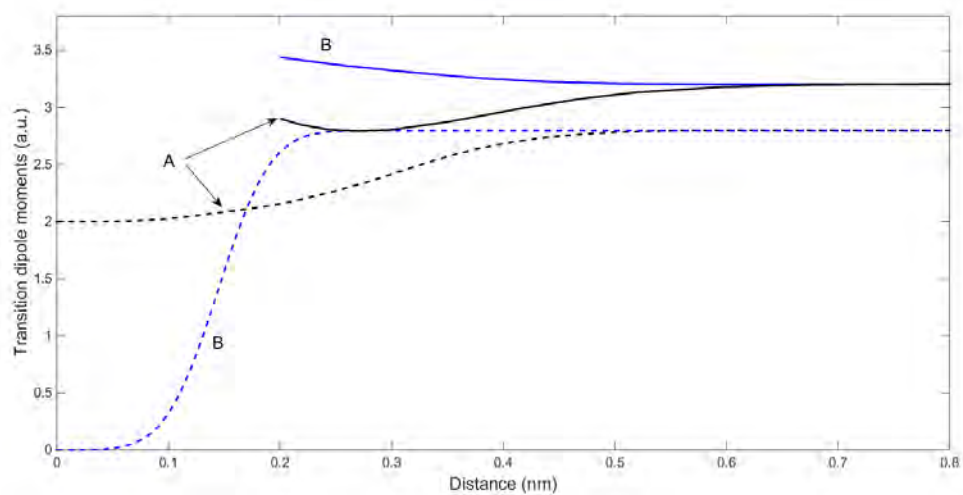
(a)
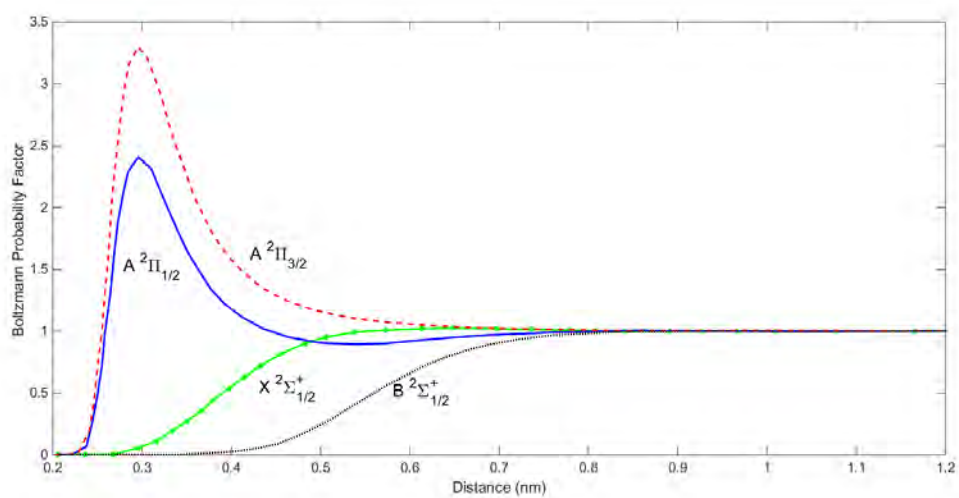
(b)

Figure 3.11: Dipole moment (a) and Boltzmann Factors (b). Hager (- - -) [34] and Bouhadjar (—) [19]. A corresponds to the dipole moment for the $X - A$ transitions with B corresponding to the $X - B$ transition.

56

3.4.3 Comparison of observed and predicted line shapes.

The broadening, shifting and asymmetry parameters as predicted by Equation (3.2) are compared with the present observations in Table 3.1. The calculated broadening rates are systematically larger than the currently observed rates by 1.1-3.2 MHz/Torr and agree within 20%. The ^{3}He broadening rates are higher due to the increased relative velocity. However, the increase is not as high as anticipated and different for the D_1 and D_2 lines due to a line dependent decrease in cross-section with temperature, as discussed below. The collision induced shift rates are generally more sensitive to interaction potential and yet exhibit very good agreement.

There is a significant difference in the shift rates for the D_1 and D_2 lines. This has also been observed in our recent Cs study [34]. The $A^2\Pi_{3/2}$-$X^2\Sigma^+_{1/2}$ difference potential yields red shifts, whereas the long-range barrier in the $B^2\Sigma^+_{1/2}$-$X^2\Sigma^+_{1/2}$ surfaces yields a blue shift. The convolution of these two line shapes yields a smaller blue shift for the He D_2 line. In contrast, the D_1 line involves only the $A^2\Pi_{1/2}$-$X^2\Sigma^+_{1/2}$ surface which exhibits a modest barrier and thus a larger blue shift. The magnitude of the predicted shift rate is about twice the measured value for the D_1 line, but close to the small value observed for the D_2 line. The predicted shifts rates are remarkably similar to the observations, except for the ^{3}He D_2 line. Indeed, the predictions for the ^{3}He D_2 line suggest a near zero shift, whereas the observations indicate an increased shift to the blue. The temperature dependence of the cross-section for the D_2 shift appears to be a most sensitive probe of the interaction potential, and is discussed further below. The predicted asymmetry parameters are correlated with the shift rates.

Several predictions of the high pressure D_1 and D_2 line shapes for Rb-^{4}He and ^{3}He collision pairs, at 10,000 Torr and T = 333 K near line center and T = 533 K in the far wings, are provided in Figure 3.12. Each spectrum consisting of 105 digitized points was

computed numerically from the Fourier transform of the correlation functions for the D_1 and the convolved D_2 difference potentials.

The blue satellite predicted for the D_2 line is readily apparent and located at 735.7 nm, consistent with the observations of Figure 3.4. This secondary maximum in the D_2 far blue wing occurs at a wavelength corresponding to the barrier height in the $B-X$ difference potential. The barrier of 907.7 cm^{-1} reported in Figure 3.10 leads to the observed shift of 52 nm. The extremum in the difference potential is broader and occurs at shorter range for Rb than the corresponding surfaces for Cs. This is consistent with the stronger, more defined blue satellite in Cs [34]. Inclusion of the variation in dipole moment and corresponding Boltzmann factors in equations (9-10) further flattens and reduces the magnitude of the peak of the blue satellite. The variation in dipole moment has a minor effect on the amplitude of the blue satellite. The effect of the Boltzmann factor in absorption (using the ground state potential) is more significant and produces a blue satellite with a poorly defined peak and agrees well with the current observations. A Boltzmann factor based on the B state surface, as suggested for emission [1], dramatically reduces the intensity of the far wing, inconsistent with the observed line shape.

The D_1 line shown in Figure 3.12 exhibits a red shoulder, which may result from the tail of a strong, but unresolved, blue feature that is blended with the core. The barrier heights for the $A^2\Pi_{1/2}$-$X^2\Sigma_{1/2}^+$ transitions are considerably less, leading to smaller shifts and larger amplitudes. The D_1 blue satellite is about $0.5x10^{-3}$ of the resonant peak, or ≈ 5 times larger than the D_2 blue satellite. The blue D_1 satellite does not present a spectral peak, but rather generates a shoulder on the core line shape.

A full prediction of the Rb-^{4}He line shape for both lines is directly compared with the experimental results in Figure 3.8. The potentials of Figure 3.9 do not require empirical modification to provide excellent quantitative agreement. The dipole moment variation and absorption Boltzmann factor is critical to obtaining strong agreement. The difference in the
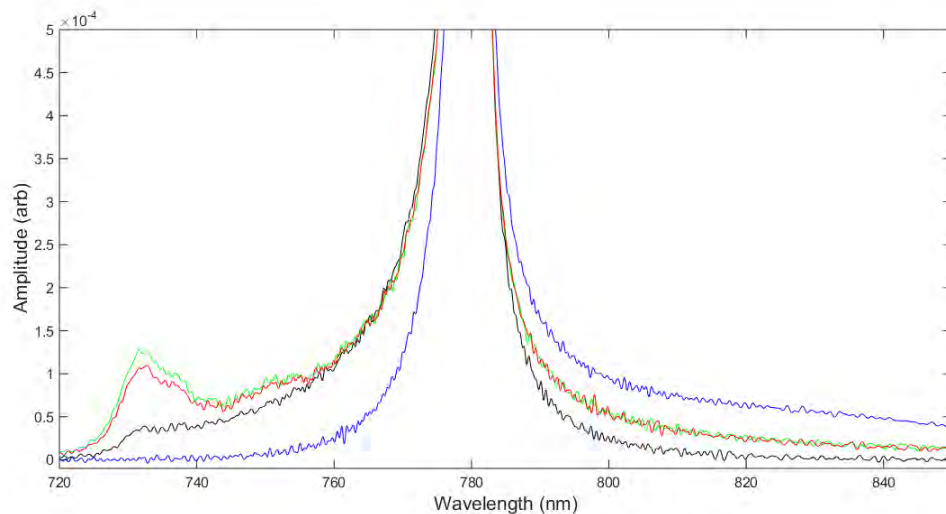
(a)
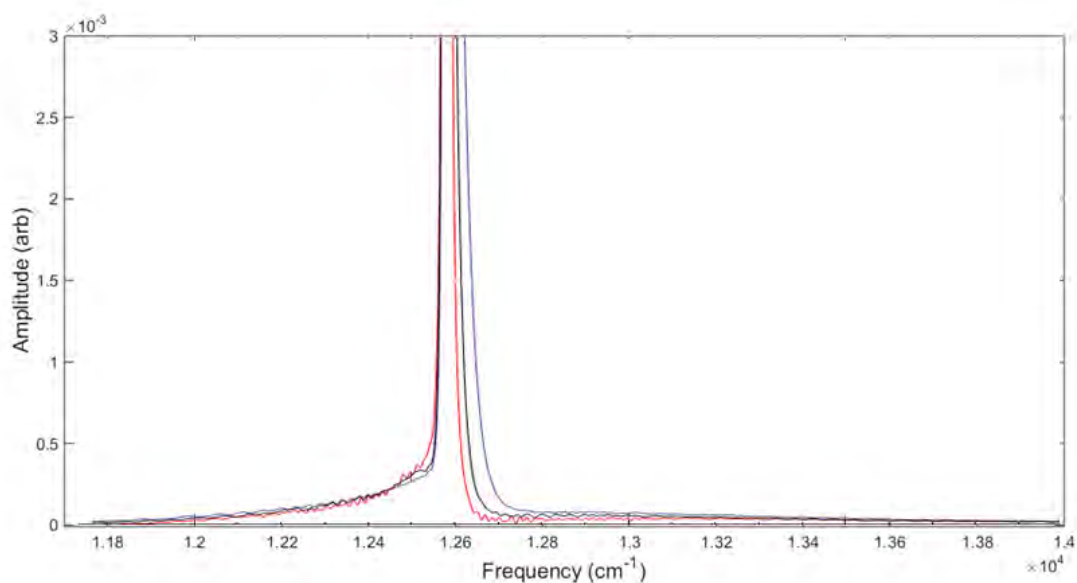
(b)

Figure 3.12: Predicted ^{4}He line shapes at 10,000 Torr and 333K: (a) Rb D_2 line with convolution of both surfaces, assuming from top to bottom (—) no dipole moment variation, (—) dipole moment variation with no Boltzmann factor, (—) dipole moment variation with ground state Boltzmann factor, and (—) dipole moment variation with excited B state Boltzmann factor; (b) Rb D_1 line with (—) unmodified potentials, (—) difference potential scaled by 0.5, and (—) difference potential scaled by 2.0.

59
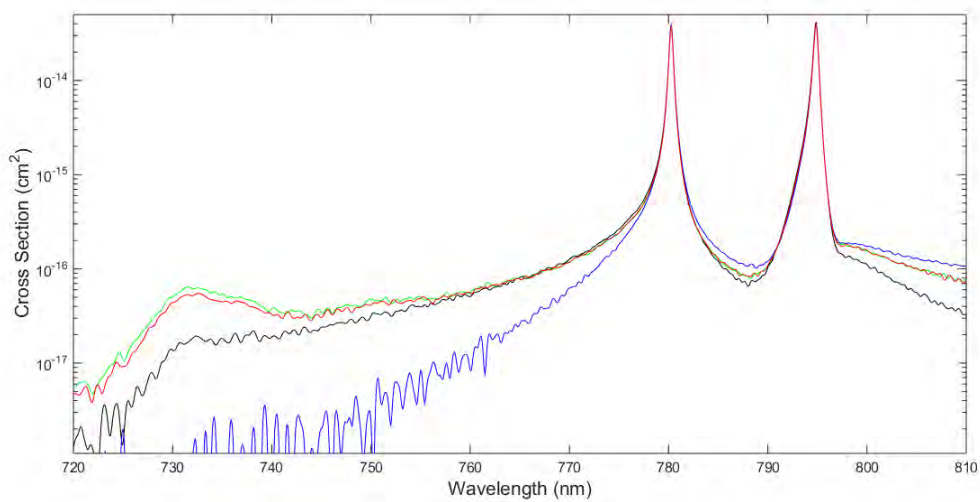
(a)
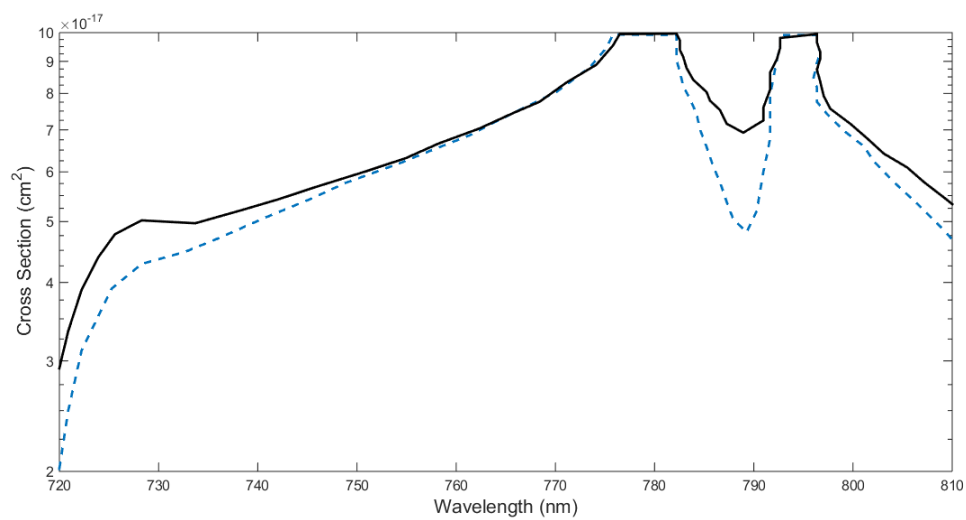
(b)

Figure 3.13: (a) Predicted full scan of absorption cross-section on logarithmic scale, and (b) absorption cross-section from Bouhadjar [19] at 320 K (- - -) and 500 K (—).

60

modeled and predicted D_1 line is the greatest. The experimental observations for the ^{3}He and ^{4}He collision partners also exhibit a greater difference on the red side of the D_1 line, presumably reflecting greater temperature dependence.

3.4.4 Predictions of the temperature dependent broadening and shifting rates.

A prediction for the temperature dependence of the broadening and shifting rates is provided in Figure 9. The rates are converted to cross-sections:

$$\sigma_b = \gamma \left(\frac{kT}{\bar{v}} \right) \tag{3.16}$$

$$\sigma_s = \delta \left(\frac{kT}{\bar{v}} \right) \tag{3.17}$$

to remove the influence of relative velocity on the results. Two sets of predictions are provided for each case. Using the average velocity as expressed in Equation 3.10 allows for highly sampled temperature dependence. However, non-physical oscillations are observed, particularly for the D_2 line. By employing a Maxwellian distribution of relative speeds the oscillations are removed, but the temperature dependence is less sampled, due to the increased numerical complexity.

Often, broadening cross-sections are assumed independent of temperature, as predicted for a hard sphere interaction. Alternatively, the broadening cross-section for a long range attractive, r^{-6}, interaction, yields a $T^{-0.3}$ dependence [37, 83]. The D_2 broadening cross-section is nearly independent of temperature, whereas the D_1 line is closer to the predicted van der Waals potential, presumably due to the single, isolated surface. Note that the shallower well observed for the Rb-He system compared with Cs-Ar with higher polarizability, [34] produces a smaller temperature dependence. The ^{3}He collision partner is a reasonable substitute for higher temperature conditions, as the potential surfaces are unchanged. The observed ^{3}He broadening rate does not increase as much as predicted by the mass effect on average velocity. This difference is greater for the D_1 line, consistent with the predicted stronger temperature dependence of the cross-section. The predicted

61
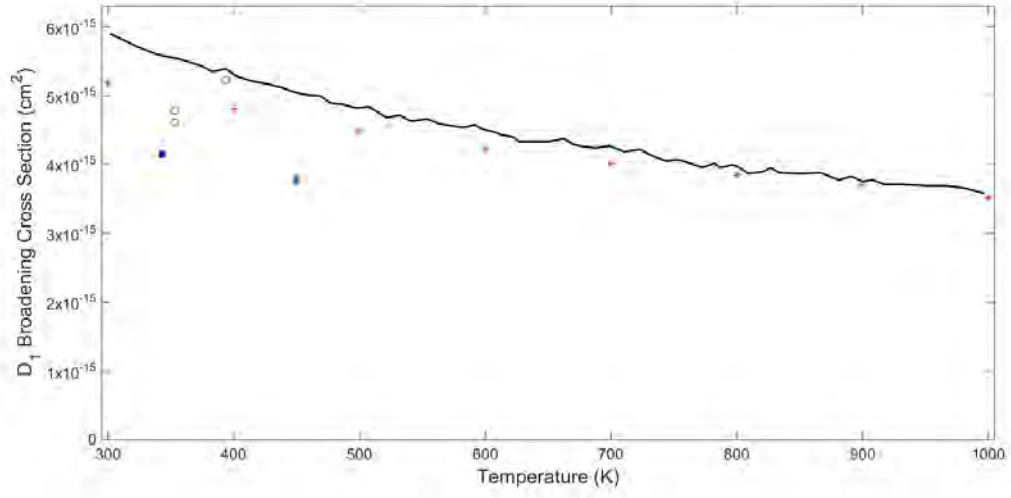
(a)
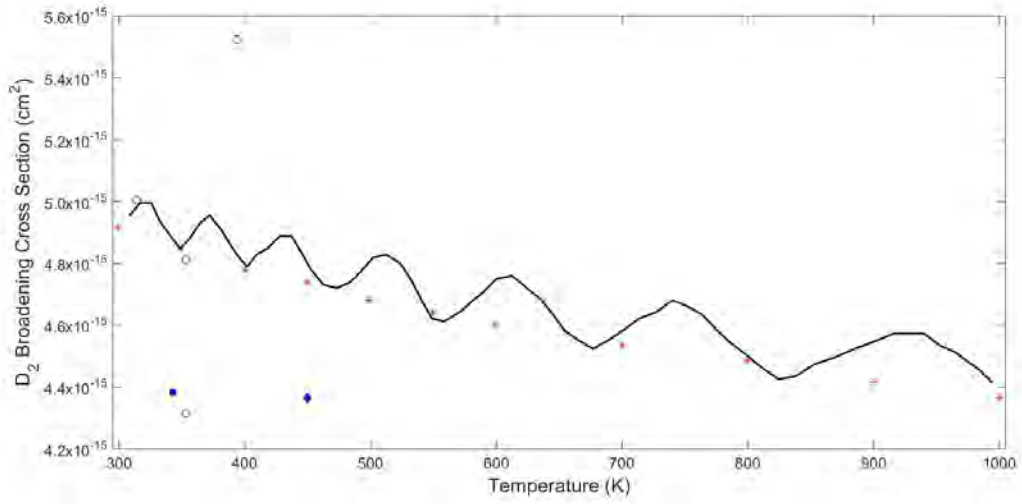
(b)

Figure 3.14: Predicted temperature dependence for the broadening cross-sections for the Rb-^{4}He D_1 and D_2 lines using: (——) average velocity and ($*$) full Maxwellian speed distribution. Experimental observations for: ($\square$) ^{4}He, ($\diamond$) ^3He with mass change reflected as temperature increase, and ($\circ$) prior observations from references [65, 67, 68, 83].

(a)

(b)

Figure 3.15: Predicted temperature dependence for the shifting cross-sections for the Rb-^{4}He D_1 and D_2 lines using: (—) average velocity and ($*$) full Maxwellian speed distribution. Experimental observations for: ($\square$) ^{4}He, ($\diamond$) ^{3}He with mass change reflected as temperature increase, and ($\circ$) prior observations from references [65, 67, 68, 83].

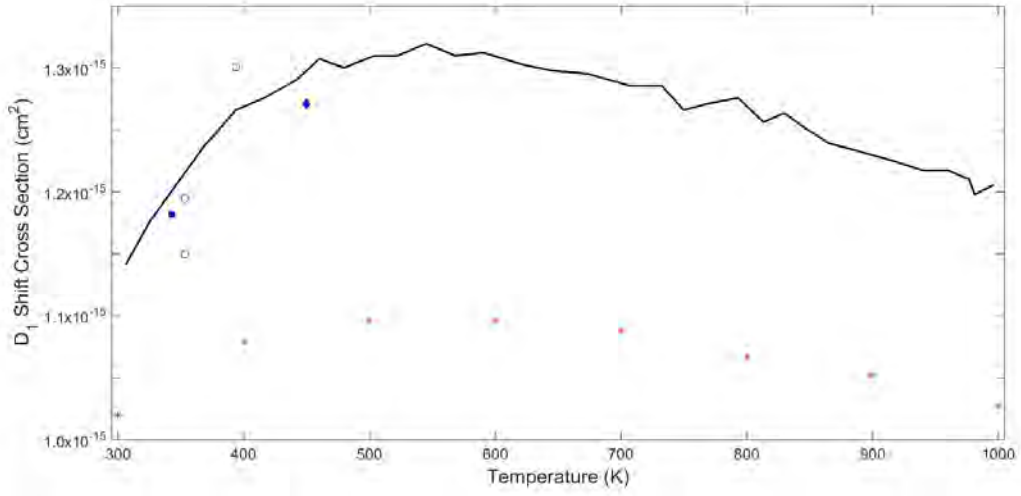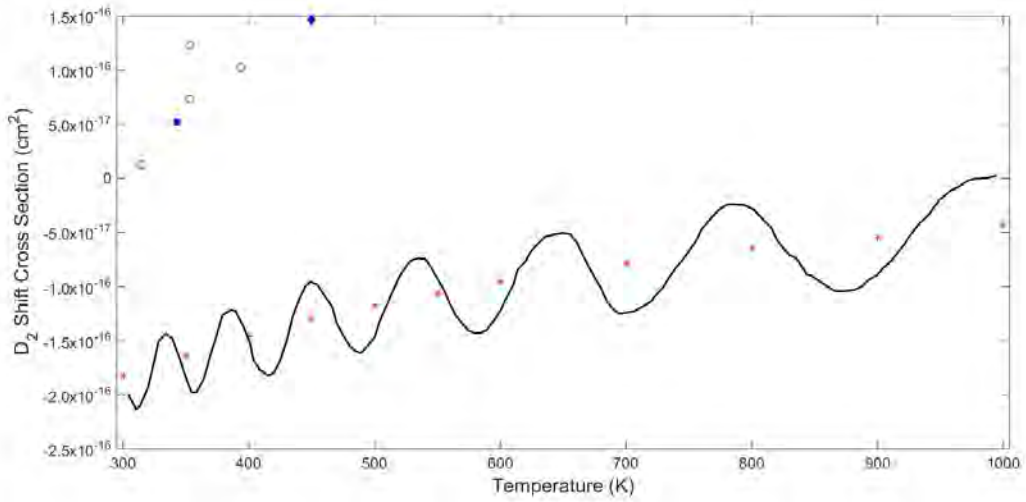isotope effect on the D_2 shift rate is less supported by the data. At high temperatures the predicted shift rate trends toward zero, whereas the observed rate increases to the blue. The shift rate is more sensitive to the interaction potential and the weighting of the two surfaces. A detailed experimental study of the temperature dependence requires the development of an alkali vapor cell where the temperature can be increased without modifying the alkali vapor density. In the current apparatus, temperature controls the Rb vapor pressure and the line center quickly becomes opaque at T > 373 K.

The cross-sections for collision-induced shifts depend critically on the interaction potentials. For the rather large blue shift associated with the D_1 line, the shift cross-section is predicted to depend only weakly on temperature. However the small shift predicted for the convolved D_2 line approaches zero at high temperature.

Given the experimental fidelity available in experimentally observed line shifts from laser absorption experiments of about 1% error, an experimental test of the current predictions is warranted, but requires independent control of Rb vapor density and gas temperature. Unfortunately, the available experimental results span a small range of temperatures and have been measured with different techniques.

3.5   Conclusions

The experimentally observed, non-Lorentzian line shapes for the Rb D_1 and D_2 lines broadened by ^{4}He and ^{3}He at pressures up to 20 atmospheres ($\approx$15,000 Torr) are in strong quantitative agreement with the predictions of the Anderson-Talman theory using one electron pseudo potentials. The predictions of the line core broadening agree with the observations to within 14%. The agreement for shifting rates is better, 10%, except for the ^{3}He D_2 line which is near zero. The significant difference in the observed shift rates for the D_1 and D_2 lines is explained by the convolution of the red shifted line shape from $A^2\Pi_{3/2} - X^2\Sigma_{1/2}^+$ difference potential with the blue shifted line shape of the $B^2\Sigma_{1/2}^+ - X^2\Sigma_{1/2}^+$ surface. The asymmetry parameters predictions are less accurate, with more than a factor

of two disagreements with observations. To match the location, amplitude and shape of the blue wing of the D_2 line requires the inclusion of dipole moment variation and Boltzmann factor. The difference in the modeled and observed wings of the D_1 line is larger, including a significant difference for ^{3}He and ^{4}He collision, suggesting a more sensitive dependence on temperature. The current prediction for the temperature dependence of the line shape parameters awaits an experimental verification at low Rb density.

IV. Temperature Dependent Broadening and Shifting

4.1 Introduction

The diode pumped alkali laser (DPAL) was first proposed in 2001 as an alternative to high-power, diode-pumped, solid-state lasers [46, 48]. A high power, >1 kW, system with 48% optical-to-optical efficiency has recently been reported [18], and development for laser weapons applications [62] is in progress. The radiation from un-phased diode bars is absorbed by an alkali metal vapor (Potassium, Rubidium, or Cesium) on the D_2 line, $^2S_{1/2} \rightleftarrows {}^2P_{3/2}$, collisional relaxation populates the lower fine structure split $^2P_{1/2}$ state, and lasing is achieved on the $^2P_{1/2} \rightleftarrows {}^2S_{1/2}$ transition. The alkali metal vapor is pressure broadened by a rare gas, usually helium, to efficiently absorb the emission from spectrally narrowed diode bars or stacks. The concept of using a gas phase medium for the phasing of large diode arrays combines the best features of electrically driven lasers with the inherent thermal management advantages of a gas lasers. Indeed, the primary factor for DPAL laser weapon development is the promise of improved beam quality over diode pumped solid-state lasers.

In the DPAL system, the cycle rate for pump, collisional fine structure mixing and lasing can be very high, < 0.1 ns, particularly for pump intensities exceeding 10 kW/cm^2 [56]. The initial linear response of output power to input power is degraded at high pump intensity when the system becomes bottlenecked on the fine structure transition [33]. The transition to this bleached limit depends critically on the D_2 absorption line shape relative to the spectral width of the diode pump [35]. Thus, the most important kinetic parameters are the rates for fine structure mixing and line broadening. Spatial variations in diode pump intensity and flow of the gas through the resonator will lead to turbulence and gain medium index variations, reducing beam quality. Rapid fluctuations in the gain

66

medium can not be corrected by adaptive optics and will ultimately limit device beam quality.

The temperature dependence of the mixing and broadening rates is critical to modeling the DPAL performance. Unfortunately, the rates for line broadening and shifting are only available for the Rb-He DPAL system over a limited temperature range, T = 310-450 K [12, 69]. The numbers with the greatest confidence have an even more limited temperature range, T = 314-394 K [65, 67, 68, 83]. Furthermore, theoretical predictions vary widely, with disagreements on even the sign of the shift rate [12, 53]. In the present work we report the temperature dependence of the Rb D_2 and D_1 line broadening and shifting rates for ^{4}He for T = 373-723 K. To achieve this broad temperature range, control of the alkali vapor density independent of the gas temperature is required.

The line shape parameters are a sensitive probe of the interaction potentials [34]. By placing the current results in context of prior theoretical predictions, we explore the sensitivity of line shapes to the potential surfaces. The larger objective is to empirically inform potential surfaces to predict both the temperature dependence of the line broadening and fine structure mixing rates, unifying the Rb-He DPAL kinetics.

4.2 Experiment

The experimental setup for the laser absorption spectroscopy experiment is shown schematically in Figure 4.1. A Coherent Verdi 18 pumped continuous wave (CW) Spectra Physics Matisse Ti-Sapphire ring cavity laser, with bandwidth 10 MHz, was tuned over approximately 32.5 GHz centered on the $5^2S_{1/2} \rightarrow 6^2P_{1/2}$ (D_1, λ_1 = 795 nm) and 23 GHz centered $5^2S_{1/2} \rightarrow 6^2P_{3/2}$ (D_2, λ_2 = 780 nm) transitions. The beam was amplitude modulated at 360 Hz then directed through the alkali cell with a small portion of the beam split off into a vacuum sealed Triad Technologies Pyrex 25 mm x 50 mm cell filled with ^{87}Rb to be used as an absolute wavelength reference. Polarization of the laser beam was oriented horizontally with a typical initial output power of 600-800 mW. Various filters

and optics reduced the power delivered to the test cell to approximately 94 nW at its maximum with a beam radius of 2 mm giving a beam intensity of approximately 2.8 mW/cm^2. The calculated saturation intensity, I_{sat}, is approximately 1.6 mW/cm^2 at vacuum and 1.2 mW/cm^2 at pressure.

Three Hamamatsu S2281-04 silicon photodiodes with Hamamatsu C9329 pre-amplifiers connected to Stanford Research Systems SR850 DSP lock-in amplifiers were used to collect the incident, transmitted, and reference absorption signals. The integration time for the lock-in amplifiers was set at 100 ms giving 10 data points per second. The alkali containment cell was specially designed for this experiment to allow for low alkali number densities while opperating at a range of increased cell temperatures ranging from 373 K to 723 K. Further discussion of the alkali containment cell can be seen in Section 4.2.1. Helium (^{4}He), 99.999% purity, was added and removed from the system via gas/vacuum handling system after going through a SAES MC1-902F gas getter providing 99.9999% purity. Pressure was monitored using a MKS model 609A manometer with a 670 signal conditioner for pressures up to 500 Torr. An Agilent model FRG-700 manometer with a XGS-600 signal conditioner was used to measure vacuum pressures down to an ultimate vacuum pressure of 3.9 microtorr. When the turbo pump was off, the leak rate was < .5 mTorr/min.

Laser wavelength information was collected using a fiber coupled High-Finesse WSU-2 wavemeter using the reflection off of a pellicle placed at the exit aperture of the Matisse laser. The wavemeter, used in conjunction with the ^{87}Rb reference cell, created the wavelength axis for the data. Day to day variations in the absolute frequency reported by the wavemeter relative to the Rb reference cell were on the order of 10-20 MHz, with variations during the day of 1-2 MHz. These variations are caused by the sensitivity of the wavemeter to changes in temperature and humidity within the laboratory. The day to day
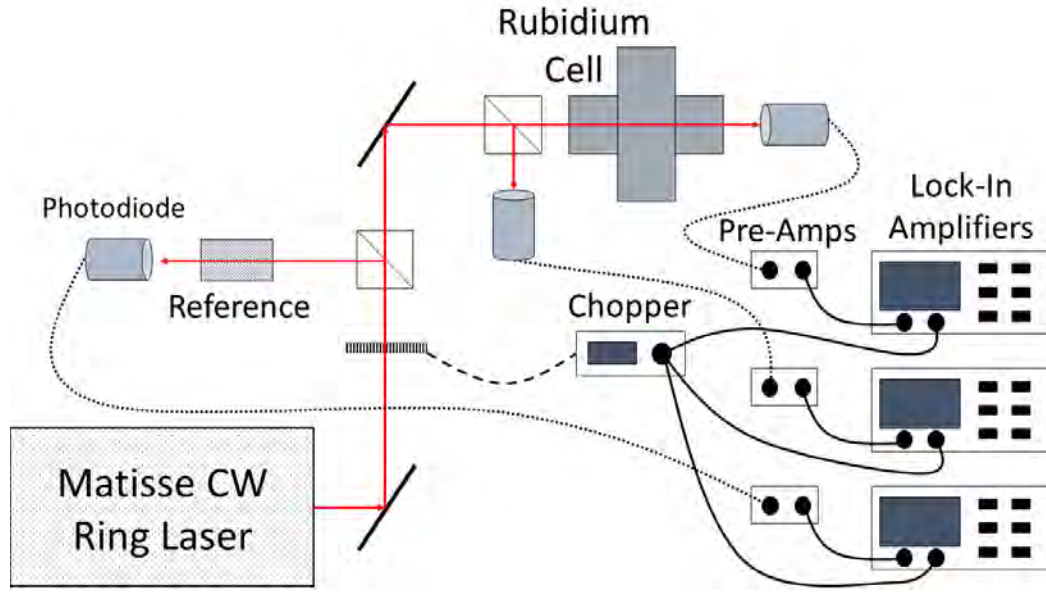
Figure 4.1: Setup for the temperature dependent shift and broadening rates experiment

variations are on the order of the baseline variations discussed later, with the run to run variations during the day being much smaller.

4.2.1   Alkali Cell.

A new alkali containment cell was required for the completion of this experiment. The typical sealed cell or heat pipe configurations [38] keep the alkali pool at the temperature of the cell thereby controlling the number density based off the vapor pressure curves [73, 74]. This leads to an exponential increase in alkali number density as experimental temperature increases. A high alkali number density creates the problem of the sample appearing completely opaque to the probing laser during the absorption experiment. A balance must be struck between having enough alkali density to give a good signal to noise ratio while still being low enough not to be opaque to the probe laser. The cell, shown in Figure 4.2, avoids this high alkali number density problem by being a true two temperature system. The alkali, located in the alkali pool portion of the cell, is kept at a separate, lower temperature than the rest of the cell. This temperature, separate from the experimental temperature,

drives the alkali number density. The rest of the cell can then be raised to the required temperature for the experiment without affecting the alkali number density driven by the lower temperature alkali pool. Typical values for the number density of alkali inside the cell before closing the valve were approximately $10^{11} - 10^{12}$ cm^{-3}.
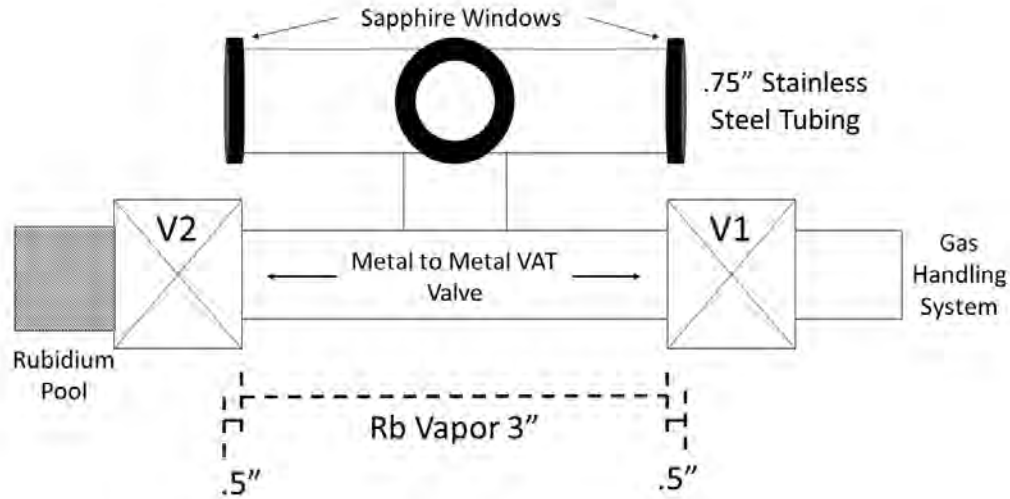
Figure 4.2: Alkali containment cell. This cell design allows for a two temperature system where the alkali density is controlled independently from the experimental temperature.

A VAT Series 541 metal-to-metal angle valve allows for the alkali pool to be closed off from the rest of the cell preventing fluctuations in the number density during an experiment. The cell also uses another metal to metal valve to attach to a gas handling system that allows for the addition or removal of buffer gas. The entire cell can be sealed off from the gas handling and vacuum system in order to keep the number density of the buffer gas constant.

The body of the alkali containment cell is of stainless steel construction with welded seams on the upper 5-way cross and the lower T sections. The 5 way cross sits on top of the T section as shown in Figure 4.2 with the metal to metal valves located at either end of

the T section. Connections between the various pieces, and holding the windows in place, are Conflat (CF) 1 1/3" knife edge connections with silver coated copper gaskets. Silver plated bolts and plate nuts are used in conjunction with the CF connections. Two wedged sapphire windows are used in the upper cross along the beam path with a non-wedged flat sapphire window and a flat cap being used on the cross connections parallel to the beam path. The port with the non-wedged window is used to monitor alkali buildup inside the cell. The capped port opposite the non-wedged window is not used during this experiment.

Heating of the cell is accomplished through the use of three sections of BriskHeat thermal tape. One section of type BlH1010 heater tape is wrapped around the alkali pool with temperature monitoring accomplished using Type J thermocouple attached to a Watlow Model 96 proportional integral derivative (PID) temperature controller. The rest of the cell is heated using two lengths of BWH1010 high temperature thermal tape, capable of temperatures up to 1000 K. The first piece is wrapped around the two metal to metal valves and the T connection, with the second length covering the upper 5 way cross. Type K thermocouples were placed at the junction of the T connection and the 5 way cross as well at the top of the 5 way cross. The two high temperature sections are connected to Watlow EZ-Zone PID temperature controllers. Each section of thermal tape has its own independent power and controller. The thermal tape and thermocouples are then wrapped with ThermoTec exhaust insulating wrap with foil wrapped aero-gel blanket insulation outside of that. The maximum temperature of the apparatus was limited by the braze around the windows, which fails around 823 K. The experiment limited the temperature to 723 K in order to not reach the failure point and destroy the cell.

4.2.2 Procedure.

Cell preparation begins by baking the cell at the highest temperature the experiment will be operated at, up to 723 K, while using a turbo pump to vacuum the cell out down to 3 to 4 μTorr. This removes anything that may be stuck on the wall and passivates the

system at those higher temperatures. Once the bake-out is completed the cell is returned to the starting temperature of 373 K, and the cell is isolated from the vacuum system by closing valve 1. Valve 2, leading to the alkali pool, is opened allowing alkali vapor to diffuse throughout the cell. During the diffusion process, the CW laser scans continuously across the transition being investigated allowing for a continuous check on the amount of alkali vapor inside the cell during the filling process. It was determined that the opportune time to close valve 2, and stop the flow of any more Rb into the cell, was just before the strongest transition features turned opaque to the probe laser. This allows for the transition to broaden and drop in peak absorbance as the He buffer gas is added and at the same time leave the highest possible absorbance features.

Immediately following the closing of the alkali pool, valve 1 is opened reconnecting the cell to the gas handling system. Helium gas is slowly added to the cell at a rate of approximately 1-2 Torr per second up to the desired pressure and allowed to come to thermal equilibrium for 15 minutes. Once the gas has come to a thermal equilibrium the pressure is recorded using the MKS Baratron Manometer. The cell is once again sealed from the gas handling system by closing valve 1. Once sealed, with both the Rb vapor and the He gas, the cell will not be reopened for the remainder of the current experimental run thereby creating a system with a constant number density of alkali and gas perturbers. Spectral scans across the transition of interest are taken at each cell temperature. Temperatures are increased after each scan while the cell is sealed; each new temperature takes approximately 10 minutes to reach the next set point and is then given 15 minutes to thermally equalize at the new temperature. Upon completion of the run, the temperature is slowly lowered back down to 373 K to avoid thermal gradients within the system that may damage the connections. Finally the cell is opened to vacuum to remove the Rb-He mixture to reset the cell for another run. After each run the cell must be rebaked and vacuumed to remove anything that may have been reintroduced into the system.

4.3 Spectral Analysis

4.3.1 Observed and Simulated Absorption Spectra.

Absorbtion spectra, as shown in Figure 4.3, for the D_1 and D_2 transitions and the reference were created using Beer's Law,

$$I_t = I_0 \, e^{-\sigma n l} \tag{4.1}$$

$$A = -ln\left(\frac{I_t}{I_o}\right) = \sigma n l \tag{4.2}$$

where σ is the absorption cross-section, n is the number density, and l is the path length through the cell. The I_t and I_0 signals for the absorbance equations were made to be approximately equal to each other while traveling through the cell with no alkali inside. The two signals were not exactly equal which shows up as an offset of the entire line shape, as seen in Figure 4.5. There is also a slight signal variation between the two detectors as a function of wavelength which shows up as a cyclical wave feature as a function of wavelength. This wave feature is well approximated using a low, 3rd order, polynomial. The offset shown in Figure 4.5 is approximately A = 0.2 corresponding with the modulation on the order of ΔA = 0.01.

The data in Figure 4.3 shows an increase in the absorbance as the temperature increases. This may be caused by a small amount of alkali metal being deposited somewhere in the cell, increasing the number density as the temperature increases. This does not cause a problem as long as the data does not become opaque to the probing beam. Other data sets show a decrease in the absorbance signal as temperature goes up. The scans where the absorbance decreases suggests that no alkali metal gets deposited on the wall during the filling process. The decrease results from out-gassing from the cell walls which reacts with and removes some of the alkali vapor. Either an increasing or decreasing absorbance signal is usable, as long as the signal does not drop too low for a good signal to noise ratio and does not become opaque to the probing beam. Correctly filling the cell with enough alkali that it does not deposit on the walls, while at the same time adding enough

so that the signal is not eaten up by other impurities in the gas is a delicate balancing act requiring much trial and error.
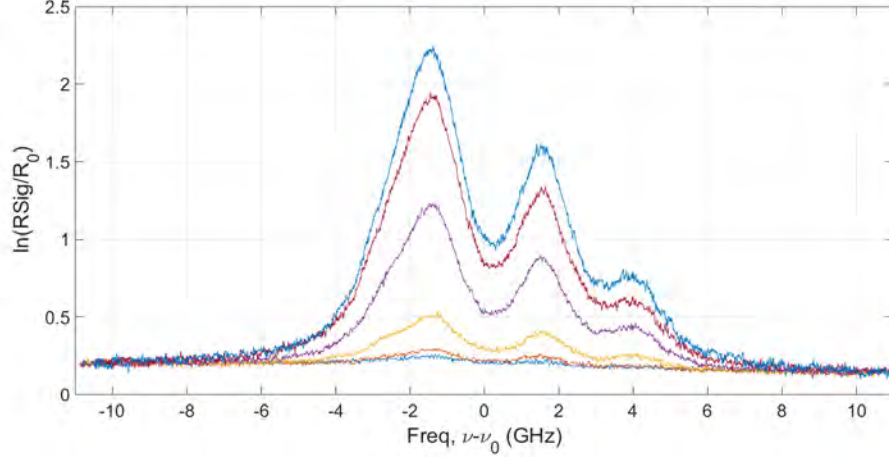
Figure 4.3: Absorption spectra of the Rb D_2 (ν_0 = 384.23 THz) transition. These spectra were taken with the cell filled to 75 Torr of He at 373 K and then sealed. Temperatures shown from top to bottom are 698 K, 648 K, 498 K, 448 K, 398 K, and 373 K.

To model the absorption spectra and extract line shape parameters, the hyperfine transition lines, 4 for D_1 and 6 for D_2 transitions, were predicted for both the [87]Rb and [85]Rb isotopes. For the low pressure reference cell, only the [87]Rb isotope is present. The predicted line shape for a single isotope is provided in equation 4.3. When fitting the predicted line shape to the observed spectra, the relative frequencies and line strengths were constrained using the values given by Steck [73, 74]. The fit was given a global shift allowing the locked transitions to shift as a group to create the best fit to the reference data and refine the absolute laser frequency. A low order polynomial baseline is included to account for detector response as discussed earlier. This global shift is the absolute wavelength error present in the wavemeter being used on that day for that run, typically on the order of between 60-80 MHz. This global shift is also applied to the high pressure

74

absorption spectra to improve the accuracy of the observed collision induced shifts. A built-in MATLAB non-linear least-squares fitting routine, lsqcurvefit, was used to fit the series of Voigt profiles and polynomial baseline to the data.

$$Abs = \sum_{i=1}^{n}(A)(S_i)V(v_i - \delta, \gamma_D, \gamma_L) + \text{cubic} \tag{4.3}$$

In Equation 4.3 the summation over the hyperfine lines has a shared global amplitude (A) which accounts for overall rubidium density within the cell. Each hyperfine line then has its predetermined relative amplitude (S_i) multiplied by overall Voigt line shape. The Voigt line shape is a convolution of the Gaussian and Lorentzian line shapes and has parameters v_0 for line center, γ_D for the doppler broadening on the Gaussian, and γ_L for the pressure broadening on the Lorentzian. The parameters γ_D, γ_L, A, and δ are shared among all of the hyperfine line Voigts. The pressure shift, δ, and pressure broadening, γ_L, are pulled from these fits. The values used for center frequency and relative amplitudes are shown in Tables 4.1 and 4.2.

$$V(v, \gamma_D, \gamma_L) = \int_{-\infty}^{\infty} G(v, \gamma_D)L(v - v_0, \gamma_L) \tag{4.4}$$

$$G(v_0, \gamma_D) = \frac{e^{-v^2/(2\gamma_D^2)}}{\gamma_D \sqrt{2\pi}} \tag{4.5}$$

$$L(v - v_0) = \frac{1}{\pi}\frac{1/2\gamma_L}{(v - v_0)^2 + (\gamma_L)^2} \tag{4.6}$$

A fit of equation 4.3 including both isotopes for a typical high pressure absorption spectrum is provided in Figures 4.5-4.6.

This baseline subtraction was the largest systematic source of error for the fits by producing fitting errors in the absolute frequency axis of up to 8 MHz. Due to the correlation of baseline and Lorentzian width, the uncertainty in width associated with different baseline assumptions is somewhat larger, up to 30 MHz. In order to fully characterize the error associated with various baselines, a set of various polynomials of order 1 through 10 were fit to the same data set and the associated shift and broadening

Table 4.1: D_1 Hyperfine Transitions [73, 74]

Transition$_{F_l \rightarrow F_u}$		Center Frequency (cm^{-1})	Line Strength (S)
^{85}Rb	T$_{22}$	12579.000	.2857
	T$_{23}$	12579.012	1
	T$_{32}$	12578.899	1
	T$_{33}$	12578.911	.7999
^{87}Rb	T$_{11}$	12579.076	.0752
	T$_{12}$	12579.104	.3762
	T$_{21}$	12578.848	.3762
	T$_{22}$	12578.876	.3762

Table 4.2: D_2 Hyperfine Transitions [73, 74]

Transition$_{F_l \rightarrow F_u}$		Center Frequency (cm^{-1})	Line Strength (S)
^{85}Rb	T$_{21}$	12816.601	.8258
	T$_{22}$	12816.603	1.071
	T$_{23}$	12816.605	.8564
	T$_{32}$	12816.502	.3059
	T$_{33}$	12816.504	1.071
	T$_{34}$	12816.508	2.478
^{87}Rb	T$_{10}$	12816.682	.1611
	T$_{11}$	12816.684	.4027
	T$_{12}$	12816.689	.4027
	T$_{21}$	12816.456	.0805
	T$_{22}$	12816.461	.4027
	T$_{23}$	12816.470	1.127
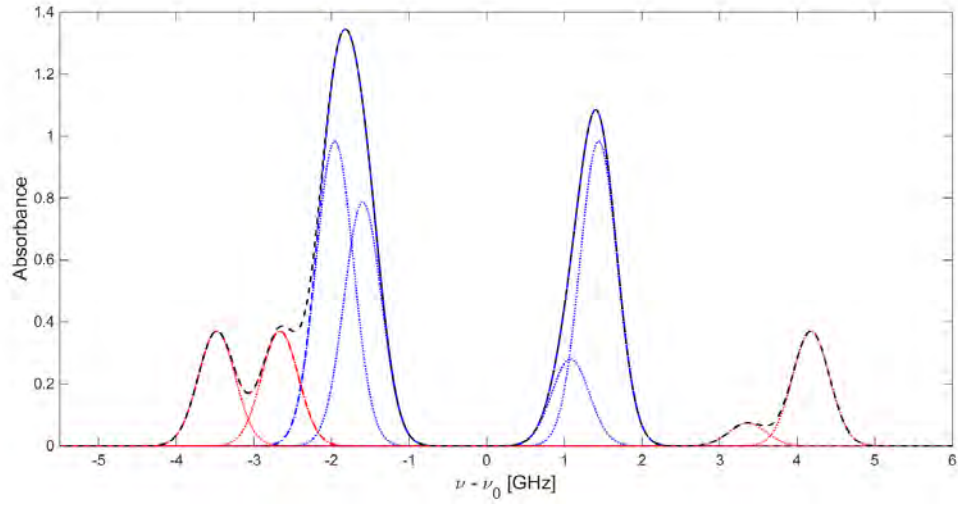
(a)
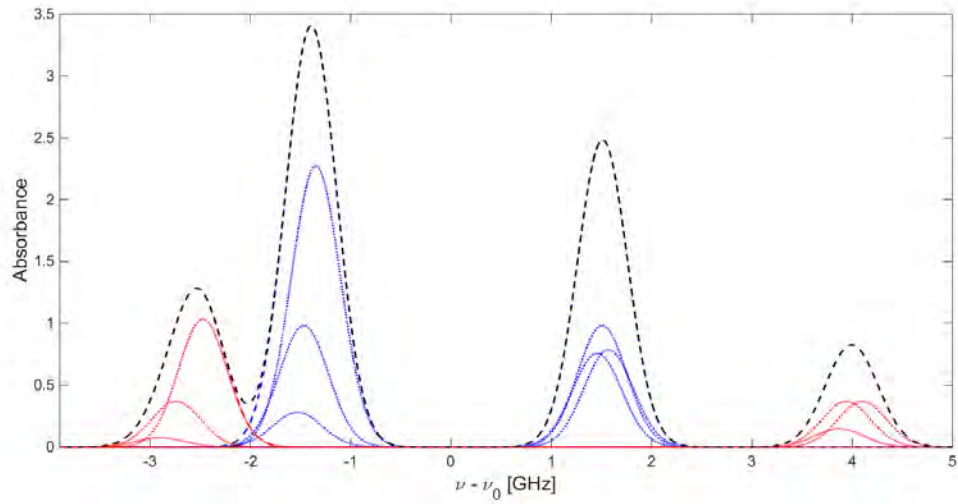
(b)

Figure 4.4: Simulated D_1 (ν =794.978 nm) and D_2 (ν =780.241 nm) non-broadened hyperfine lines at 373 K. The blue dotted lines represent the ^{85}Rb hyperfine lines and the red dotted lines represent the ^{87}Rb hyperfine lines. A total combined line shape is shown as the black dashed line.

error analyzed. This procedure was repeated for every temperature at each separate buffer gas fill pressure. The resulting global shift with associated error is taken as the overall shift of the spectra from vacuum. A fit of the hyperfine lines to a single run with residuals can be seen in Figures. 4.5 and 4.6.
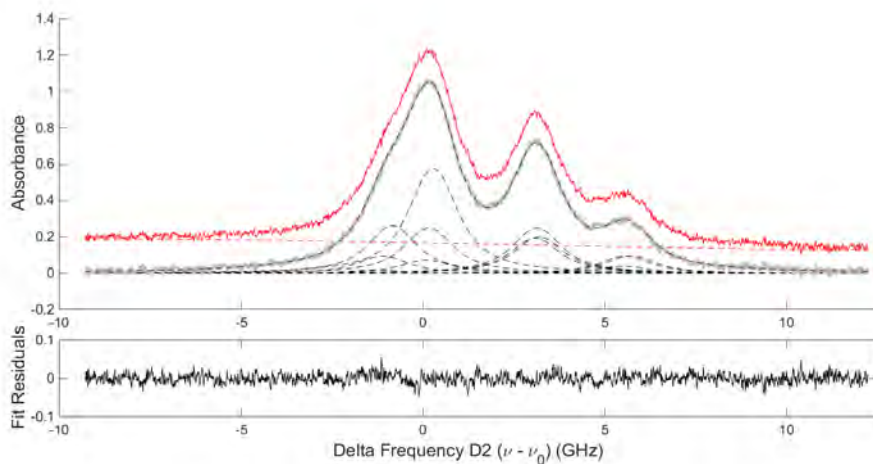
Figure 4.5: D_2 transition filled with 74.9 Torr of He at 498 K with fit. The red line is the raw data with the dashed red line below being the baseline. The fit is shown as a dashed black line over the gray data with the hyperfine lines being shown as smaller black dashed lines. The residual to the fit of Equation 4.3 can be seen in the sub panel.

During the fitting shown in Figure 4.5, the Doppler portion of the broadening was fixed to the set temperature of the system plus or minus one degree. This was done due to the baseline problems discussed earlier creating a trade off between the Doppler and Lorentzian line widths. By locking the Doppler width to its known value, the trade-off between the two widths was removed when adding a baseline. During the fitting of the reference cell, the Doppler width was approximately 580-590 MHz. At the set temperature of the reference cell, 313 K, the expected width is 530 MHz. The measured width was wider indicating that
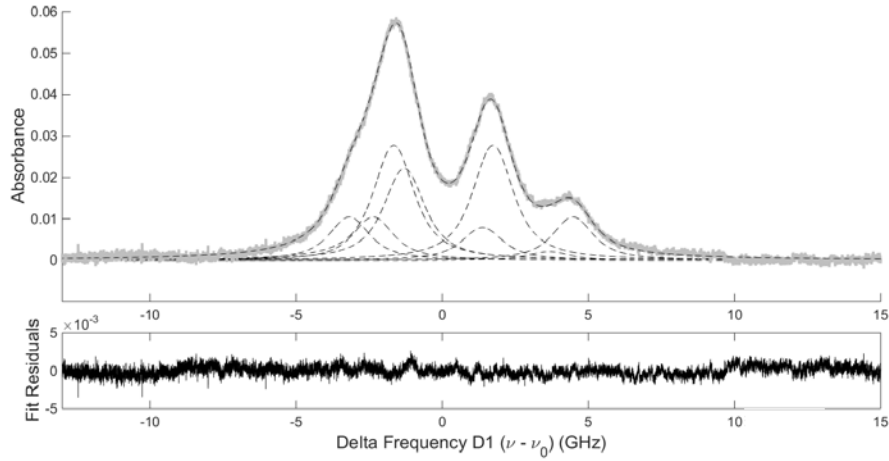
Figure 4.6: D_1 transition filled with 72.9 Torr of He at 548 K with fit. The fit is shown as a dashed black line over the gray data with the hyperfine lines being shown as smaller black dashed lines. The residual to the fit can be seen in the sub panel.

the intensity of the laser through the reference cell was many times over I_{sat}. This did not affect the line centers of the fits that are used as the wavelength correction.

With the completion of the fitting, it becomes evident that there are no problems in the experimental setup related to either the polarization of the laser or the transition saturation. A polarization problem within the experiment would manifest itself as saturating the more intense transitions more than the weaker hyperfine lines. By locking in the relative amplitudes of each of the lines and not having to modify those relative intensities to create a non-structured residual, it is shown that polarization is not a problem. The saturation intensity would show up as a much broader transition than expected due to the saturation broadening present when pumping a transition well above the saturation intensity. Once again our numbers, when compared with previous results and approximated pump intensity, support that saturation broadening was not an issue during the experiment.

79

4.3.2 Comparison of observed and predicted line shape parameters.

The shift and broadening rates as a function of temperature are sensitive measures of both the choice of theory and the potential energy surfaces used by those calculations. Prior theoretical predictions employ two techniques: the Anderson-Talman semi-classical approach used by Blank [14] and the full quantum approach with Baranger coupling used by Loper [53]. There is also a comparison to be made of two predictions that use the same level theory, Anderson-Talman, but have two different potential energy surfaces. The potential energy surfaces developed by Blank [14] are ab initio calculations with no dipole modification, while the surfaces used by Hager [34] are psudo-potential surfaces provided by Berriche et al. [13].
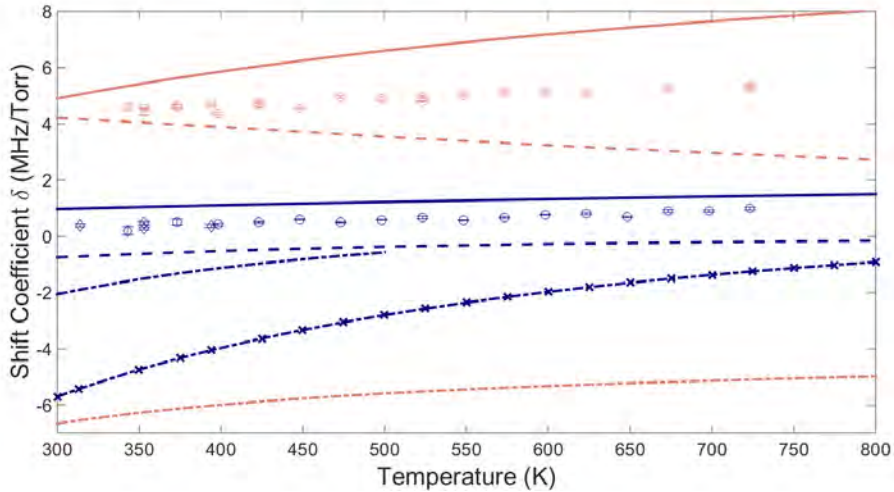

Figure 4.7: Temperature dependence of the Rb-He shift coefficient. Figure shows D_1 in red and D_2 in blue. The current experimental data is shown as circles with other reported literature as squares (diamonds) for $D_1(D_2)$. Theoretical calculations from Blank(—), Hager(- - -), and Loper(–.–) are also shown. For the D_2 transition Loper has both Baranger and Allard(–.x) coupling.

The current experimental results are compared with the prior theoretical predictions in Figures 4.7-4.11. The measured shift as a function of temperature in the experiment shows a small, but measurable change in the reported shift coefficient at the higher temperature ranges. The shift coefficients range from 4.36 MHz/Torr to 5.35 MHz/Torr for the D_1 line and from 0.42 MHz/Torr to 0.99 MHz/Torr for the D_2 line over the Δ T = 350 K range. A check on these results is done by comparing the lower temperature measurements to reported results in literature at similar temperatures, which are shown in Figures 4.7 as square markers for the D_1 and diamond for the D_2 transitions. The rates reported by [65, 67, 68, 83] compare well with measured values from this experiment in the 300-400 K temperature range. The shift coefficient, demonstrated by the Rb-He system, shows that the D_1 transition has a shift that is approximately 10 times larger than the shift exhibited by the D_2 transition. The variation for the D_1 line is also on the order of 1 MHz/Torr compared to the total range of the D_2 line being closer to 0.5 MHz/Torr over the temperature range.

The results provided by Loper for the shift coefficient predict a negative (red) shift for the center wavelength of both the D_1 and D_2 transitions. This result is of the opposite sign as that of Blank's shifts and Hager's D_1 shift coefficient, the data from this experiment, and the results from various published results [67, 68, 83]. The magnitude of the theoretical values from Loper also have much greater variation over the temperature range in question than either this data set or other predictions.

The predicted shifts from Blank are in closer agreement with this experiment and literature compared to those from Loper. While Blank's predictions tend to overestimate the shift for both the D_1 and D_2 transitions, they have the correct sign for the shift, as well as following the magnitude of the shifts closely. The potential energy surfaces used by both Blank and Loper were the same, with the only difference being the level of theory used for each calculation. In this case, the semi-classical approach with the ab initio potentials shows a much greater agreement with data.

81

The last theoretical prediction for the shift coefficient comes from Hager et al [34]. Hager's prediction employ Anderson-Talman theory, just like Blank's predictions, while using a pseudo interaction potential. A modified pseudo-potential created by Berrichi [13], using data to inform portions of the potential, is used. While this potential does create a better fit to the high pressure data from Chapter 3.4, it does not predict the temperature dependence of the shift and broadening well. The shift predicted by Hager has wrong sign for the direction of the D_2 shift, but does predict the correct sign for the D_1 transition. The trend as temperature increases shows a decrease in the amplitude of the shift as well.

An attempt is made to tie the predicted shifts and their differences back to their respective difference potentials. A closer look at the two potentials used, the ab. initio from Blank and the pseudo-potential from Berriche, can be seen in Figures 4.8 and 4.9. Starting with the ground state potentials and the kinetic energy of the rubidium we can explore what regions of the interaction potential were probed. Using our temperatures of 300 K to 800 K the energy of the incoming perturber ranges from 208.5 cm^{-1} to 556 cm^{-1}. These energies compared to the ground state potential show that for Blank the interaction distance being probed is 0.41 nm down to 0.34 nm and for Hager's predictions 0.37 nm to 0.31 nm.

For the D_1 line these interaction ranges are all in the attractive portion of the potential difference curve for both Blank's and Hager's predictions. An attractive potential leads to a red shift and as the temperature increases and the difference potential is probed more and more the integrated value becomes less repulsive. The integrated area is still repulsive leading to the blue shift, but is becoming less so. The prediction from Hager is probing a portion of the difference potential that is much more attractive than the region being probed by Blank. The region being probed here starts in the attractive region and as temperature increases will probe smaller inter-atomic distances that are even more attractive. This leads to Hager's predictions becoming less and less blue shifted as temperature increases.
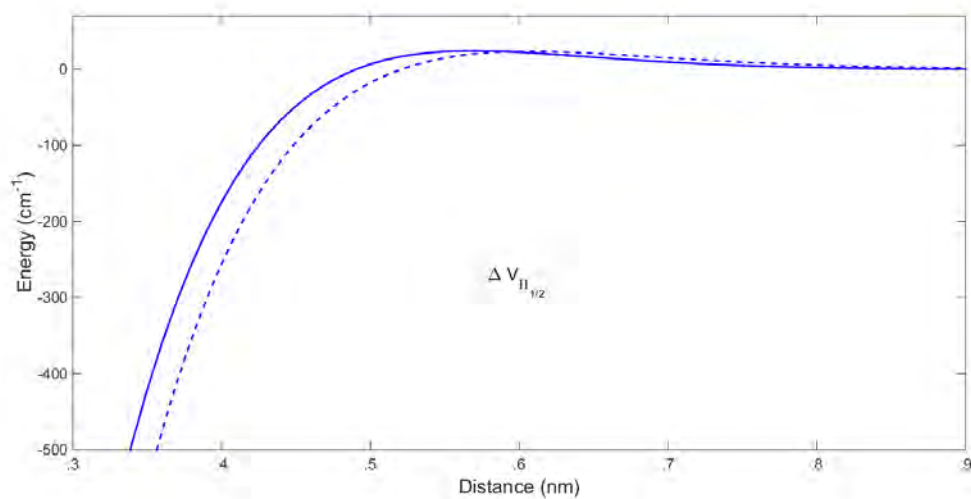
(a)
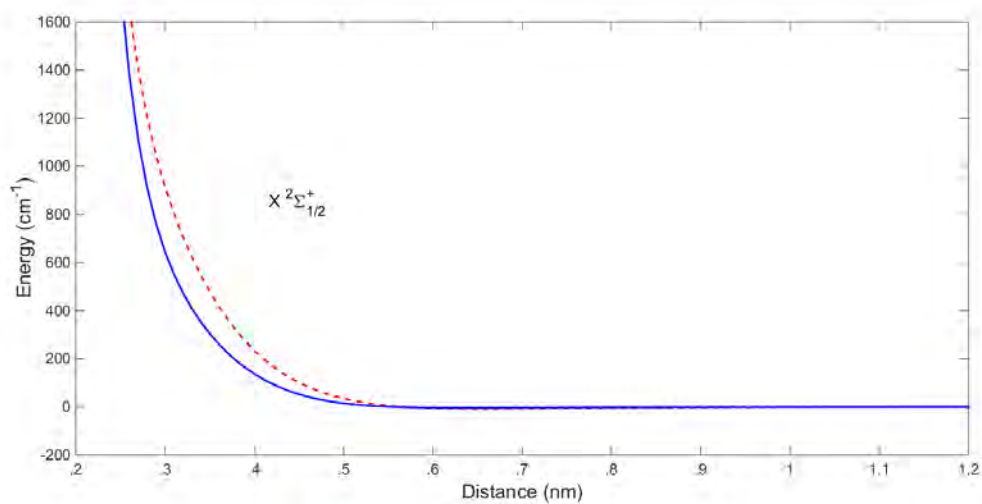
(b)

Figure 4.8: (a) Potential energy differences for the D_1 transition with (b) ground state potential surface. Blank's surfaces (- - -) and Hager's surfaces (—)

A similar analysis of the potential differences is made for the D_2 transition. The analysis is complicated by the multiple surface that make up the shift, but a similar trend can be seen. Using the same interaction regions being probed as the D_1 line Hager's
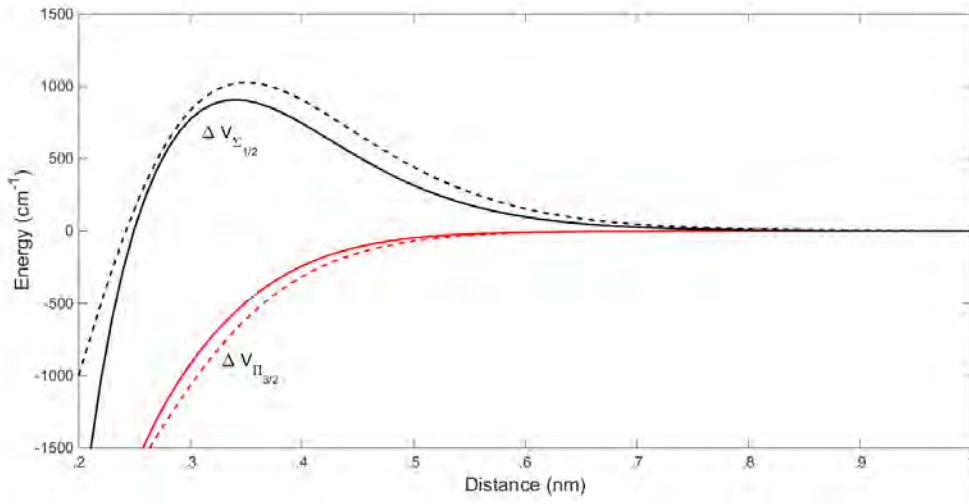
(a)
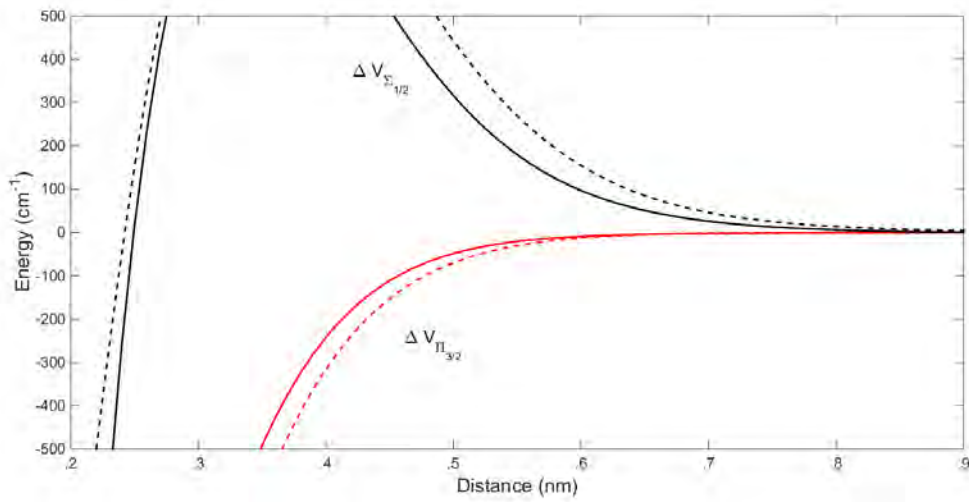
(b)

Figure 4.9: Potential energy surfaces for D_2 transition. Blank's [15] surfaces are shown as (- - -) with Berriche's [13] surfaces used by Hager [34] shown as (—).

potentials show that as the temperature increases the difference potentials grow slightly more repulsive which correlates to his predictions of a slightly increasing blue shift for the D_2 line as temperature increases. The same regions on Blank's difference potentials show

almost no change. There is an extremely small repulsive component visible that does grow as temperature increases. This once again leads to a slight increase in the blue shift as a function of temperature. For both the D_1 and D_2 lines the experimental data appears to split the difference between Blank's and Hager's predictions.

Figure 4.10: Temperature dependence of the Rb-He broadening coefficient for the D_1 line. The current experimental data is shown as red circles with the other reported literature shown as squares. Theoretical calculations from Blank(—), Hager(- - -), and Loper(–·–) are also shown.

The broadening coefficients for the D_1 and D_2 transitions are shown in Figures 4.10 and 4.11 respectively. The experimental data for both transitions once again agree well with literature at the lower temperatures. A few data points representing the same temperatures can be seen. The spread in this values comes from a systematic error of day to day variations in the laboratory. The D_2 transition also shows a data point that varies greatly from the rest of the run. This data point was determined to have a system failure during the testing, it is still shown to indicate measurements were taken at that temperature. The broadening coefficient increases slightly with temperature for both lines, as would be expected by just
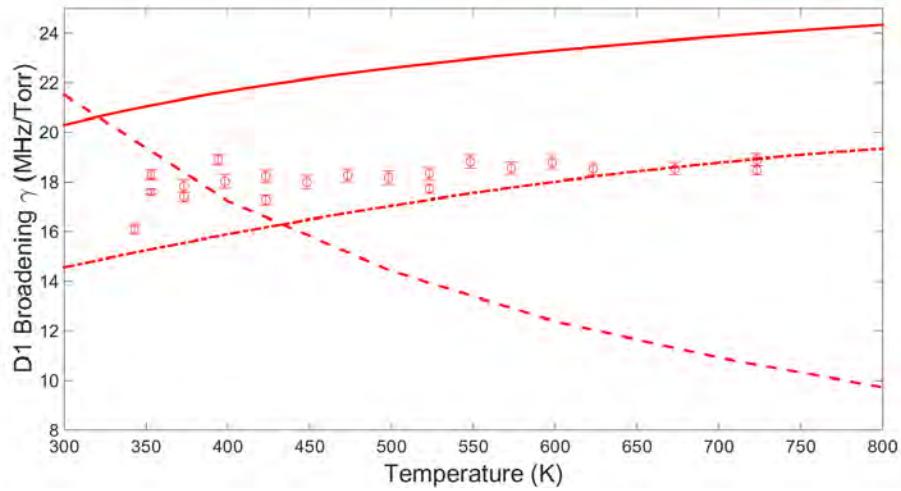
85
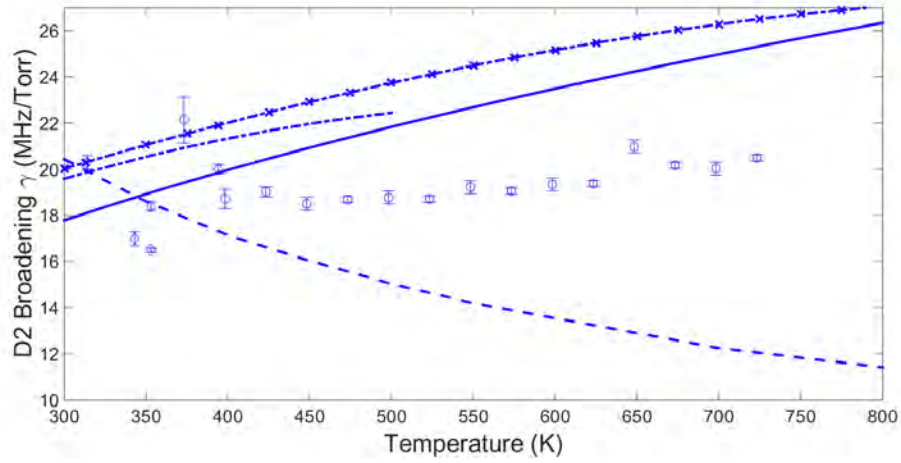
Figure 4.11: Temperature dependence of the Rb-He broadening coefficient for the D_2 line. The current experimental data is shown as blue circles with the other reported literature as diamonds. Theoretical calculations from Blank(—), Hager(- - -), Loper-Barringer coupling(–·–), and Loper-Allard coupling(·x) are also shown.

the simple view of the rate being given as:

$$\gamma(T) = \sigma(T)\bar{v} \tag{4.7}$$

where $\bar{v}$ is the thermally averaged velocity. The current experiment gives a broadening coefficient for the D_1 line that varies from 17.8 MHz/Torr to 18.9 MHz/Torr and for the D_2 line from 18.5 MHz/Torr to 20.5 MHz/Torr as temperature increases from 373 K to 723 K. While the previously reported values and the current experimental values agree well, the theoretical predictions once again do not show good agreement. The same theoretical predictions used for the shift are once again compared here for the broadening. In the case of the broadening for the D_1 line, the predictions made by Blank and Loper both trend in the positive direction. Only the magnitude of the broadening is off, with Loper's predictions being lower yet closer in magnitude to the experimental data, and Blank's predictions being larger and further away in magnitude. The prediction from Hager has

86

a much higher variation in magnitude than seen in either of the other two predictions or the variation seen within the data. Hager's predictions also show a trend that has the broadening becoming less with temperature. This decreasing broadening does not match the data or other predictions.

The D_2 broadening coefficient shows similar trends to the D_1 data. The theoretical predictions for Blank and Loper follow closely with each other with both overestimating the broadening coefficient as a function of temperature. Once again the predictions by Hager show a decrease in the broadening, but have about the same amount of variation as the other two theoretical curves over the temperature range.

4.4   Conclusions

A new experimental technique was developed to observe the shifting and broadening coefficients at high temperatures. Using the new cell and procedures, the Rb-He shift and broadening coefficients were observed for temperatures ranging from 373 K to 423 K, hundreds of degrees higher than the previously reported values of 394 K [68] and 450 K [69]. The experiment shows that while there is a measurable change in the shift and broadening coefficients as a function of temperature that those changes are small. These small changes in shift and broadening rate could be important though in the modeling and building of a DPAL. An analysis of the temperature distribution within a DPAL done by Zhu et. al [87] demonstrates that even at moderate pump powers, 40 W, that the difference in temperature between the center pumped area and the walls can be 300 K or greater.

A comparison of the data with previously measured values show a very good agreement at the lower temperatures. The values agree for both the shift and the broadening coefficients giving a high level of confidence in the current values. These values, along with the previously reported values, were compared to three different theoretical calculations. Two theoretical values were obtained using the same potential energy surfaces, but different theories [15, 53]. The third theoretical value used a different potential, but the same theory

as Blank. None of the theories are in good agreement with the experimental data, or with each other. More work is necessary with the theories and the potential energy surfaces they used to match the experimental data.

V.   Rb-He Temperature Dependent Spin-Orbit Rates

5.1   Introduction

The operation of the DPAL requires a mixing between the two upper excited states in order to achieve lasing. Due to the lack of optical transitions allowed between the levels a different method is required to move population. That method is spin-orbit mixing due to added buffer gas that collisionaly relaxes or excites the Rb between the excited states. The speed at which population is moved from the pumped $^2P_{3/2}$ state to the upper lasing $^2P_{1/2}$ state much be sufficiently high in order to avoid bottlenecking the system. The rate at which the population moves is called the spin-orbit (SO) mixing or spin-orbit relaxation rate. Studies done by Miller [56] and Hurd [38] demonstrated intensity scaling of the DPAL systems where MW/cm^2 pump intensities were achieved exciting more population into the upper level than could be moved down with the SO rate present. This bottlenecked the system leading to lower efficiencies. It was determined that at modest buffer gas pressures the medium could only process approximately 50 photons/atom in a 2-8 ns time frame.

The spin-orbit mixing rate has been previously measured and reported in the literature. Early work by Krause [45] and Beahn [9] give the rates as 1.03×10^{-17} cm^2 at 340 K and 1.2×10^{-17} cm^2 at 373 K respectively. The temperature dependence of the SO rates has been explored as well. Gallagher [28] in 1966 looked at the temperature dependence of the rates over a large temperature range, 300-900 K, but had large 15-25% errors. A more recent study done by Sell [29] improved on the accuracy of these measurements, but only covered a temperature range of about 303-423 K. Theoretical calculations of the predicted SO rates have also been explored by Lewis [51].

Typical measurements of SO rates use either the CW or pulsed methods described in the Background chapter. The benefits of each are a higher averaged power for the CW method and a directly measured time basis for the pulsed. This experiment explores a

hybrid method, dubbed quasi-CW, that is pulsed at such a rate that there are both CW and pulsed features within the data. An exploration of this method has shown it to not be advantageous as this time.

5.2 Experiment

The experimental setup for the side fluorescence measurements used in this experiment are shown in Fig 5.1 below. A new, one of a kind, 200 pico-second 80 MHz rep rate Titanium-Sapphire Spectra Physics Tsunami, optically pumped with a Spectra Physics Millennia eV, was used to excited the Rb along both the D_1 and D_2 lines. The short 200 pico-second pulse used here allows for a mathematical simplification during pulse analysis compared to a more standard 8 ns pulse because it can be modeled as an impulse function compared to the 20-30 ns decay where as the longer pulse can not. Energy per pulse is approximately 3 nJ with a spectral width of 1.5 GHz and a spot size radius of 2 mm. Average output power is approximately 2.5 W with an intensity per pulse between 750 and 1000 W/cm^2, well above the saturation intensity of the system. Rough tuning gives control over output wavelength in 1.5 cm^{-1} range using a birefringent filter with fine wavelength control coming from an electronically controlled Gires-Tournois Interferometer (GTI). Laser wavelength was stable to within 0.01 wavenumbers with a drift of 0.1 wavenumbers over a period of about an hour.

A ConOptics model 360-80 electro-optic modulator driven with a Model 25D driver was placed into the beam path. The electro-optic modulator uses a non-linear potassium dihydrogen phosphate (KD*P) crystal to direct light based upon polarization and drive voltage. By modulating the signal to the crystal a polarized beam coming into the system can either be allowed through or dumped out the side, this allows for a selection of pulses let through the system. Input into the modulator had a polarization of greater than 1000:1 using a Glan-Laser calcite polarizer immediately before entrance aperture.

The beam is sent through the specially designed alkali cell discussed in Section 4.2.1 where is excites the alkali. The only change that the cell has in this experiment from the past is the side windows that were used either as a diagnostic check or covered and now opened to allow for the detection of side fluorescence. On either side of the alkali cell are photo multiplier tubes (PMT). On one side is a Burle C31034 PMT connected to a Standford Research Systems Model PS325 power supply set at 1,700V. The other side has a Hamamatsu R943-02 PMT connected to another PS325 power supply set at 2,000V. Output from the PMTs terminated into a LeCroy Wavepro 7300 3 GHz oscilloscope. Time bases is 50 ns/div with data being averaged over 5,000 sweeps. The Burle has a 1nm wide band-pass filter center on the D_2 (780nm) line with a similar filter center on the D_1 (795nm) line sitting in front of the Hamamatsu PMT. These filters in this arrangement allow for the side fluorescence on either line to be measured simultaneously.
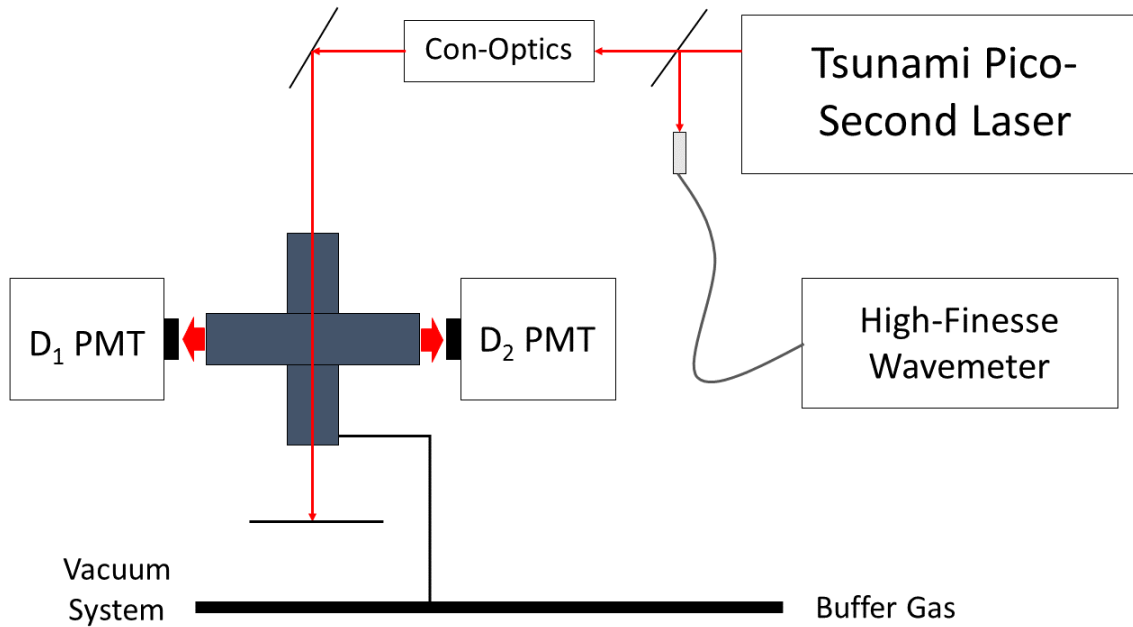

Figure 5.1: Setup for the Spin-Orbit (SO) relaxation rates experiment

During testing the Rb containment cell would be filled with both alkali and helium. The helium used was 99.9999% purity and was added into and removed out of the system via the gas handling system after going through a SAES MC1-902F gas getter. Vacuum pressures for the system could reach down to 11 μTorr with higher pressure ranges reach approximately 750 Torr when helium was added to the system. Pressures were monitored on the low end via an Agilent model FRG-700 manometer with a XGS-600 signal conditioner. The high end pressures were monitored using an MKS model 609A 1,000 Torr manometer connected to a model 670 signal conditioner.

To determine the wavelength of the pump sources a small portion of the beam was split off the optical train using the front reflection of a fused silica window which was then coupled into a fiber. The fiber terminated in a High-Finesse wavemeter to give the pump wavelength. The pump wavelength has a spectral width of approximately 1.5 GHz and appeared to be stable to approximately 0.01 wavenumber. The calibration of the wavemeter was checked using a vacuum sealed Rb^{87} cell. Using this cell the laser could be swept across the hyperfine lines of the un-broadened transition.

Throughout the experiment the 80 MHz pulsed laser could be used in one of two ways. The first mode of operation consisted of using the laser in it's pulsed form allowing every pulse to go through the con-optics modulator. These pulses were stable to within 50 Hz of the 80 MHz rep-rate, and were used to trigger the Oscilloscope signal. The second mode of operation used the modulator described above in pulse picking mode where it would be set to allow 1 pulse through and then dump the next 24 pulses.

5.2.1 Procedure.

The procedure for cell preparation did not vary with the pump source operating mode. The cell is initially evacuated using the roughing pump to get down to the millitorr region. Once there the turbo-pump is activated to bring the system further into the micro-torr region. Once the cell has been evacuated the temperature of the cell is slowly raised.

This allows for anything that may be left on the walls of the cell such as water vapor or atmospheric gases to be desorbed and removed via the vacuum system. The heating for this is provided by the BriskHeat BWH1010 heater tape wrapped around the cell controlled with two Watlow PID temperature controllers and 2 K-type thermocouples. The alkali pool temperature is kept separate from the rest of the cell and is not important during this preparation step. Once the cell has reached between 698 K and 723 K it is allowed to stay at this temperature for a few hours before being cooled back down to 373 K.

To fill the cell with alkali the cell was set at 373 K with the alkali pool set to 338 K. The alkali pool was opened with the turbo pump on to remove any last traces of helium that may have been in the cell. Once the pressure was back down to vacuum pressure (typically after 10-15 seconds) the connection from the cell to the vacuum system is closed and the alkali is allowed to fill the cell. The filling of the cell with alkali typically takes anywhere from 60 to 90 min with the check being a visual inspection to see the fluorescences coming off of the pumped area. At this point the cell is ready for the addition of helium gas. Gas was added slowly, when required, at a rate of approximately 0.2 - 0.5 Torr per second at the lower pressures, and at higher pressures up to 2 Torr per second.

5.3 Observed Fluorescence

The signal from the side fluorescence experiment varied depending on the mode of operation of the laser. Without pulse picking the temporally resolved side fluorescence from the parent $^2P_{3/2}$ state (D_2 line intensity) and from the satellite $^2P_{1/2}$ (D_1 line intensity) is provided in Fig. 5.2 with the corresponding laser intensity being shown in Fig. 5.3. The pump pulses are separated by 12.5 ns (80 MHz) and exhibit a variation in peak intensity of 9%. Without any buffer gas within the system the natural decay time of the pumped D_2 state is the inverse of the A coefficient at $3.61 \times 10^7 s^{-1}$ or about 27.7 ns. Without anything to speed up the decay time, such as buffer gas, the excited Rb atoms do not have time to fully decay away before the next pulse. The emission from the parent state is largely independent

93

of pressure with an exponential decay following each excitation. Each decay exhibits three oscillations, reflecting the pump pulse shape. A large jump from the low pressure signal to the higher pressure signals is due to line shape effects where the un-broadened line at low pressure is not large enough to match the pump. At the higher pressures the transition line shape and the pump become closer matched.

The temporally resolved emission from the satellite $^2\text{P}_{1/2}$ state is weaker and depends strongly on on He pressure. One would expect a double exponential, rising and falling, response to the short pulsed excitation, consistent with the more rounded oscillations seen in Figure 5.2(b).

With pulse picking, the pump signal is shown in Fig 5.5. This partially suppressed pump lead to the signal for the D_1 and D_2 transitions shown in Fig 5.4. Unfortunately, the ConOptics pulse picker does not fully isolate subsequent pulses. The second pulse is only attenuated to approximately 25% of the peak with the subsequent pulses down in the 10% range. Causes of this phenomenon may include crystal coating problems, incorrectly matched impedances in the line, or unknown alignment issues. An attempt was made to work with the manufacturer to solve the problems but time available became an issue. While the temporal decay dynamics are enhanced with pulse picking, interpretation appears complicated by the varying pulse attenuations.

The signals from the two operating mode are similar to each other, but very different in the approach needed to understand them. While allowing all of the pulses through we see a quasi-CW experiment with an oscillating decay feature indicative of a pulsed experiment. The pulse-picked mode then shows a quasi-pulsed experiment where the non-suppressed pulses show and offset and re-excitation features that are indicative of a CW experiment. This hybrid pump approach was not intentional at the onset of the experiment, but became the mode of operation due to problems with laser and pulse picker performance.
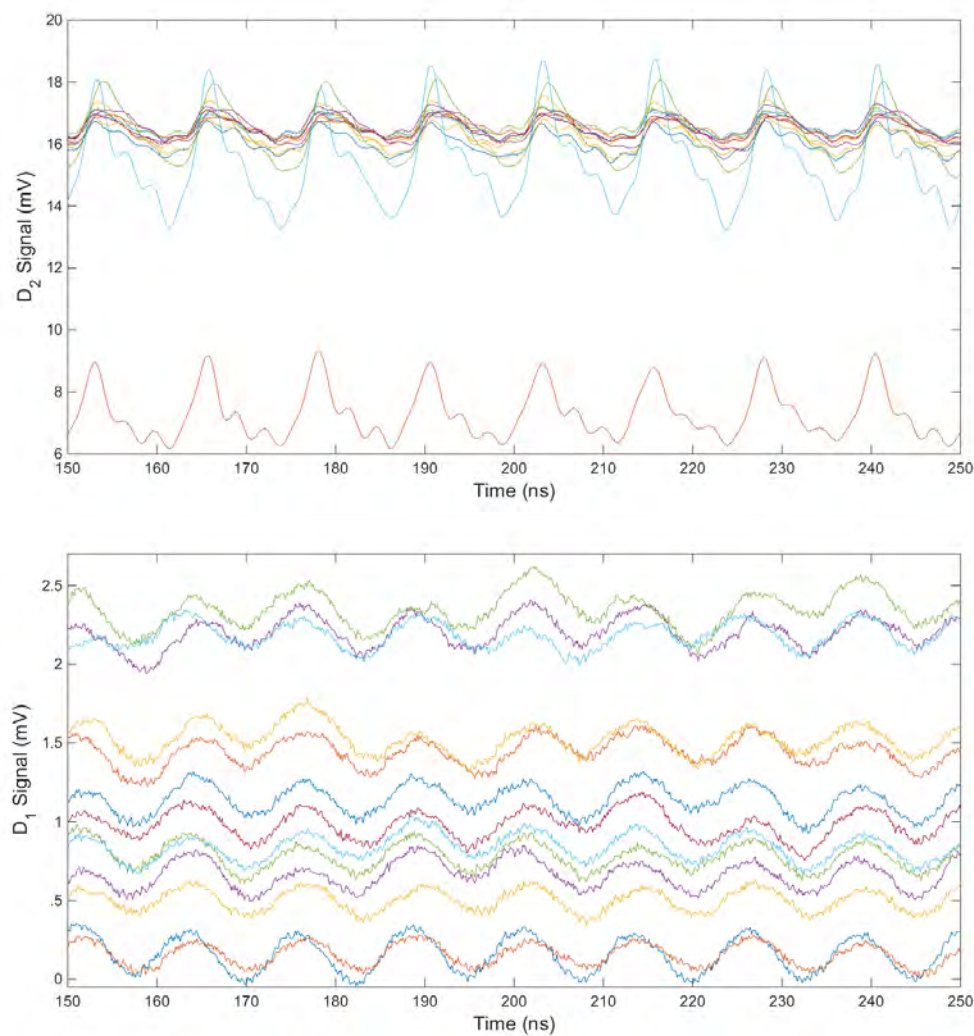
Figure 5.2: Raw Experimental data for the D_1 and D_2 transitions while pumping along the D_2 line at 373 K. Pressures shown, from bottom to top, are 0 Torr, 5.2 Torr, 9.7 Torr, 14.8 Torr, 19.4 Torr, 30.5 Torr, 49.1 Torr, 75.1 Torr, 106.7 Torr, 287.4 Torr, 503.4 Torr, 730.4 Torr.
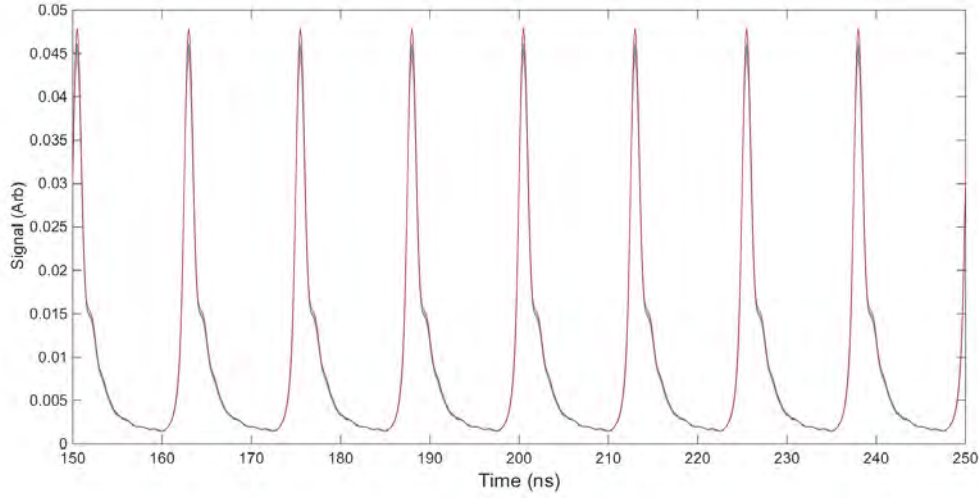
Figure 5.3: Laser pump signal at 80 MHz with no pulse picking.

5.4   Analysis

5.4.1   Quasi-CW Pumping.

The analysis of the observed data differs depending on what mode the system was being operated in. Without pulse picking enabled in the system the resulting data closely resembles the expectations of a CW pumped experiment. One of the best executions of the CW experiment was done by Pitz [64]. Solving the equations of state given in equation 2.6, we can get the steady state relative populations:

$$\left[\frac{N_1}{N_2}\right]_{PumpD_2} = \left(\frac{I_{D_1}}{I_{D_2}}\right)\left(\frac{d_2}{d_1}\right) = \frac{k_{12}[M]}{A_1 + (k_{10} + k_{21})[M]} \tag{5.1}$$

$$\left[\frac{N_2}{N_1}\right]_{PumpD_2} = \left(\frac{I_{D_2}}{I_{D_1}}\right)\left(\frac{d_1}{d_2}\right) = \frac{k_{21}[M]}{A_2 + (k_{20} + k_{12})[M]} \tag{5.2}$$

With these two steady state equations it becomes possible to determine the spin orbit rates via a ratio of the satellite to the parent. An attempt to do this was made for this data set. The average value was determined of both the satellite and the parent in order to remove the pulsing features. Those values were then ratioed against each other for a variety of He pressures that ranged from 5 Torr up to 730 Torr to create a Stern-Volmer plot. In the above

96
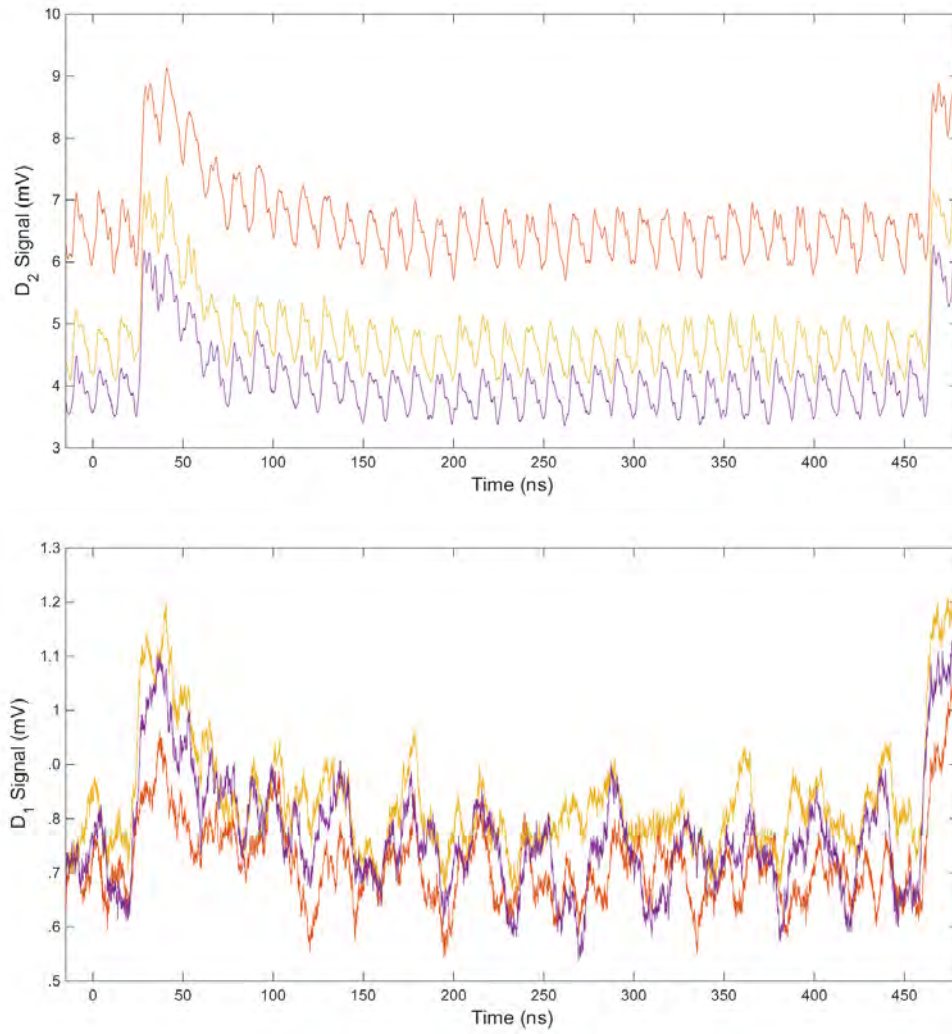
Figure 5.4: Raw Experimental data for the D_1 and D_2 transitions while pumping along the D_2 line with pulse picking. From bottom to top the pressures are 19.4 Torr, 49.5 Torr, and 242.7 Torr

equations there is a d_2/d_1 factor that is the relative detectivity of the system. A detectivity ratio for our system was calculated to be approximately 27.8. The detectivity ratio was calculated using the PMT response curve for either PMT at the set voltage and the another response factor. To calculate the response factor the system was forced to obey detailed
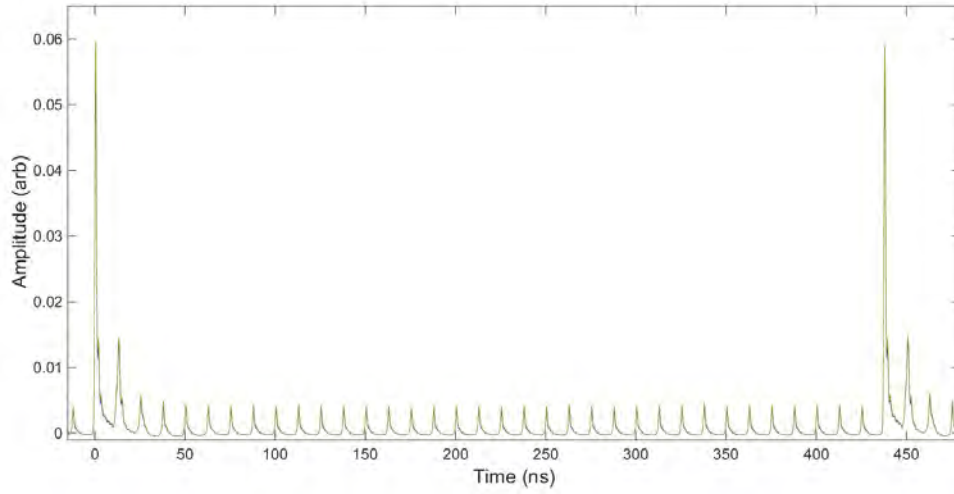
Figure 5.5: Laser Pump Signal at 80 MHz with pulse picking.

balance given by:

$$\frac{k_{21}}{k_{12}} = \frac{\sigma_{12}}{\sigma_{21}} = \frac{g_2}{g_1}e^{\Delta E/kT} \tag{5.3}$$

Plugging into the detailed balance equation $\Delta E = 237.6$ cm^{-1}, g_2=4, g_1=2, and T = 373K results in a ratio of 0.7998. Taking the inverse of this we can get the back rate is 1.25. By forcing the fitting function given below to reach this ratio of 1.25 the detectivity was determined. The results of this are shown in Fig. 5.6.

When fitting the data shown in Fig. 5.6 to the equation:

$$Y = \frac{Ax}{1 + Bx} \tag{5.4}$$

where $A = k_{12}/A_1$ and $B = k_{21}/A_1$ from equation 5.2. The fits returned values of 8.644×10^{-19} for A and 6.886×10^{-19} for B. Using the value for A and the natural decay rate of 3.61×10^7 sec for A_1 we get that the cross section (σ) is equal to 2.17^{-16} cm^2. This value is more than an order of magnitude larger than those previously reported by Gallagher at 1.18×10^{-17} cm^2 [28] and Sell at approximately 1.15×10^{-17}cm^2 [29]. The larger cross-section value found here may indicate they system was trapped though trapping is unlikely

98

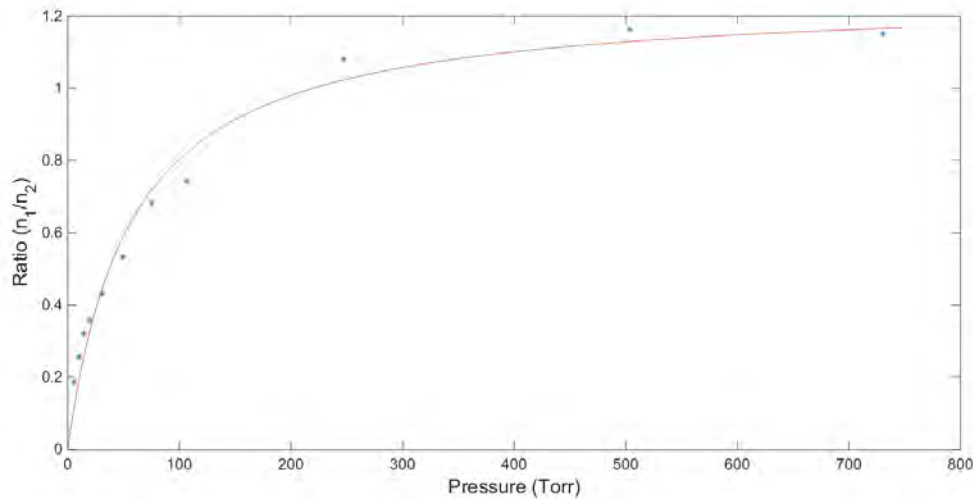Figure 5.6: Ratio of the D_1 and D_2 signals ($\frac{I_{D1}}{I_{D2}}\frac{d_2}{d_1}$) including detector response while pumping the D_2 line at 373 K.

to cause this large of an error. Trapping occurs when the emitted light is reabsorbed before making it to the edge of the cell. Due to time and equipment constraints an effort was made to push on to explore the temperature dependence of these transitions, with the knowledge that the absolute value of the rate is incorrect.

Assuming that the quasi-CW analysis above is valid, the temperature dependence was explored. The system in the quasi-CW pumping configuration was used to pump the alkali cell at 373 K with 17.4 Torr of helium added. This pressure was chosen as it fell in the region of linear growth shown in Fig. 5.6. With the cell filled and sealed off from both the alkali pool and the gas handling system the temperature was systematically increased by 50 K increments from 373 K up to 723 K. Following the same procedures as before the ratios of the transitions were corrected for detectivity with the results shown in Fig. 5.7.

A few items to note here is the linear increase in the spin-orbit mixing rate over the temperature range of 373 K to 523 K. Beyond that, at 573 K and 623 K the rate drops quite significantly. During the experiment visual observation of the cell revealed that the

99
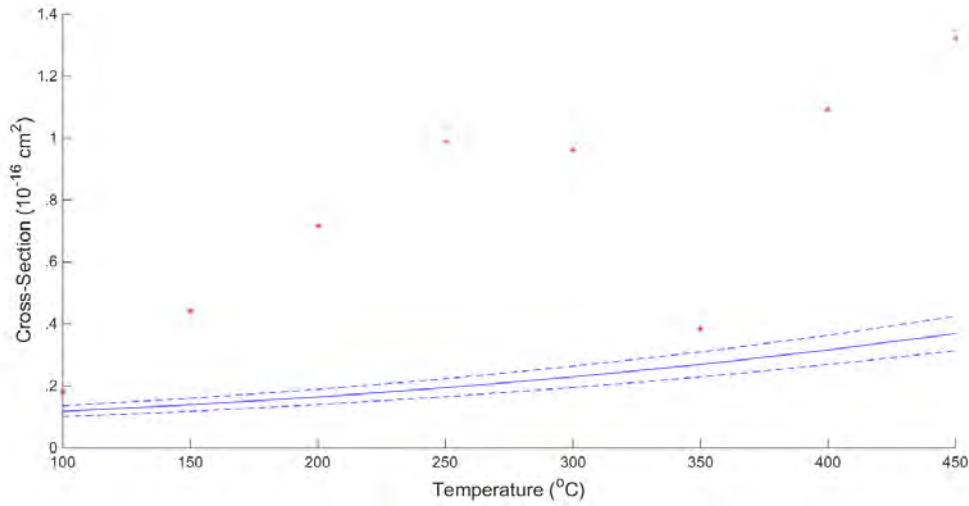
Figure 5.7: Measured temperature dependent cross-section (*) while pumping the D_2 line at 17.4 Torr for a variety of temperatures ranging from 373 K to 723 K. Previously measured cross-sections from [28] shown as (—) with 15% error bounds represented by (- - -).

alkali density inside the cell had risen significantly. This observation was based upon the reference cell no longer receiving the pump beam, and the amount of light emminating from the cell. This indicates that there was alkali plated out somewhere inside the cell that was released from the walls at higher temperatures. The signal can be seen returning at 673 K and 723 K with the same slope as the first temperature range. Visual inspections at this point revealed that the pump beam was once again making it to the reference cell indicating that as the temperature rose the alkali was reacting away within the cell.

A comparison to previous results indicates major systematic problems with the data collection.

5.4.2 *Pulse Picking.*

While operating in the pulse picking mode analysis of the system follows the method described earlier by used by Brown [21]. Using the equations derived earlier for a pulsed experiment it can be shown that the the decay is an exponential decay on the parent

(pumped) transition. The satellite transition (non-pumped) on the other hand will have an exponential increase in amplitude followed by an exponential decay. This feature can be fit using a double exponential. What we see during this type of analysis is that the parent transition has a very rapid rise while the satellite has a slow rise due to population being moved slowly from the parent to the satellite. As more and more buffer gas is added these rises and decays happen more rapidly.

The data shows for our experiment that there is a rapid increase in the signal for the parent transition. This is then followed by the exponential decay that is expected from a pulsed experiment. Before the decay can get back to zero though another pulse comes in to re-excite more of the Rb. An attempt to fit to the overall decay feature does not work as the overall decay due to the extra pulses extends out well beyond the rate at which individual pulses decay away. Attempting to fit to individual pulse decays is not effective either. Since the next pulse comes in before the previous pulse has had a chance to decay away exponential fits to the individual pulses also do not give a reasonable answer. This mode of operation does not conform to the pure pulsed analytic solution.

5.5 Conclusions

The best estimate for the spin-orbit mixing rate from the available data is 3.12×10^{-11} cm^3/s. From the given rate a cross-section of 2.17×10^{-16} cm^2 was observed. This is a factor of 15 larger than previously reported results by Gallagher [28]. The temperature dependence of the rate also shows a much larger increase in magnitude over the temperature range when compared with previous observations. This larger observed cross-section and the lack of repeatability calls into question the validity of the collected data.

The hybrid CW pulsed pumping of the experiment, while not intentionally set out for, did provide some interesting results that required a different type of thinking to interpret. Using the quasi-CW pulsing and a CW type analysis we were able to extract values that are close to those provided in literature from previous experiments. Unfortunately due to

equipment problems and with the analysis able to be carried out up to this point these values do not add anything new to the body of scientific work. Also, variations within the data sets themselves also point to some parameter within the system not being understood and controlled as well as assumed.

Due to the hybrid nature of our pumping and the difficulties analyzing the data that does not fall squarely into either of the well known and well studies regimes. In order to extract usable values a full model will need to be developed that take into account the varying pulse amplitudes and repetition rate. Due to the complications with extracting values from the hybrid pump method measurements done in a pure CW or a pure pulsed environment would be the preferable method for this type of experiment. The alkali cell being used has been shown in other experiments to be sufficient for determining the temperature dependence of various parameters assuming the pumping works. Recommend that in the future, a diagnostic setup is added into the system for detection of alkali density is present in the system, as well as either a full CW or pulsed system that will allow for relaxation before the next pulse hits.

VI. Conclusions

6.1 Work Summary

This work has explored the high-pressure Rb-He line shape parameters to include broadening, γ, shifting, δ, asymmetry, β_0, and secondary blue peak location. The measured broadening rates for ^{4}He D_1 and D_2 lines are 16.1 ± 0.2 MHz/Torr and 17.0 ± 0.3 MHz/Torr respectively. The rates for ^{3}He D_1 and D_2 are 16.8 ± 0.5 MHz/Torr and 19.4 ± 0.4 MHz/Torr. Similarly the shift rates for ^{4}He are 4.60 ± 0.12 MHz/Torr and 0.20 ± 0.14 MHz/Torr with ^{3}He 5.65 ± 0.35 MHz/Torr and 0.65 ± 0.2 MHz/Torr. The broadening and shift rates measured aren't new values, but are used as validation against previous measurements and show that the linearity of the rates extends out to 15,000 Torr. The measured location of the secondary blue peak location is a previously unreported value with the location of 735 nm. The asymmetry of the line shape measured at high pressures gave a shading to the blue of 0.51 ± 0.04 MHz/Torr and 0.24 ± 0.02 MHz/Torr for the D_1 and D_2 of ^{4}He lines respectively. The ^{3}He values for the D_1 and D_2 lines are given as 0.43 ± 0.01 MHz/Torr and 0.30 ± 0.03 MHz/Torr respectively.

The temperature dependence of the shift and broadening rates was also determined over a temperature range of 373 K to 723 K. The previous trusted results covered a much small range of 353 K to 394 K. These increased temperatures represent information not currently in the literature. This increased temperature range also allows for the comparison to various theoretical predictions over a much greater temperature range. The shift coefficient ranges from 4.36 MHz/Torr to 5.35 MHz/Torr for the D_1 line and a much smaller observed shift of .42 MHz/Torr to .99 MHz/Torr over the temperature ranges. Broadening coefficients range from 17.8 MHz/Torr to 18.9 MHz/Torr for the D_1 transition and 18.5 MHz/Torr to 20.5 MHz/Torr for the D_2 transition.

The measured spin-orbit rate at 373 K was observed to be 2.17×10^{-16} cm^2. This rate is approximately 15 times higher than previously reported values. The temperature dependence of the rate at low pressure was also shown to vary with temperature three times more than the best literature observations. The exceedingly large spin-orbit rates coupled with the rapidly varying temperature dependence of the rates show there were large systematic errors within the experiment.

In order to measure these values at increased temperatures a new alkali containment cell was needed. Throughout this research effort a two temperature alkali cell was developed and built. Though the new cell allowed for temperature measurements at previously unreached temperatures the use of the cell was very procedurally intensive. The procedures for using the cell were developed through trial and error, but are now at the level necessary for continued experimentation.

6.2   DPAL Impact

This research will have several important impacts on the scientific community's understanding of the DPAL system. The scientific foundation of the DPAL system is the interaction between the alkali and the buffer gas used. These interactions are modeled by the potential energy surfaces that can then be used by various theoretical models to predict parameters such as line shape and mixing rates. Currently those potential energy surfaces are incomplete in their level of refinement.

The core line shape measurements made for the temperature dependence of the shift and broadening are very sensitive to the long range potentials. The short range potentials then greatly effect the wings of the line shape determined by the high pressure measurements made. These line shape parameters can be used to empirically modify the potential energy surfaces. Then using the new surfaces a check on their validity is to predict the temperature dependence of the spin-orbit mixing rate.

On the engineering side these measurements will be useful in scaling the DPAL to high powers. As discussed earlier in order to make a DPAL work the excited atoms must transition from the upper excited state to the lower state before the system can lase. If this rate is not fast enough the system bottlenecks and efficiency drops. A simple view of the solution is to just add more buffer gas to increase the rate. This will have other consequences within the system though. As stated earlier the temperature changes within the system can be up to 300 K over just a few cm of length. With a temperature gradient this large the mixing rate can vary throughout the system where there may be bottlenecking in some spots while not in others. By increasing the pressure one could increase the mixing rate so that the slowest rate is sufficient to prevent bottlenecking.

Increasing the pressure in the system amplifies the effects of the temperature dependence of the broadening and shifting rates. In order to get the most out of the DPAL system temperature variations within the system need to be accounted for and corrected to maximize laser efficiency, power output, and beam quality.

6.3   Recommendation for future work

The first recommendation for future work is a complete measurement of the spin-orbit mixing rates. To do this work the current alkali cell should be used as it has been proven to work well over the temperature ranges up to $450^{o}C$. A change to the experimental setup would be the addition of a laser diagnostic to measure the amount of alkali vapor in the cell. After that either a pure CW or pure pulsed method should be employed. The hybrid quasi-CW pumping method used while interesting did not provide the results needed.

The temperature ranges, while greater than previous results, could be increased. An increase in the upper range of the temperature could be accomplished using the same techniques used here, but would required different materials. Ceramic heaters and different cell materials could be used to reach in the 2,000 - 3,000 K range. To get an increase in the lower end temperatures would require a completely different approach. To get very low

temperatures an alkali vapor would need to be made, and then cooled without condensing out the alkali. One possible method would be to flow the system through a supersonic nozzle where the corresponding decrease in pressure would also drop the temperatures below what would be possible with a standard setup.

Due to the success of these measurements a strong recommendation would be to revisit these same experiments with no modification in order to procure the results for the other alkali and noble gas interactions. This would have the two-fold benefit of expanding the kinetics database and provide the theorists with more data to compare their models to. With the Rb-He being one of the simplest interactions due to the nature of helium being the smallest and lightest it is most likely to be closest to correct. The other noble gases represent a more challenging case to match and will give more confidence in the correctness of the surfaces.

As was determined during comparison to theoretical predictions, the various models and surfaces are not yet correct. It appears that some modification of the current potential surfaces could result in results close to those obtained experimentally. The theory also postulates as difference in the emission and absorption spectra that has not been explored. An emission measurement that encompasses the wings of the line shape would be useful in confirming or disproving the difference in emission and absorption. Possibly a CW pumped excitation experiment with a scanning monochromator viewing the side fluorescence could be used.

Appendix: Conversion Factors

A.1 Shift and Broadening Unit Conversions

Shift and broadening rates are reported in a variety of ways through the literature. In order to facilitate an apples to apples type comparison each of the reported values were converted to MHz/Torr, which is the standard this group uses while reporting results. Below are the four other units along with how they are converted into MHz/Torr. The final equation of each section gives a single number and temperature variable that can be directly applied as the conversion factor.

The first reported units are in wavenumbers per concentration.

$$\left(\frac{cm^{-1}}{cm^{-3}}\right) \Rightarrow \left(\frac{MHz}{Torr}\right)$$

Wavenumbers are converted to frequency using the speed of light (c). The ideal gas law is used to relate number density (n) to pressure.

$$\left(\frac{cm^{-1}}{cm^{-3}}\right)\left(\frac{c}{k_B T}\right) = \left(\frac{MHz}{Torr}\right)$$

$$\left(\frac{cm^{-1}}{cm^{-3}}\right)\left(\frac{2.9979x10^4 \; cm \; MHz}{1.38064x10^{-23} \; (Pa \; m^3 \; K^{-1})T}\right)\left(\frac{133.322Pa}{Torr}\right)\left(\frac{1m}{100cm}\right)^3 = \left(\frac{MHz}{Torr}\right)$$

$$\left(\frac{cm^{-1}}{cm^{-3}}\right)\left(\frac{2.89493x10^{23}}{T}\right) = \left(\frac{MHz}{Torr}\right) \tag{A.1}$$

To convert to MHz/Torr take the reported value, multiply by the given conversion factor and divide by the temperature in Kelvin.

Another set of reporting units is wavenumbers per relative density (r.d.)

$$\left(\frac{cm^{-1}}{r.d.}\right) \Rightarrow \left(\frac{MHz}{Torr}\right)$$

where r.d. is the relative density compared to an ideal gas at 760 Torr at 273.15 K which has 2.69×10^{19} cm^{-3}. Wavenumbers are converted to frequency using the speed of light (c).

$$\left(\frac{cm^{-1}}{r.d.}\right)\left(\frac{c}{k_B T}\right) = \left(\frac{MHz}{Torr}\right)$$

$$\left(\frac{cm^{-1}}{r.d.}\right)\left(\frac{10761.8}{T}\right) = \left(\frac{MHz}{Torr}\right)$$

(A.2)

To convert to MHz/Torr take the reported value, multiply by the given conversion factor and divide by the temperature in Kelvin.

Some reported values for the broadening and shifting us frequency per concentration.

$$\left(\frac{Hz}{cm^{-3}}\right) \Rightarrow \left(\frac{MHz}{Torr}\right)$$

The concentration is converted to a pressure using the ideal gas law.

$$\left(\frac{Hz}{cm^{-3}}\right)\left(\frac{1}{k_B T}\right) = \left(\frac{MHz}{Torr}\right)$$

$$\left(\frac{Hz}{cm^{-3}}\right)\left(\frac{133.322 Pa/Torr}{1.38064 x 10^{-23} \ (Pa \ m^3 \ K^{-1})T}\right)\left(\frac{1MHz}{1x10^6 Hz}\right)\left(\frac{1m}{100cm}\right)^3 = \left(\frac{MHz}{Torr}\right)$$

$$\left(\frac{Hz}{cm^{-3}}\right)\left(\frac{9.65654 x 10^{12}}{T}\right) = \left(\frac{MHz}{Torr}\right)$$

(A.3)

To convert to MHz/Torr take the reported value, multiply by the given conversion factor and divide by the temperature in Kelvin.

The last units that shift and broadening are reported in is frequency per amagat.

$$\left(\frac{GHz}{amg}\right) \Rightarrow \left(\frac{MHz}{Torr}\right)$$

An amagat (η) is defined as the number density of an ideal gas at 101.325 kPa (760 Torr) at 273.15 K

$$\eta = \left(\frac{p}{p_0}\right)\left(\frac{T_0}{T}\right)$$

The conversion from amagat to pressure requires the given T_0 temperature of 273.15 K and the pressure of 760 Torr as shown below.

$$\left(\frac{GHz}{amg}\right)\left(\frac{273.15K}{T}\right)\left(\frac{1}{760Torr}\right)\left(\frac{1x10^3 MHz}{1GHz}\right) = \left(\frac{MHz}{Torr}\right)$$

$$\left(\frac{GHz}{amg}\right)\left(\frac{359.211}{T}\right) = \left(\frac{MHz}{Torr}\right)$$

(A.4)

To convert to MHz/Torr take the reported value, multiply by the given conversion factor and divide by the temperature in Kelvin.

A.2 Asymmetry Parameter Comparison

$$S(v) = \frac{A\,[1 + 0.664\;2\pi\;T_d(v - v_c)]}{(v - v_c)^2 + (\gamma/2)^2} \tag{A.5}$$

$$I(v) = 2\left(\frac{c}{w}\right)e^{-n\alpha_0}cos(n\beta_0)\frac{n\alpha_1}{(n\alpha_1)^2 + (2\pi cv/w - n\beta_1)^2} +$$
$$2\left(\frac{c}{w}\right)e^{-n\alpha_0}sin(n\beta_0)\frac{n\alpha_1(2\pi cv/w - n\beta_1)}{(n\alpha_1)^2 + (2\pi cv/w - n\beta_1)^2} \tag{A.6}$$

Equation A.5 has the asymmetry parameter given as T_d which needs to be compared to our asymmetry parameter given as $n\beta_0$. In order to compare the equations the first step is to use the small angle approximation for cos and sin for Equation A.6 to get:

$$2\left(\frac{c}{w}\right)e^{-n\alpha_0}\frac{[1 + n\beta_0(2\pi cv/w - n\beta_1)]}{(n\alpha_1)^2 + (2\pi cv/w - n\beta_1)^2} \tag{A.7}$$

Now that Equations A.5 and A.7 and in the same format we can see that:

$$A = 2\left(\frac{c}{w}\right)e^{-n\alpha_0}n\alpha_1$$

$$(v - v_c) = (2\pi cv/w - n\beta_1)$$

$$(\gamma/2) = (n\alpha_1)$$

and most importantly allows the comparison of the two asymmetry parameters by:

$$n\beta_0 = (0.664)(2\pi)T_d \tag{A.8}$$

Bibliography

[1] Allard, NF, A Royer, JF Kielkopf, and N Feautrier. "Effect of the variation of electric-dipole moments on the shape of pressure-broadened atomic spectral lines". *Physical Review A*, 60(2):1021, 1999.

[2] Allard, NF and F Spiegelman. "Collisional line profiles of rubidium and cesium perturbed by helium and molecular hydrogen". *Astronomy & Astrophysics*, 452(1):351–356, 2006.

[3] Allard, Nicole and John Kielkopf. "The effect of neutral nonresonant collisions on atomic spectral lines". *Reviews of Modern Physics*, 54:1103–1182, Oct 1982. URL http://link.aps.org/doi/10.1103/RevModPhys.54.1103.

[4] Anderson, PW and JD Talman. "Pressure broadening of spectral lines at general pressures". *Bell System Technical Publication*, 3117, 1956.

[5] Arnold, E, W Borchers, HT Duong, P Juncar, J Lerme, Peter Lievens, W Neu, R Neugart, M Pellarin, J Pinard, et al. "Optical laser spectroscopy and hyperfine structure investigation of the 102S, 112S, 82D, and 92D excited levels in francium". *Journal of Physics B: Atomic, Molecular and Optical Physics*, 23(20):3511, 1990.

[6] Banerjee, A, D Das, and V Natarajan. "Absolute frequency measurements of the D1 lines in 39K, 85Rb, and 87Rb with $\approx$ 0.1 ppb uncertainty". *Europhysics Letters*, 65(2):172, 2004.

[7] Baranger, Michel. "Simplified quantum-mechanical theory of pressure broadening". *Physical Review*, 111(2):481, 1958.

[8] Barwood, GP, P Gill, and WRC Rowley. "Frequency measurements on optically narrowed Rb-stabilised laser diodes at 780 nm and 795 nm". *Applied Physics B*, 53(3):142–147, 1991.

[9] Beahn, TJ, WJ Condell, and HI Mandelberg. "Excitation-Transfer Collisions between Rubidium and Helium Atoms". *Physical Review*, 141(1):83, 1966.

[10] Bean, BL and RH Lambert. "Temperature dependence of hyperfine density shifts. III. ^{23}Na, ^{39}K, and ^{85}Rb in He, Ne, Ar, and N$_2$". *Physical Review A*, 12(4):1498, 1975.

[11] Bean, BL and RH Lambert. "Temperature dependence of hyperfine density shifts. IV. ^{23}Na, ^{39}K, and ^{85}Rb in He, Ne, Ar, and N$_2$ at low temperatures". *Physical Review A*, 13(1):492, 1976.

[12] Belov, VN. "Measurement of the constants for the broadening and shift of the D$_2$ line of rubidium (780.0 nm) by inert gases". *Optics and Spectroscopy*, 51:209–211, 1981.

110

[13] Berriche, Hamid. "Electronic, spectra, and spin orbit interaction for FrAr van der Waals system". *International Journal of Quantum Chemistry*, 113(9):1349–1357, 2013.

[14] Blank, Aaron L. *Potential Energy Curves and Associated Line Shape of Alkali-Metal and Noble-Gas Interactions*. PhD Dissertation, Air Force Institute of Technology, 2014.

[15] Blank, L and David E Weeks. "Impact broadening, shifting, and asymmetry of the D_1 and D_2 lines of alkali-metal atoms colliding with noble-gas atoms". *Physical Review A*, 90(2):022510, 2014.

[16] Blank, L, David E Weeks, and Gary S Kedziora. "M + Ng potential energy curves including spin-orbit coupling for M = K, Rb, Cs and Ng = He, Ne, Ar". *The Journal of Chemical Physics*, 136(12):124315, 2012.

[17] Boesten, HMJM, CC Tsai, JR Gardner, DJ Heinzen, and BJ Verhaar. "Observation of a shape resonance in the collision of two cold Rb 87 atoms". *Physical Review A*, 55(1):636, 1997.

[18] Bogachev, A V, Sergey G Garanin, A M Dudov, V A Eroshenko, S M Kulikov, G T Mikaelian, V A Panarin, V O Pautov, A V Rus, and Stanislav A Sukharev. "Diode-pumped caesium vapour laser with closed-cycle laser-active medium circulation". *Quantum Electronics*, 42(2):95, 2012.

[19] Bouhadjar, F, K Alioua, MT Bouazza, and M Bouledroua. "Rubidium D1 and D2 atomic lines pressure broadened by ground-state helium atoms". *Journal of Physics B: Atomic, Molecular and Optical Physics*, 47(18):185201, 2014.

[20] Bradley, Michael P, James V Porto, Simon Rainville, James K Thompson, and David E Pritchard. "Penning Trap Measurements of the Masses of C 133 s, R 8 7, 8 5 b, and N 23 a with Uncertainties 0.2 ppb". *Physical Review Letters*, 83(22):4510, 1999.

[21] Brown, Kirk C. and Glen P. Perram. "Spin-orbit relaxation and quenching of cesium $7\,^2P$ in mixtures of helium, methane, and ethane". *Physical Review A*, 85:022713, Feb 2012.

[22] Carrington, C Gerald and Alan Gallagher. "Blue satellite bands of Rb broadened by noble gases". *Physical Review A*, 10(5):1464, 1974.

[23] Cohen, James S and Barry Schneider. "Ground and excited states of Ne2 and Ne2$^+$. I. Potential curves with and without spin-orbit coupling". *The Journal of Chemical Physics*, 61(8):3230–3239, 1974.

[24] Dhiflaoui, J and H Berriche. "One-Electron Pseudopotential Investigation of CsAr van der Waals System Including the Spin- Orbit Interaction". *The Journal of Physical Chemistry A*, 114(26):7139–7145, 2010.

111

[25] Dhiflaoui, J, H Berriche, M Herbane, AG AlSehimi, and MC Heaven. "Electronic Structure and Spectra of the RbAr van der Waals System Including Spin–Orbit Interaction". *The Journal of Physical Chemistry A*, 116(43):10589–10596, 2012.

[26] Drummond, DL and Alan Gallagher. "Potentials and continuum spectra of Rb-noble gas molecules". *The Journal of Chemical Physics*, 60(9):3426–3435, 1974.

[27] Durand, Philippe and Jean-Claude Barthelat. "A theoretical method to determine atomic pseudopotentials for electronic structure calculations of molecules and solids". *Theoretica chimica acta*, 38(4):283–302, 1975.

[28] Gallagher, Alan. "Rubidium and cesium excitation transfer in nearly adiabatic collisions with inert gases". *Physical Review*, 172(1):88–96, 1968.

[29] Gearba, MA, JF Sell, BM Patterson, R Lloyd, J Plyler, and RJ Knize. "Temperature dependence of Rb 5P fine-structure transfer induced by ^{4}He collisions". *Optics letters*, 37(10):1637–1639, 2012.

[30] Gourevitch, A, G Venus, V Smirnov, DA Hostutler, and L Glebov. "Continuous wave, 30 W laser-diode bar with 10 GHz linewidth for Rb laser pumping". *Optics letters*, 33(7):702–704, 2008.

[31] Granier, J and R Granier. "Temperature effect on the displacement and broadening of the resonance lines of rubidium excited by argon". 1966.

[32] Gutterres, RF, C Amiot, A Fioretti, C Gabbanini, M Mazzoni, and O Dulieu. "Determination of the ^{87}Rb 5p state dipole matrix element and radiative lifetime from the photoassociation spectroscopy of the Rb$_2$ 0_g^-(P$_{3/2}$) long-range state". *Physical Review A*, 66(2):024502, 2002.

[33] Hager, GD and GP Perram. "A three-level analytic model for alkali metal vapor lasers: part I. Narrowband optical pumping". *Applied Physics B*, 101(1-2):45–56, 2010.

[34] Hager, Gordon D, Gordon E Lott, Aaron J Archibald, L Blank, David E Weeks, and Glen P Perram. "High pressure line shapes for Cs D$_1$ and D$_2$ lines and empirically informed interaction potentials". *Journal of Quantitative Spectroscopy and Radiative Transfer*, 147:261–273, 2014.

[35] Hager, Gordon D and Glen P Perram. "A three-level model for alkali metal vapor lasers. Part II: broadband optical pumping". *Applied Physics B*, 112(4):507–520, 2013.

[36] Hickling, Holly L, Larry A Viehland, Dessa T Shepherd, Pavel Soldán, Edmond PF Lee, and Timothy G Wright. "Spectroscopy of M$^+$·Rg and transport coefficients of M$^+$ in Rg (M = Rb–Fr; Rg = He–Rn)". *Physical Chemistry Chemical Physics*, 6(17):4233–4239, 2004.

[37] Hindmarsh, William Russell and Judith M Farr. "Collision broadening of spectral lines by neutral atoms". *Progress in Quantum Electronics*, 2:141–214, 1973.

[38] Hurd Jr, Edward J. *Characteristics of a High Intensity, Pulsed, Potassium Vapor Laser in a Heat Pipe*. Master's Thesis, 2011.

[39] Izotova, SL, AI Kantserov, and MS Frish. "Constants for broadening and shift of D_1 and D_2 rubidium-87 lines by inert gases". *Optics and Spectroscopy*, 51:107–109, 1981.

[40] Jones, J. E. "On the Determination of Molecular Fields. II. From the Equation of State of a Gas". *Royal Society of London Proceedings Series A*, 106:463–477, 1924.

[41] Kantor, P Ya and LN Shabanova. "Profiles of the Rbi 794.7-and 780.0-nm lines in the presence of inert gases; parameters of interatomic potentials". *Optics and Spectroscopy*, 58:614–619, 1985.

[42] Kazantsev, SA, NI Kaliteevskii, and OM Rish. "Application of the magnetic scanning technique for measuring the broadenings and shifts of the D_1 resonance line of rubidium caused by inert gases". *Optics and Spectroscopy*, 44:372–375, 1978.

[43] Kielkopf, John F. "Predicted alkali collision broadening by noble gases based on semiempirical potentials". *Journal of Physics B: Atomic and Molecular Physics*, 9(17):L547, 1976.

[44] Kluttz, Kelly A., Todd D. Averett, and Brian A. Wolin. "Pressure broadening and frequency shift of the D_1 and D_2 lines of Rb and K in the presence of ^{3}He and N_2". *Physical Review A*, 87:032516, 2013.

[45] Krause, L. "Collisional Excitation Transfer Between the $^2P_{1/2}$ and $^2P_{3/2}$ Levels in Alkali Atoms". *Applied Optics*, 5(9):1375–1382, 1966.

[46] Krupke, William F. "Diode-pumped alkali laser", 2003. US Patent 6,643,311.

[47] Krupke, William F. "Diode pumped alkali lasers (DPALs) - A review (rev1)". *Progress in Quantum Electronics*, 36(1):4–28, 2012.

[48] Krupke, William F, Raymond J Beach, V Keith Kanz, and Stephen A Payne. "Resonance transition 795-nm rubidium laser". *Optics Letters*, 28(23):2336–2338, 2003.

[49] Langhoff, PW and M Karplus. "Pade summation of the cauchy dispersion equation". *Journal of the Optical Society of America*, 59(7):863–871, 1969.

[50] Larson, B, O Hausser, PPJ Delheij, DM Whittal, and D Thiessen. "Optical pumping of Rb in the presence of high-pressure He 3 buffer gas". *Physical Review A*, 44(5):3108, 1991.

[51] Lewis II, Charlton D. *Non-Adiabatic Atomic Transitions: Computational Cross Section Calculations of Alkali Metal-Noble Gas Collisions*. PhD Dissertation, Air Force Institute of Technology, 2011.

[52] Lide, David R. "CRC handbook of physics and chemistry", 2001.

[53] Loper, Robert D. *Collisional broadening and shift of D1 and D2 spectral lines in atomic alkali vapor-noble gas systems*. PhD Dissertation, Air Force Institute of Technology, 2013.

[54] Mastromarino, PA, CR Otey, D Pripstein, and EW Hughes. "Tunable diode laser study of pressure broadening of Rb D_1 lines in the presence of ^{4}He buffer gas". *Nuclear Instruments and Methods in Physics Research Section B: Beam Interactions with Materials and Atoms*, 194(1):69–77, 2002.

[55] Merritt, Jeremy M, Jiande Han, Terry Chang, and Michael C Heaven. "Theoretical investigations of alkali metal: rare gas interaction potentials". *SPIE LASE: Lasers and Applications in Science and Engineering*, 71960H–71960H. International Society for Optics and Photonics, 2009.

[56] Miller, WS, CV Sulham, JC Holtgrave, and GP Perram. "Limitations of an optically pumped rubidium laser imposed by atom recycle rate". *Applied Physics B*, 103(4):819–824, 2011.

[57] Moore, CE. "Atomic energy levels NSRDS-NBS". *Circular No. 467*, volume 2. US GPO Washington, 1971.

[58] Müller, Wolfgang, Joachim Flesch, and Wilfried Meyer. "Treatment of intershell correlation effects in abinitio calculations by use of core polarization potentials. Method and application to alkali and alkaline earth atoms". *The Journal of Chemical Physics*, 80(7):3297–3310, 1984.

[59] Nesmeyanov, Andrei Nikolaevich and JI Carasso. *Vapour pressure of the elements*. Infosearch, 1963.

[60] Ottinger, Ch, Richard Scheps, GW York, and Alan Gallagher. "Broadening of the Rb resonance lines by the noble gases". *Physical Review A*, 11(6):1815, 1975.

[61] Perram, Glen P. "High Power DPAL Scaling and Efficiency Kinetics", June 2012. MDA ATI BAA (HQ0147-11-ATI-BAA).

[62] Perram, Glen P, Salvatore J Cusumano, Robert L Hengehold, and Steven T Fiorino. *An Introduction to Laser Weapon Systems*. Directed Energy Professional Society, 2010.

[63] Pitz, Greg A, Charles D Fox, and Glen P Perram. "Pressure broadening and shift of the cesium D_2 transition by the noble gases and N_2, H_2, HD, D_2, CH_4, C_2H_6, CF_4, and He_3 with comparison to the D_1 transition". *Physical Review A*, 82(4):042502, 2010.

[64] Pitz, Greg A, Charles D Fox, and Glen P Perram. "Transfer between the cesium 6 $^2P_{1/2}$ and 6 $^2P_{3/2}$ levels induced by collisions with H_2, HD, D_2, CH_4, C_2H_6, CF_4, and C_2F_6". *Physical Review A*, 84(3):032708, 2011.

[65] Pitz, Greg A, Gordon D Hager, Tiffany B Tafoya, Joseph W Young, Glen P Perram, and David A Hostutler. "An experimental high pressure line shape study of the rubidium D_1 and D_2 transitions with the noble gases, methane, and ethane". *SPIE LASE*, 896208–896208. International Society for Optics and Photonics, 2014.

[66] Pitz, Greg A, Douglas E Wertepny, and Glen P Perram. "Pressure broadening and shift of the cesium D_1 transition by the noble gases and N_2, H_2, HD, D_2, CH_4, C_2H_6, CF_4, and He_3". *Physical Review A*, 80(6):062718, 2009.

[67] Romalis, MV, E Miron, and GD Cates. "Pressure broadening of Rb D_1 and D_2 lines by ^3He, ^4He, N_2, and Xe: Line cores and near wings". *Physical Review A*, 56(6):4569, 1997.

[68] Rotondaro, Matthew D and Glen P Perram. "Collisional broadening and shift of the rubidium D_1 and D_2 lines ($5^2S_{1/2} \rightarrow 5^2P_{1/2}$, $5^2P_{3/2}$ by rare gases, H_2, D_2, N_2, CH_4 and CF_4". *Journal of Quantitative Spectroscopy and Radiative Transfer*, 57(4):497–507, 1997.

[69] Roueff, E and A Suzor. "Broadening, shift and depolarization of broad fine structure alkali spectral lines by helium". *Journal de Physique*, 35(10):727–740, 1974.

[70] Sasso, A., W. Demtröder, T. Colbert, C. Wang, E. Ehrlacher, and J. Huennekens. "Radiative lifetimes, collisional mixing, and quenching of the cesium 5DJ levels". *Phys. Rev. A*, 45:1670–1683, Feb 1992.

[71] Shang-Yi, Ch'en. "Broadening, asymmetry and shift of rubidium resonance lines under different pressures of helium and argon up to 100 atmospheres". *Physical Review*, 58:1051–1058, 1940.

[72] Simsarian, JE, LA Orozco, GD Sprouse, and WZ Zhao. "Lifetime measurements of the 7 p levels of atomic francium". *Physical Review A*, 57(4):2448, 1998.

[73] Steck, Daniel A. "Rubidium 85 D line data", 2001.

[74] Steck, Daniel A. "Rubidium 87 D line data", 2001.

[75] Tang, KT and J Peter Toennies. "An improved simple model for the van der Waals potential based on universal damping functions for the dispersion coefficients". *The Journal of Chemical Physics*, 80(8):3726–3741, 1984.

[76] Tsi-Zé, Ny et al. "Pressure Effects of Rare Gases on the Second Doublet of Rubidium Principal Series". *Physical Review*, 52(11):1158, 1937.

[77] Volz, U and H Schmoranzer. "Precision lifetime measurements on alkali atoms and on helium by beam–gas–laser spectroscopy". *Physica Scripta*, 1996(T65):48, 1996.

[78] Wilson, John Norton and Richard M Curtis. "Dipole polarizabilities of ions in alkali halide crystals". *The Journal of Physical Chemistry*, 74(1):187–196, 1970.

[79] Wu, Sheldon SQ, Thomas F Soules, Ralph H Page, Scott C Mitchell, V Keith Kanz, and Raymond J Beach. "Hydrocarbon-free resonance transition 795-nm rubidium laser". *Lasers and Applications in Science and Engineering*, 68740E–68740E. International Society for Optics and Photonics, 2008.

[80] Wu, Sheldon SQ, Thomas F Soules, Ralph H Page, Scott C Mitchell, V Keith Kanz, and Raymond J Beach. "Resonance transition 795-nm rubidium laser using ^{3}He buffer gas". *Optics Communications*, 281(5):1222–1225, 2008.

[81] Wu, Sheldon SQ, Thomas F Soules, Ralph H Page, Scott C Mitchell, V Keith Kanz, and Raymond J Beach. "Resonance transition 795-nm rubidium laser using ^{3}He buffer gas". *Optics Communications*, 281(5):1222–1225, 2008.

[82] Ye, Jun, Steve Swartz, Peter Jungner, and John L Hall. "Hyperfine structure and absolute frequency of the ^{87}Rb $5P_{3/2}$ state". *Optics Letters*, 21(16):1280–1282, 1996.

[83] Zameroski, Nathan D, Gordon D Hager, Wolfgang Rudolph, Christopher J Erickson, and David A Hostutler. "Pressure broadening and collisional shift of the Rb D_2 absorption line by CH_4, C_2H_6, C_3H_8, n-C_4H_{10}, and He". *Journal of Quantitative Spectroscopy and Radiative Transfer*, 112(1):59–67, 2011.

[84] Zhdanov, Boris and RJ Knize. "Diode-pumped 10 W continuous wave cesium laser". *Optics Letters*, 32(15):2167–2169, 2007.

[85] Zhdanov, BV, T Ehrenreich, and RJ Knize. "Highly efficient optically pumped cesium vapor laser". *Optics Communications*, 260(2):696–698, 2006.

[86] Zhdanov, BV, J Sell, and RJ Knize. "Multiple laser diode array pumped Cs laser with 48 W output power". *Electronics Letters*, 44(9):582–584, 2008.

[87] Zhu, Qi, Bailiang Pan, Li Chen, Yajuan Wang, and Xunyi Zhang. "Analysis of temperature distributions in diode-pumped alkali vapor lasers". *Optics Communications*, 283(11):2406–2410, 2010.

[88] Zweiback, J, A Komashko, and WF Krupke. "Alkali-vapor lasers". 75810G–75810G, 2012.

REPORT DOCUMENTATION PAGE

Form Approved
OMB No. 0704–0188

1. REPORT DATE *(DD–MM–YYYY)*	2. REPORT TYPE	3. DATES COVERED *(From — To)*
17–09–2015	Dissertation	Sept 2012–Sept 2015

4. TITLE AND SUBTITLE

Temperature Dependent Rubidium-Helium Line Shapes
and Fine Structure Mixing Rates

5a. CONTRACT NUMBER

5b. GRANT NUMBER

5c. PROGRAM ELEMENT NUMBER

6. AUTHOR(S)

Miller, Wooddy S., Captain, USAF

5d. PROJECT NUMBER

5e. TASK NUMBER

5f. WORK UNIT NUMBER

7. PERFORMING ORGANIZATION NAME(S) AND ADDRESS(ES)

Air Force Institute of Technology
Graduate School of Engineering and Management (AFIT/EN)
2950 Hobson Way
Wright-Patterson AFB, OH 45433-7765

8. PERFORMING ORGANIZATION REPORT NUMBER

AFIT-ENP-DS-15-S-027

9. SPONSORING / MONITORING AGENCY NAME(S) AND ADDRESS(ES)

Missile Defense Agency (MDA)
Bldg. 5222, Martin Road
Redstone Arsenal, AL 35898-0001

10. SPONSOR/MONITOR'S ACRONYM(S)

11. SPONSOR/MONITOR'S REPORT NUMBER(S)

12. DISTRIBUTION / AVAILABILITY STATEMENT

DISTRIBUTION STATEMENT A:
APPROVED FOR PUBLIC RELEASE; DISTRIBUTION UNLIMITED

13. SUPPLEMENTARY NOTES

This work is declared a work of the U.S. Government and is not subject to copyright protection in the United States.

14. ABSTRACT

Line shapes for the Rb D_1 (5 $^2S_{1/2} \rightleftarrows$ 5 $^2P_{1/2}$) and D_2 (5 $^2S_{1/2} \rightleftarrows$ 5 $^2P_{3/2}$) transitions with ^{4}He and ^{3}He collisions at pressures of 500 - 15,000 Torr and temperatures of 333 - 533 K have been experimentally observed and compared to predictions from the Anderson-Talman theory. The observed collisionally induced shift rates for ^{4}He are dramatically higher for the D_1 line, 4.60 ± 0.12 MHz/Torr than the D_2 line, 0.20 ± 0.14 MHz/Torr. The asymmetry is somewhat larger for the D_1 line and has the same sign as the shifting rate. The ^{3}He broadening rate for the D_2 line is 4% larger than the ^{4}He rate, and 14% higher for the D_1 line, reflecting the higher relative speed. The calculated broadening rates are systematically larger than the observed rates by 1.1 - 3.2 MHz/Torr and agree within 14%. The primary focus of the first experiment is to characterize the high pressure line shapes, focusing on the non-Lorentzian features far from line center. In the far wing, the cross-section decreases by more than 4 orders of magnitude, with a broad secondary maximum in the D_2 line near 735 nm. The potentials do not require empirical modification to provide excellent quantitative agreement with the observations. The dipole moment variation and absorption Boltzmann factor is critical to obtaining strong agreement in the wings.

Temperature dependent shift and broadening rates have been experimentally measured over a temperature range of 373 K to 723 K and compared to prior predictions from the Anderson-Talman theory and quantum treatments involving Allard and Baranger coupling. The shift coefficients exhibit an increase of 20% from 4.36 MHz/Torr to 5.35 MHz/Torr for the D_1 line and an 80% increase from .42 MHz/Torr to .99 MHz/Torr for the D_2 line over the temperature range. Broadening coefficients exhibit a 6% increase from 17.8 MHz/Torr to 18.9 MHz/Torr and 10% from 18.5 MHz/Torr to 20.5 MHz/Torr for the D_1 and D_2 lines respectively. The experimental values agree well with prior reported values within the temperature overlap regions of T < 394 K. The closest theoretical prediction to the observed values is the Anderson-Talman approach using spin orbit multi reference (SOCI) ab initio potentials.

A laser induced fluorescence (LIF) experiment using a hybrid continuous wave (CW) - pulsed laser excitation pumping scheme was used to measure the temperature dependent spin-orbit (SO) mixing rates. An experimental apparatus was designed and built allowing for temperatures up to 723 K to be explored which is 350 K higher than any other experiment other than Gallagher in 1968. A proposal for a systematic exploration of the σ_{SO} rates was developed with initial observed values of 2.17×10^{-16} cm^2. The temperature dependence of the rates were explored resulting in a increase of 6 times the initial value compared with an increase of 3 time the initial value observed by Gallagher. These initial observations require further exploration.

15. SUBJECT TERMS

DPAL, Rubidium, Helium, Shift, Broadening, Rates, Temperature, Line Shape

16. SECURITY CLASSIFICATION OF:			17. LIMITATION OF ABSTRACT	18. NUMBER OF PAGES	19a. NAME OF RESPONSIBLE PERSON
a. REPORT	b. ABSTRACT	c. THIS PAGE			Dr. Glen P. Perram (ENP)
U	U	U	U	131	**19b. TELEPHONE NUMBER** *(include area code)* (937) 255-3636 x4504 Glen.Perram@afit.edu

Standard Form 298 (Rev. 8–98)
Prescribed by ANSI Std. Z39.18